UNIVERSITY OF GRANADA

Department of Applied Physics

Biocolloid and Fluid Physics Group

Thin Film Rheology and Ferrohydrodynamic Lubrication of Magnetic Fluids

Efrén Alberto Andablo Reyes

PhD Thesis

Thin Film Rheology and Ferrohydrodynamic Lubrication of Magnetic Fluids

by

Efrén Alberto Andablo Reyes

Licenciado en Física

SUPERVISORS

Dr. D. Juan de Vicente Álvarez-Manzaneda   Dr. D. Hugh A. Spikes
Prof. Titular de Física Aplicada   Prof. Tribology Group
                                                  Imperial College London

Dr. D. Roque Hidalgo Álvarez
Catedrático de Física Aplicada

A mis padres Efrén y Gloria,
Mis hermanas Miriam, Araceli y Gloria
y Amelia por no dejar de creer nunca en mí

A falta de astucia, trabajo duro …

Agradecimientos

Aprovecho este espacio para agradecer:

al Departamento de Física Aplicada por darme las facilidades para realizar esta tesis doctoral y a los proyectos Tribo-Reología de Fluidos Magnéticos (MAT-2006-13646-C03-03) y Tribo-Reología de Nuevos Fluidos MR (MAT-2009-14234-C03-03) por financiarla.

a mis directores Roque I. Hidalgo Álvarez, Juan de Vicente Álvarez Manzaneda y Hugh Spikes por haberme guiado durante estos últimos 3 años en mis actividades científicas y haber hecho todo lo necesario para facilitar la pronta presentación de este trabajo.

a todos mis compañeros en la Sala de Becarios por haberme apoyado en todos mis momentos de frustración, los cuales no fueron pocos, y sobre todo por haberme brindado su amistad.

a mi familia, pues sé que aunque hayan estado a una considerable distancia física de mí, han hecho todo lo posible para estar presentes de alguna forma en los momentos que más los necesitaba.

Contents

Chapter 1: Introduction

A magnetic nanofluid consists basically of magnetic nano particles dispersed in a liquid carrier forming a thermodynamically stable colloidal suspension [Rosensweig, 1997]. Their mechanical properties are similar to those of the carrier liquid but in the presence of a magnetic field, they behave like ferromagnetic materials and magnetic body forces are induced on them. The carrier liquid can be either a polar or non polar medium depending of the application in mind. For instance, water-based fluids have been studied as biocompatible suspensions for medical applications such as target drug delivery and magnetic resonance studies [Lavaca, 1999; Lavaca, 2010; Racuciu, 2007]. Oil-based magnetic nanofluids are most commonly used for mechanical applications. In a magnetic liquid seal, for example, a magnetic nanofluid is confined in a position due to the action of an appropriately-applied, non-uniform magnetic field distribution [Ravaud, 2010]. The magnetic nanofluid keeps two media separated by supporting the force exerted by the difference of pressure between them. At the same time, the fluid sustains moving parts of the mechanical system where the seal is being used. This is the case of the rotatory shaft used in the hard drive motors. This kind of seal has two main advantages, no maintenance is required and the leakage of sealing fluid during operation is almost negligible. For those reasons, they are widely used in many industrial and scientific applications, and they represent one of the most important mechanical applications of magnetic nanofluids.

We can also find in literature many theoretical studies of the possibility of using magnetic nanofluids to improve the performance of lubricated contacts. Thrust, journal and pad bearings are examples of contacts widely used in mechanical systems. For instance, in a thrust bearing, theoretical calculations have shown that the use of magnetic nanofluids as lubricants is plausible for small contacts with size limited to a few centimeters and loads restricted to lower than 100 N [Walker, 1979]. These conditions are satisfied for instance in micro electro mechanical systems (MEMS) [Ku, 2009], but obviously, a magnetically lubricated pad bearing is not suitable for use in a boat-propelling system. In journal bearings, the confinement ability of magnetic nanofluids is convenient to avoid lubricant leakage out of the contact clearance [Shah, 2004; Naduvinamani, 2009; Kuzhir, 2007].

Irrespective of the contact geometry, a key role of lubrication is to reduce the friction forces acting on rubbing surfaces during operation. Bearing this in mind, the control of friction in contacts lubricated with magnetic nanofluids and operating in the hydrodynamic lubrication regime was taken as the main objective of the present work. In the hydrodynamic lubrication regime, the surfaces of the contact are fully separated by a thin, pressurized lubricant film. Hydrodynamic lubrication usually occurs between sliding/rotating non-conforming surfaces in the presence of a fluid or lubricant. An alternative to this mechanism is so-called squeeze flow, where occurs when the surface approach forces the fluid to flow outward from the contact. The performance of a contact lubricated by a perfect Newtonian fluid operating in this regime is well described by the Reynolds lubrication theory. Describing a contact lubricated by a magnetic nanofluid requires the introduction of the extra magnetic body forces that appear on it when placed in the presence of a magnetic field.

This work is structured as follows: Chapter 2 is used to present a brief revision of theoretical details related to the mechanics of Newtonian fluids, including the Reynolds theory for hydrodynamic lubrication. Chapter 3 describes the properties of magnetic nanofluids and introduces a modified Reynolds lubrication theory to describe their performance as lubricants in the presence of a magnetic field distribution. In Chapter 4 the first results of this study are presented. Here, a contact lubricated with a Newtonian fluid consisting of two tilted rigid flat surfaces, which operates in the hydrodynamic lubrication regime, is studied by means of the Reynolds lubrication theory. A contact with a similar geometry, but lubricated with a magnetic nanofluid, is experimentally and theoretically studied in Chapter 5. The possibility of control the friction in the contact using an externally applied magnetic is explored. In Chapter 6 the appearance of starvation is studied in a contact lubricated with a magnetic nanofluid working in the soft elasto-hydrodynamic lubrication regime. In the absence of a magnetic field, starvation occurs in this contact at high speeds of operation due to the limited amount of lubricant available. A magnetic field distribution is used to confine the fluid around the contact in order to prevent the onset of starvation. Finally, in Chapter 7, a summary of all the results is presented together the most important conclusions from this work.

Chapter 2: Basic concepts on lubrication

In this chapter, a brief revision of fluid mechanics is presented. The concept of Newtonian fluid is introduced, as well as the equations governing its motion. Finally, the Reynolds lubrication theory for contacts working in the hydrodynamic lubrication regime is explained.

2.1 Lubricated contacts.

A lubricated contact consists of two or more rubbing surfaces in the presence of a fluid. The fluid can be a liquid or a gas. The fluid forms a lubricating film between the surfaces. The surfaces support a load that tends to bring them into contact and this load is counteracted by pressurization that occurs within the lubricating film. The presence of the lubricating film between the surfaces decreases the friction force. The varying nature of the lubrication forces acting on a contact results in a classification into three lubrication regimes: boundary, mixed and hydrodynamic lubrication. In the boundary regime, the lubrication is provided by very thin protective layers formed on contacting surface asperities by physical or chemical adsorption, whose thickness and strength are determined by the nature of interaction between the surfaces and the lubricant, such as hydrophobic-hydrophilic forces [Bongaerts, 2007; Persson, 2009]. In this regime, friction is determined by the force needed to shear the coatings on the asperities in direct contact. In the hydrodynamic lubrication regime, the surfaces are separated by a relatively thick film of fluid and the friction is determined by the shear stress of the fluid film. This regime is well described by the hydrodynamic lubrication theory of Reynolds that will be explained in detail in the next sections. The mixed lubrication regime shares characteristics of both boundary and hydrodynamic lubrication since there is partial asperity contact.

All of these lubrication regimes are commonly described in the form of a "Stribeck curve" (Figure 2.1) [Lubbinge; 1999, Kavehpour, 2004] in which the friction coefficient μ is plotted as a function of the Gumbel number Gu (or duty parameter). The friction coefficient is the ratio between the tangential (rolling and/or sliding) force F_S and the normal load F_N (commonly known as load capacity) applied to the contact surfaces as mathematically expressed in equation (2.1);

$$\mu = \frac{F_S}{F_N} \qquad\qquad (2.1)$$

The most general definition of the Gumbel number groups the relative speed V between rubbing surfaces, the high shear rate lubricant viscosity η, the contact area A and the

normal load F_N. The proportionality between this group of variables and the Gumbel number Gu is given in equation (2.2).

$$Gu \propto \frac{\eta V A}{F_N} \tag{2.2}$$
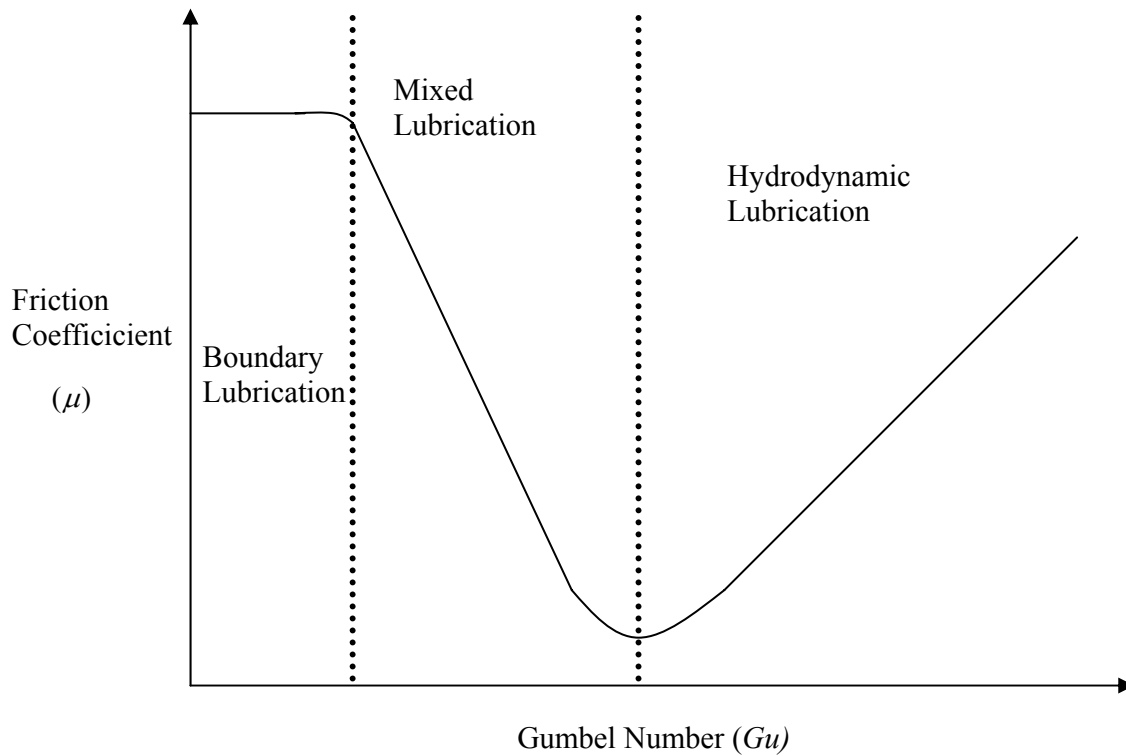
Figure 2.1. The performance of a lubricated contact is usually represented in a Stribeck curve as shown here. The curve is divided in three regions corresponding to the different lubrication regimes: boundary, mixed and hydrodynamic lubrication.

2.2 Equations of motion of Newtonian fluids

2.2.1 Newtonian fluids.

Consider the simple shearing experiment depicted in Figure 2.2. Two parallel planes are separated by a thin fluid film of thickness h. The upper plane is displaced with velocity V while the lower remains in a fixed position. In this experiment, the force exerted on the displaced surface is equilibrated by a force on the other surface with the same

magnitude but opposite direction. Thus, the surfaces submit the fluid to a superficial force per unit area τ called the shear stress. A fluid is called Newtonian when it satisfies the relation [Bird, 1982; Fay, 1996]

$$\tau = \eta \frac{V}{h} \qquad (2.3)$$

where η is independent of the shear rate. The quantity V/h is the velocity gradient generated through the fluid film and it is commonly known as shear rate. The proportionality constant in equation (2.3) is the fluid viscosity η, which determines the resistance of a fluid to flow when this is submitted to external shearing forces.
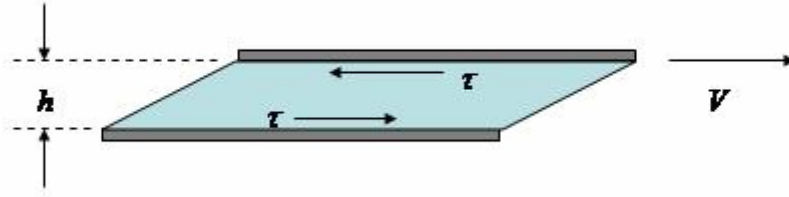
Figure 2.2. Shearing experiment on a fluid between to parallel surfaces. The space of height h between two parallel surfaces is filled with a fluid. The upper surface is displaced with velocity V and the lower is kept fixed. Both surfaces experience a force per unit area, τ of the same magnitude but opposite direction.

In general, for a Newtonian fluid, the stress and the velocity profile satisfies the relation

$$\underline{\underline{\tau}} = \eta\left(\nabla \underline{V} + \nabla^T \underline{V}\right) + \frac{3}{2}\eta(\nabla \bullet \underline{V})\underline{\underline{I}} \qquad (2.4)$$

Here, $\underline{\underline{\tau}}$ is the second order extra-stress tensor, $\underline{\underline{I}}$ is the second order identity tensor, $\underline{V}$ is the velocity vector, $\nabla \bullet \underline{V}$ is its divergence, $\nabla \underline{V}$ and $\nabla^T \underline{V}$ are the velocity gradient and the velocity gradient transposed, respectively. The first term in equation (2.4) is the generalization of equation (2.3), while the second term is related to the changes in the

fluid density due to the imposition of a normal stress. In most cases, the fluids are supposed to be incompressible and the last term is zero.

The flow of Newtonian fluids is mathematically described by the continuity and the Navier-Stokes equations. Unlike turbulent flows, in which non-stationary chaotic velocity fields may occur even when the conditions controlling the flows are time-independent, laminar flow can be described by physical intuition. On the one hand, the continuity equation expresses the conservation of mass rate in the flow. On the other hand, the Navier-Stokes equation expresses the second law of Newton for viscous Newtonian fluids. Solving an isothermal flow problem implies to solve both equations simultaneously. These equations will be introduced in the following subsections.

2.2.2 Continuity equation.

The continuity equation expresses mathematically the conservation of the fluid mass in a flow experiment. This equation is deduced by applying a balance of matter in a stationary element of volume crossed by the fluid flow. The mass rate of fluid entering the volume must be the sum of the rate of fluid leaving it and the rate of accumulation of fluid inside the volume. Consider the simple situation in Figure 2.3. A fluid of density ρ enters in a volume $\Delta x \Delta y \Delta z$ through the face x with mass rate $\rho V_x(x) \Delta y \Delta z$ and leaves the volume with mass rate $\rho V_x(x + \Delta x) \Delta y \Delta z$ through the face situated at $x + \Delta x$. The rate of mass being accumulated inside the fluid is $\Delta x \Delta y \Delta z \dfrac{\partial \rho}{\partial t}$. For this simple case, the balance of matter is

$$\rho V_x(x) \Delta y \Delta z - \rho V_x(x + \Delta x) \Delta y \Delta z = \Delta x \Delta y \Delta z \frac{\partial \rho}{\partial t} \qquad (2.5)$$

For a flow that crosses all the faces, the rest of the mass rate component entering and leaving the volume must be included in equation (2.5). The resulting balance of matter is

$$\begin{aligned} &\left[\rho(x)V_x(x) - \rho(x + \Delta x)V_x(x + \Delta x)\right]\Delta y \Delta z + \left[\rho(y)V_y(y) - \rho(y + \Delta y)V_y(y + \Delta y)\right]\Delta x \Delta z \\ &+ \left[\rho(z)V_z(z) - \rho(z + \Delta z)V_z(z + \Delta z)\right]\Delta x \Delta y = \Delta x \Delta y \Delta z \frac{\partial \rho}{\partial t} \end{aligned} \qquad (2.6)$$

Dividing equation (2.6) by the volume size and taking the limit when this goes to zero, we obtain the continuity equation [Bird, 1982; Fay, 1996]

$$\frac{\partial \rho}{\partial t} = -\nabla \bullet \left(\rho \underline{V} \right) \tag{2.7}$$

The material derivative of a quantity can be written as

$$\frac{d}{dt} = \frac{\partial}{\partial t} + \underline{V} \bullet \nabla \tag{2.8}$$

Using equation (2.8), equation (2.7) can be rewritten as

$$\frac{d\rho}{dt} = -\rho \nabla \bullet \underline{V} \tag{2.9}$$

If the fluid density is constant and uniform then the fluid is considered incompressible and the material derivative of the fluid density in equation (2.9) is zero. Then the continuity equation for an incompressible fluid is;

$$\nabla \bullet \underline{V} = 0 \tag{2.10}$$
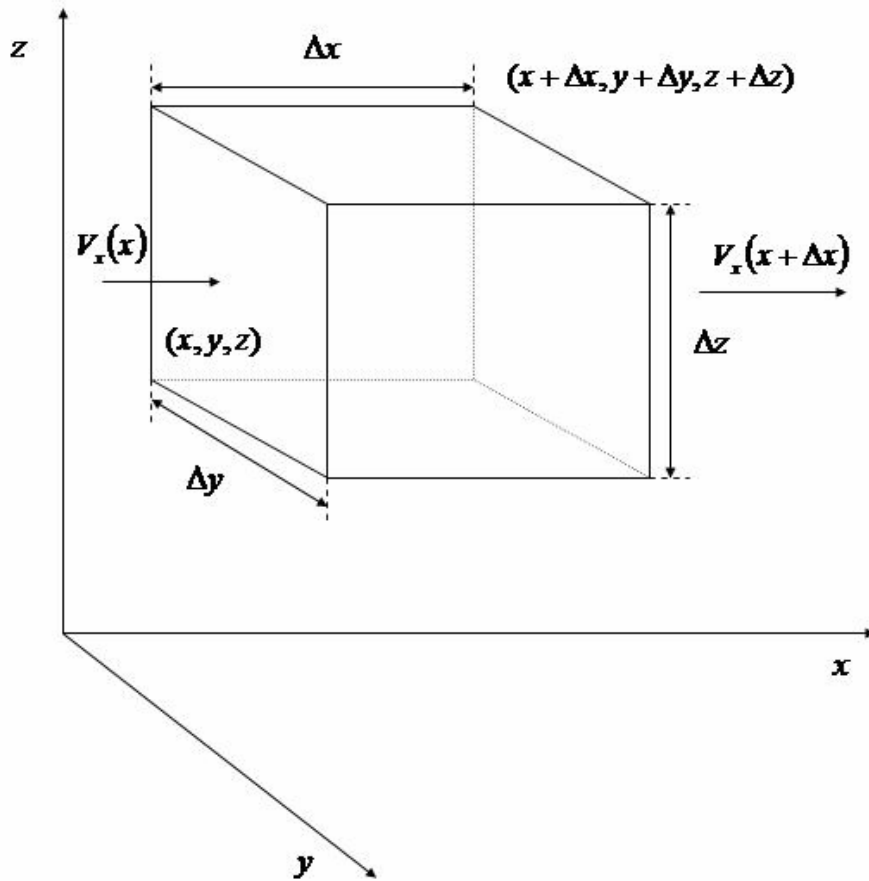
Figure 2.3. A volume of size $\Delta x \Delta y \Delta z$ is crossed by a fluid along the x direction.

2.2.3 Navier-Stokes equation.

In this section, the equation of motion that describes the flow of a Newtonian fluid will be introduced in its more general form. To describe the motion of a fluid it is necessary to find a Newton-like equation for an infinitesimal volume, *i.e.*, an equation of the form

$$\rho \frac{dV}{dt} = \underline{f}_t \tag{2.11}$$

where $\underline{f}_t$ is the total density force acting on an infinitesimal fluid volume. For a viscous Newtonian fluid $\underline{f}_t$ is the sum of gravity, pressure and viscous forces. The gravity density force $\underline{f}_g$ acting on every point at the fluid is

$$\underline{f}_g = \rho \underline{g} \tag{2.12}$$

where $\underline{g}$ is the gravitational acceleration.

On any infinitesimal fluid volume acts a force due to the difference of pressure **p** at the faces of the small volume. The pressure-density force $\underline{f}_p$ acting at any point at the fluid is mathematically expressed by equation (2.13).

$$\underline{f}_p = -\nabla p \tag{2.13}$$

Finally, the viscous-density force is;

$$\underline{f}_v = \nabla \bullet \underline{\underline{\tau}} \tag{2.14}$$

In agreement with the continuity equation, for an incompressible Newtonian fluid, the stress expressed in equation (2.4) is

$$\underline{\underline{\tau}} = \eta \left(\nabla \underline{V} + \nabla^T \underline{V} \right) \tag{2.15}$$

Introducing equation (2.15) in (2.14) it is found that the viscous-density force for an incompressible Newtonian fluid is

$$\underline{f}_v = \eta \nabla^2 \underline{V} \tag{2.16}$$

Thus, the total density force acting on an infinitesimal fluid volume is

$$\underline{f}_t = -\nabla p + \eta \nabla^2 \underline{V} + \rho \underline{g} \tag{2.17}$$

Now it is possible to write an equation to describe the motion of an incompressible Newtonian fluid. That is

$$\rho \left[\frac{\partial \underline{V}}{\partial t} + \underline{V} \bullet \nabla \underline{V} \right] = -\nabla p + \eta \nabla^2 \underline{V} + \rho \underline{g} \qquad (2.18)$$

Equation (2.18) is known as the Navier-Stokes equation [Bird, 1982; Fay, 1996].

2.3 Hydrodynamic lubrication theory

2.3.1 The lubrication approximation: Reynolds equation

Figure 2.4 presents a scheme of hydrodynamic lubrication between two sliding, non-parallel surfaces in the presence of a fluid. The bottom surface moves with speed V_0 while the upper surfaces remains fixed. The plane where the displacement of the surface lies will be called the shearing plane in further discussion. As the bottom surface moves it drags the lubricant along it into the converging wedge. A pressure field is generated as otherwise there would be more lubricant entering the wedge than leaving it. Thus at the beginning of the wedge the increasing pressure restricts the entry flow and at the exit there is a decrease in pressure boosting the exit flow. The pressure gradient therefore causes the fluid velocity profile to bend inwards at the entrance to the wedge and bend outwards at the exit, as shown in Figure 2.4 [Stachowiak, 2000]. The generated pressure separates the two surfaces and is also able to support a certain load. It is important to note that if there is no converging wedge, no pressure gradient will arise.

Pressure profile

$p(r_\parallel)$

p_{max}

Fixed surface

Inlet flow

Outlet flow

$h(r_\parallel)$

z

y

Sliding surface

V_0

V_{0x} V_0

x

V_{0y}

L
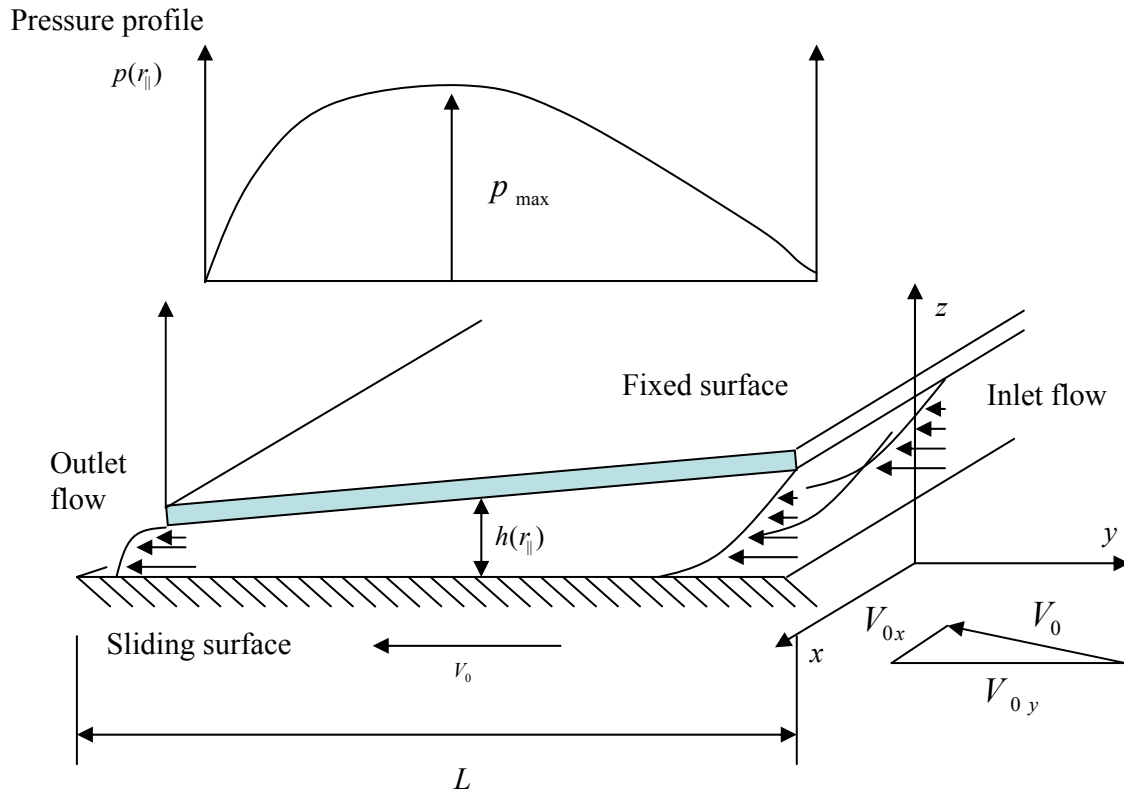
Figure 2.4. Schematic representation of a shearing flow between two tilted surfaces. In the hydrodynamic lubrication regime a pressurized fluid film separates completely the surfaces.

Usually in a lubricated contact the distance between the surfaces h is small compared to the dimensions L of their surfaces, even in the hydrodynamic lubrication regime. Under this assumption, it is plausible to suppose that the changes in the pressure through the thin lubricant film in the perpendicular direction to the shearing plane are negligible together the gravitational effects. In addition, inertial effects in the gap can be considered small in comparison with viscous forces. Then the Navier-Stokes equation that describes the problem of a narrow contact gap becomes [Stachowiak, 2000]

$$0 = -\nabla p + \eta \nabla^2 \underline{V} \tag{2.19}$$

Equation (2.19) can be divided in its components parallel and perpendicular with respect to the shearing plane. In the following, these components will be denoted using the subscripts $\parallel$ and $\perp$ respectively. As example, consider the case of the shearing plane corresponding to the plane **x-y**, in such a way that the coordinate $\underline{V}_\parallel$ of the velocity

profile lies on the cited plane, and $\underline{V}_\perp$ lies on the axis z. Then, nabla operators can be defined to contain the derivatives of the variables of the x-y plane ($\nabla_\parallel$) and z axis ($\nabla_\perp$). Equation (2.19) can be further simplified if we realize that, in a thin film, the gradients of velocity in the direction parallel of plane of stress (∥) are small compared to the gradient in the perpendicular direction (⊥). Then we can suppose that

$$\nabla_\parallel{}^2 \underline{V} \approx 0 \tag{2.20}$$

Bearing all this in mind, the Navier-Stokes equation can be rewritten as

$$\nabla_\parallel p = \eta \nabla_\perp{}^2 \underline{V}_\parallel \tag{2.21}$$

and

$$\nabla_\perp p = 0 \tag{2.22}$$

All the assumptions to go from equation (2.18) to equations (2.21) and (2.22) constitute the so-called lubrication approximation. Equation (2.22) expresses mathematically what was previously mentioned: the pressure does not depend on the coordinate perpendicular to the shearing plane. Equation (2.21) can be integrated to obtained expressions for the speed components on the shearing plane assuming no-slip boundary conditions. If the fluid is supposed to be incompressible, the condition of mass rate conservation in the flow can be mathematically expressed by equation (2.10). After substitution of the expressions for fluid speed in equation (2.10), the last must be integrated to obtain the Reynolds equation for lubrication.

For the case described previously, where the shearing plane lies parallel to the plane x-y, with $z = 0$, the expressions for the speeds are

$$V_x = \frac{\left(h(x,y)z - z^2\right)}{2\eta} \partial_x p(x,y) + \frac{V_{0x}\left(h(x,y) - z\right)}{h(x,y)} \tag{2.23}$$

and

$$V_y = \frac{\left(h(x,y)z - z^2\right)}{2\eta}\partial_y p(x,y) + \frac{V_{0y}\left(h(x,y) - z\right)}{h(x,y)} \tag{2.24}$$

Here, $p(x,y)$ and $h(x,y)$ are the pressure and the thickness of the lubricant film. V_{0x} and V_{0y} are the components of the speed of the surface in the x and y directions, respectively.

Using equation (2.23) and (2.24) in the continuity equation (2.10), the Reynolds equation (2.25) is obtained.

$$\partial_x\left[h^3(x,y)\partial_x p(x,y)\right] + \partial_y\left[h^3(x,y)\partial_y p(x,y)\right] = 12\eta\left[V_{0x}\partial_x h(x,y) + V_{0y}\partial_y h(x,y)\right] \tag{2.25}$$

Reynolds equation can be equivalently written in other coordinates systems to straightforwardly describe any contact shape. For instance, in polar coordinates Reynolds equation can be written as (Sabir, 2007; Koc, 2007)

$$\partial_r\left[rh^3\partial_r p(r,\theta)\right] + \frac{1}{r}\partial_\theta\left[h^3\partial_\theta p(r,\theta)\right] = 6\eta\Omega r\partial_\theta h(r,\theta) \tag{2.26}$$

and the angular velocity is

$$V_\theta(r,\theta) = \frac{\left(z^2 - h(r,\theta)z\right)}{2\eta}\partial_\theta p + r\Omega\frac{z}{h} \tag{2.27}$$

Equation (2.26) describes the contact represented in Figure 2.5, the upper surface rotates with angular speed Ω and the bottom surface is fixed. The shearing plane is parallel to the x-y plane.
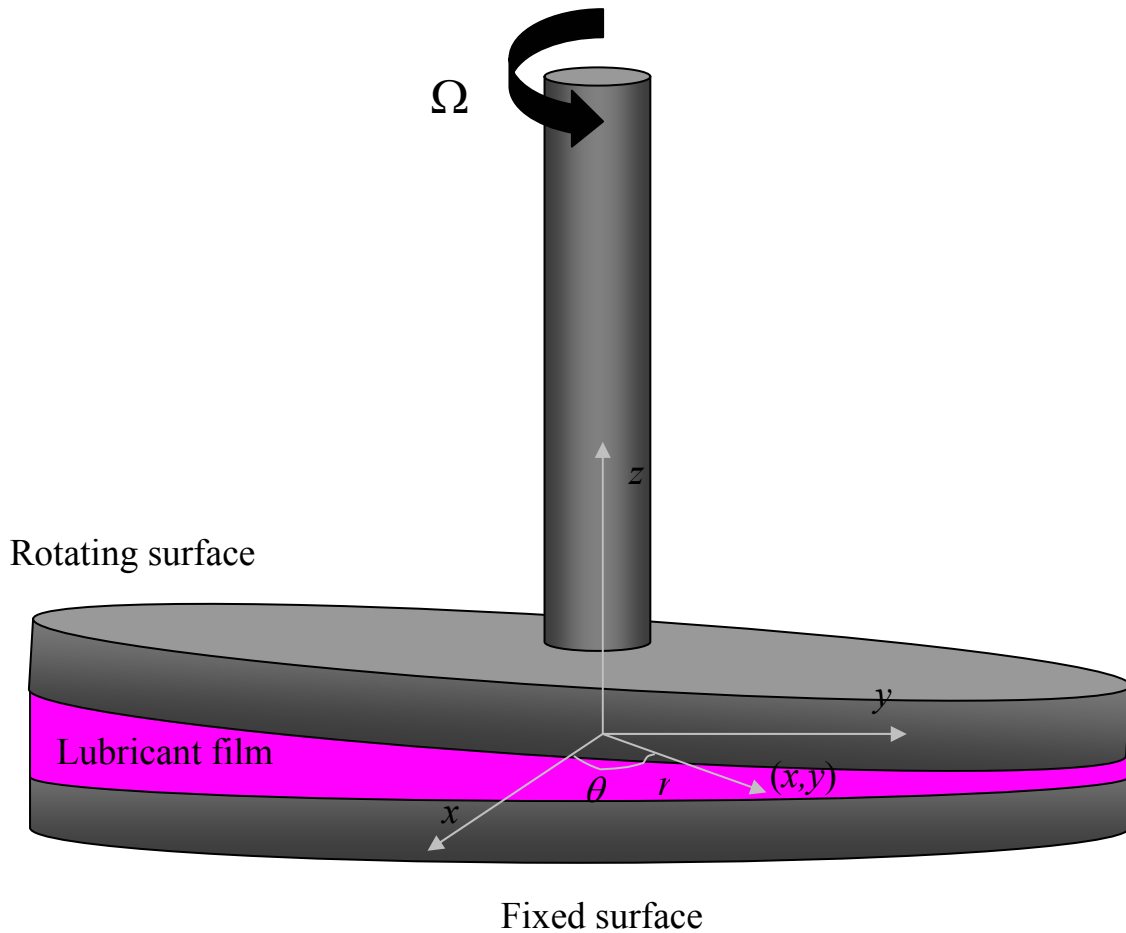
Figure 2.5. Schematic representation of a contact where the upper surface rotates with angular speed Ω, and the bottom surface is fixed. A straightforward description of this contact can be carried out by a Reynolds equation written in polar coordinates, where the position of any point in the x-y plane is described by the polar coordinates (r,θ).

It is important to remark that if the film thickness is uniform along the contact surfaces, no pressure film will be generated, in agreement to the right hand term in the Reynolds equation.

2.3.2 The lubrication parameters.

Once pressure and film thickness of lubricant in the contact have been found by solving Reynolds equation, it is possible to find the parameters needed to describe the performance of the lubricated contact. The normal force applied to the surfaces, which is supported completely by the fluid film in the hydrodynamic lubrication regime, is called the load capacity F_N. It is found integrating the pressure over the surface of the contact S covered by the fluid.

$$F_N = \int_S p(\underline{r}')dS'$$
(2.28)

The shearing force F_S acting on the fluid is calculated by integrating the shear stress τ (equation (2.15)) on the fluid over the contact surface.

$$F_S = \int_S \tau(\underline{r}')dS'$$
(2.29)

The tangential force is the sum of the contributions of the Couette and the Poisseuille flow in the contact. The first is directly related to the film shape, relative velocity of surfaces and fluid viscosity. The second is due to the pressure film distribution generated in the fluid film.

Once the normal and tangential forces have been found, the region of the Stribeck curve corresponding to the hydrodynamic lubrication regime can be determined by calculating the friction coefficient and Gumbel number as given in equation (2.1) and (2.2), respectively.

2.3.3 Soft elasto-hydrodynamic lubrication in point contacts.

Soft elasto-hydrodynamic lubrication occurs when the contact pressure is high enough to deform at least one of the contacting surfaces, but is not high enough to cause a significant change on the lubricant viscosity at the contact inlet. Soft elasto-hydrodynamic lubrication occurs not only in engineering applications like elastic bearing and seals, but also in biological systems [de Vicente, 2005, de Vicente, 2006]. In cartilaginous joints the elastic properties of the surfaces may play an important role in the performance of the hydrodynamic lubrication forces in the contact [Skotheim, 2004].

The elastic deformation ω at the point $\underline{r}$ of a contact composed of two surfaces of area S due to a pressure distribution p is [Ranger, 1975]

$$\omega(\underline{r}) = \frac{2}{\pi E'} \int_S \frac{p}{|\underline{r} - \underline{r}'|} dS'$$
(2.30)

Here, $2/E' = \left[\left(1 - v_1^2\right)/E_1 + \left(1 - v_2^2\right)/E_2 \right]$, where v_1, v_2, E_1 and E_2 are the Poisson's ratios and Young modulus of the two contacting bodies, respectively. Thus, the deformed film thickness h is

$$h(\underline{r}) = h_0(\underline{r}) + \omega(\underline{r}) + k \tag{2.31}$$

where h_0 is the non-deformed shape of the contact and k is a constant to be determined by the conditions imposed to the problem.

By solving Reynolds equation in combination of equation (2.30) and (2.31), the film thickness and the pressure in a soft contact can be found, and therefore the load capacity and friction acting between the surfaces can be calculated.
In particular for this work, the soft contact of interest is a soft point contact similar to that illustrated in Figure 2.6. For a sliding-rolling ball-plate contact operating in the soft elasto-hydrodynamic lubrication regime under fully-flooded conditions, Reynolds equation predicts values of the minimum h_m and central h_c film thickness given by equations (2.32) and (2.33), respectively [de Vicente, 2005, de Vicente, 2006].

$$h_m = \frac{2.8 R'^{0.78} (U\eta)^{0.66}}{E'^{0.44} W^{0.22}} \tag{2.33}$$

and

$$h_c = \frac{3.3 R'^{0.68} (U\eta)^{0.6}}{E'^{0.86} W^{0.11}} \tag{2.34}$$

Here, W represents the load applied to the contact and $U = (u_B + u_D)/2$ the entrainment speed, where u_B and u_D are the surface speed of the ball and disc, respectively. R' is the reduced radius in the entrainment direction, given by $1/R' = 1/R_{x1} + 1/R_{x2}$, where R_{x1}, R_{x2} represent the radii of the two contacting bodies respectively. These predictions are not far from other theoretical models available in literature [Hamrock, 1978].

The friction at the contact is

$$\mu = 1.46\frac{(\eta U)^{0.65}W^{-0.70}}{E'^{1.35}R'^{2.05}} + SRR(3.8\frac{(\eta U)^{0.71}W^{-0.76}}{E'^{1.47}R'^{2.23}} + 0.96\frac{(\eta U)^{0.36}W^{-0.11}}{E'^{0.47}R'^{0.58}}) \quad (2.35)$$

Here *SRR* denotes the slide-to-roll ratio defined as the ratio of the absolute value of sliding speed, $|u_B$-$u_D|$ to the entrainment speed *U*. The first term in equation (2.35) is the Poiseuille contribution to the friction while the second corresponds to the Couette friction. In the hydrodynamic lubrication regime, both contributions increase with the parameter ηU, and decreases with the load applied between the ball and the plane.
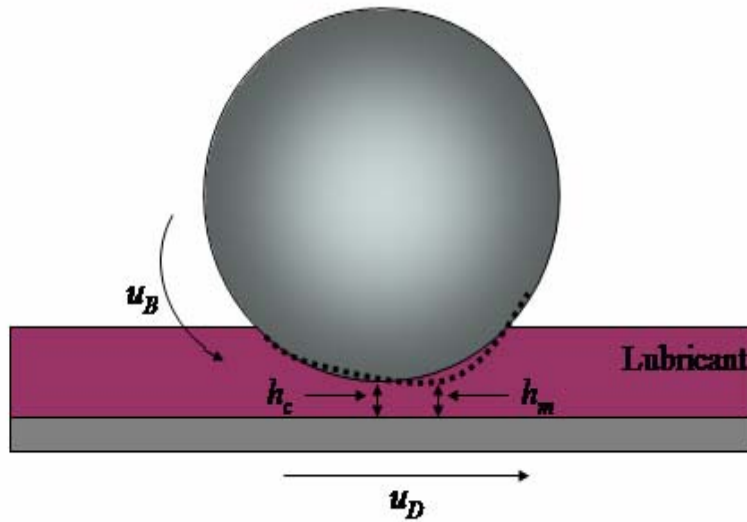
Figure 2.6. Soft point contact between a ball and a plane. The ball and the plane move with linear speed u_B and u_D, respectively. The dotted line represents the deformation of the contact. The contact area increases due to the deformation.

Chapter 3: Ferro-hydrodynamic lubrication theory

The properties of magnetic nanofluids, commonly denominated as ferrofluids, are discussed in this chapter. Most of this discussion is a summary of the content on this subject from the book of "Ferrohydrodynamics" by Rosensweig. In addition, the Reynolds theory for hydrodynamic lubrication has been modified to include the magnetic body forces acting on the magnetic nanofluid in the presence of a magnetic field.

3.1 Magnetic nanofluids.

3.1.1 What are magnetic nanofluids?

Magnetic nanofluids (more commonly called ferrofluids) are colloidal dipolar suspensions of superparamagnetic monodomain ferro- or ferrimagnetic nanometric particles coated with an absorbed layer of a long chain molecular species and dispersed in a liquid carrier [Rosensweig, 1997]. The latter is commonly a Newtonian fluid. A very well stabilized suspension of this kind retains the Newtonian behaviour of the continuum phase but ha properties of a ferromagnetic material when it is placed in a magnetic field. The basic properties of a magnetic nanofluid, such as magnetization and magnetic body forces, will be studied in the next subsections. Here the requirements that a magnetic nanofluid must satisfy to behave as a well stabilized suspension will be discussed.

The particle size must lie in the colloidal range to allow Brownian motion to keep particles suspended without settling out. In addition, the interparticle dipolar magnetic interaction will induce the formation of particle clusters if Brownian forces are not strong compared to the magnetic forces. The balance between these forces can be quantified by means of their respective energies. On the one hand, the thermal energy E_T of a particle suspended in a fluid at absolute temperature T is

$$E_T = k_B T \tag{3.1}$$

where k_B is the Boltzmann constant. On the other hand, two particles of diameter d with permanent dipolar moment

$$m = \frac{\pi}{6} d^3 M \tag{3.2}$$

where M is their permanent magnetization, interact with a magnetic energy

$$E_d = \frac{\pi}{72} \mu_0 M^2 d^3 \tag{3.3}$$

In order to avoid particle agglomeration $E_T > E_d$, *i.e.*,

$$k_B T > \frac{\pi}{72} \mu_0 M^2 d^3$$

(3.4)

Equation (3.4) restricts the particle size to

$$d \leq \left(\frac{72 k_B T}{\pi \mu_0 M^2} \right)^{\frac{1}{3}}$$

(3.5)

As example, for a suspension of magnetite particles with $M = 447$ kA/m the particle diameter must be smaller than 10 nm at room temperature in agreement to equation (3.5). In an actual magnetic fluid, the particles are not completely single-sized. The larger particles may aggregate forming clusters and result in the suspension displaying non-Newtonian behavior [Mahle, 2008]. To ensure stabilization of magnetic colloids with particle size around the limit previously mentioned, it is also important to reduce the particle size polydipersity.

Van der Waals attractive forces can not be forgotten in this discussion, as they may also promote the formation of colloidal aggregates in the suspension. distances. These forces appear spontaneously between neutral and charged particles due to the dipole-dipole interaction. The energy of interaction E_w of the fluctuating dipoles can be estimated using equation (3.6) [Rosensweig, 1997].

$$E_w = -\frac{A}{6} \left\{ \frac{2}{l^2 + 4l} + \frac{2}{(l+2)^2} + \ln \left[\frac{l^2 + 4l}{(l+2)^2} \right] \right\}$$

(3.6)

In equation (3.6), A is the so called Hamaker constant and depends on the dielectric properties of the particle and the continuum medium, $l = \frac{2s}{d}$ where s is the distance between the surfaces of the interacting particles and d is their diameter. The force related to the energy in equation (3.6) is of short range, it varies with l^6 for distant particles and l^1 when the particles are close to contact. If the surfaces of two particles come into contact, in theory an infinite energy would be needed to separate them. Thus,

the direct contact between particles surfaces must be avoided. This is achieved by adding a steric repulsive mechanism to the set of forces acting on the particles. The steric repulsion is provided by a protective coating of amphiphilic molecules adsorbed on the particle surfaces.

For two spheres of diameter d coated with uniform molecular layers of thickness δ with the surfaces separated by a distance s, the steric energy of repulsion is [Rosensweig, 1997]

$$\frac{E_r}{k_B T} = \frac{\pi d^2 \xi}{2}\left[2 - \frac{l+2}{t}\ln\left(\frac{1+t}{1+\dfrac{l}{2}}\right) - \frac{l}{t}\right] \tag{3.7}$$

where ξ is the surface concentration of molecules adsorbed at the particle surface and $t = \dfrac{2\delta}{d}$. The steric repulsive force is proportional to the number of molecule adsorbed on the particle surfaces and increases also with the coating thickness. These two values must be carefully chosen to achieve the stabilization of the suspension. This mechanism can be affected if a well stabilized suspension is diluted, due to the surface molecular density being decreased [Dababneh, 1995; Chantrell, 1982].

Very well stabilized magnetic nanofluids offer interesting properties that can be used in mechanical [Miranda, 2004; Walker, 1979; Kumar, 1993] and medical applications. For instance, the synthesis of magnetic nanofluids has found a challenge in obtaining stable biocompatible suspensions for medical applications such as magnetic resonance studies [Lavaca, 1999; Lavaca, 2010; Racuciu, 2007].

3.1.2 Magnetization models for magnetic nanofluids.

In a magnetic nanofluid, the magnetization $M(H)$ is a nonlinear function of the applied magnetic field H. The simplest model to describe $M(H)$ is the Langevin model. This model considers a suspension of non-interacting, superparamagnetic and monodisperse particle of diameter d and saturation magnetization M_d. For a fluid that satisfies the these conditions the fluid magnetization is given by the expression [Rosensweig, 1997]

$$M(H) = \phi M_d L(\alpha) \tag{3.8}$$

where

$$L(\alpha) = \coth(\alpha) - \frac{1}{\alpha} \tag{3.9}$$

$$\alpha = \frac{\mu_0 m H}{k_B T} \tag{3.10}$$

Figure 3.1 shows the Langevin magnetization model as function of the applied magnetic field for different particle diameters. In agreement with the Langevin model, the fluid magnetization $M(H)$ has an asymptotic linear behavior with the strength of the magnetic field H for low values of the latter. Here, the slope of the magnetization curve is the initial magnetic susceptibility, defined as

$$\chi_i = \frac{M(H)}{H} = \frac{\pi}{18} \phi \mu_0 \frac{M_d^2 d^3}{k_B T} \tag{3.11}$$

The initial susceptibility is proportional to the cubed power of particle diameter d. This can be observed in the faster growth of the fluid magnetization at low values of the magnetic field for larger particle size. At very intense magnetic fields, the fluid magnetization reaches a maximum value of saturation M_s. This value is proportional to the volume fraction of the particles and their magnetic saturation as expressed by equation (3.12).

$$M_s = \phi M_d \tag{3.12}$$

Experimental evidence shows that, in a fine magnetic nanofluid, the particle size distribution satisfies a lognormal distribution function of the form [Berret, 2006; Huang, 2004]

$$f_p(x) = \frac{1}{x\sigma\sqrt{2\pi}}\exp\left[-\frac{\ln(x)^2}{2\sigma^2}\right] \tag{3.13}$$

where the particle size polydispersity is described by the standard deviation σ. The magnetization of the fluid is then the sum of the contribution of particles of different sizes x. Thus, the Langevin function must be weighted using the particle size distribution as shown in equation (3.14).

$$M(H) = \phi M_s \int_0^\infty L(x,H) f_p(x) dx \tag{3.14}$$

Magnetization curves obtained using equation (3.14) are shown in Figure 3.2 for a particle size of 10 nm and σ = 0.1, 0.3 and 0.5. The smaller particles have a major influence than larger ones at intermediate and high magnetic field, lowering the magnetic susceptibility of the fluid. In contrast to this, the initial susceptibility is more influenced by the larger particles (see Figure 3.1) and increases with σ as shown in Figure 3.3. Fitting equation (3.14) to experimental measurements of the magnetization curve of a magnetic nanofluid allows determination of the mean particle size and the polydispersity of its solid content [Chantrell, 1978; Ivanov, 2007].
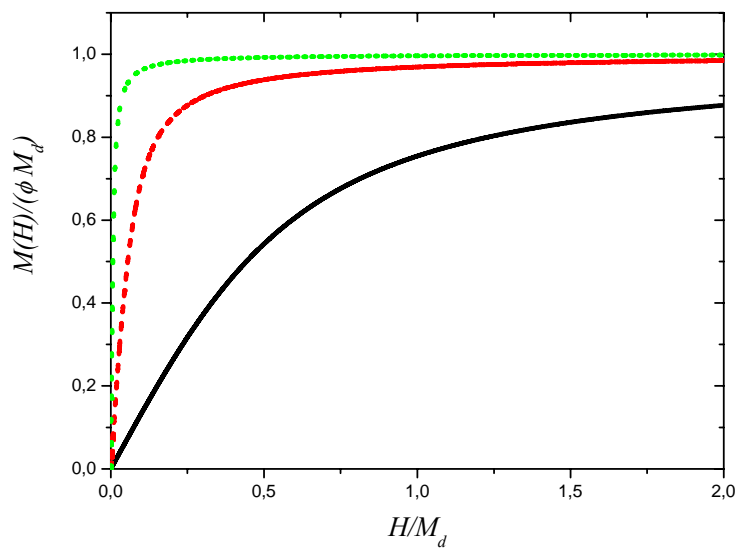
Figure 3.1. Langevin model of fluid magnetization for magnetite particles M_d = 447 kA/m, with diameter of (solid) 5, (dashed) 10 and (dotted) 20 nm. T = 298.15 ºK.
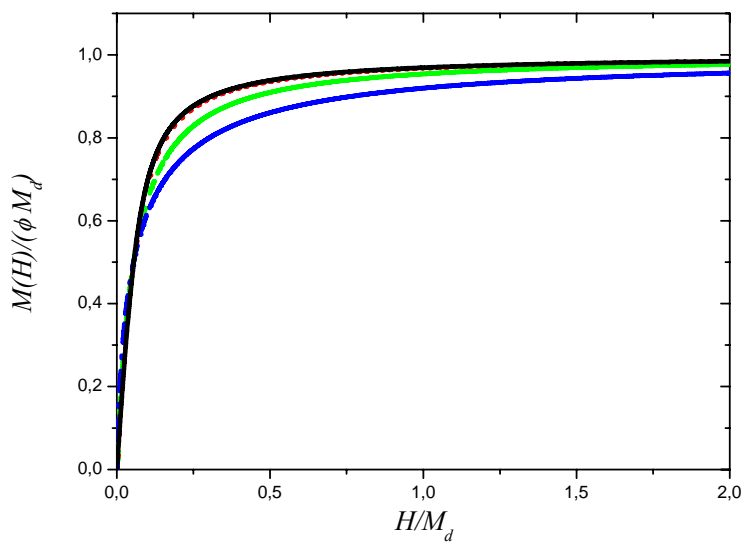
Figure 3.2. Fluid magnetization curves for magnetite particles with diameter d = 10 nm and values of σ of (solid) 0.0, (dotted) 0.1, (dashed) 0.3 and (dash-dotted) 0.5. T = 298.15 ºK.
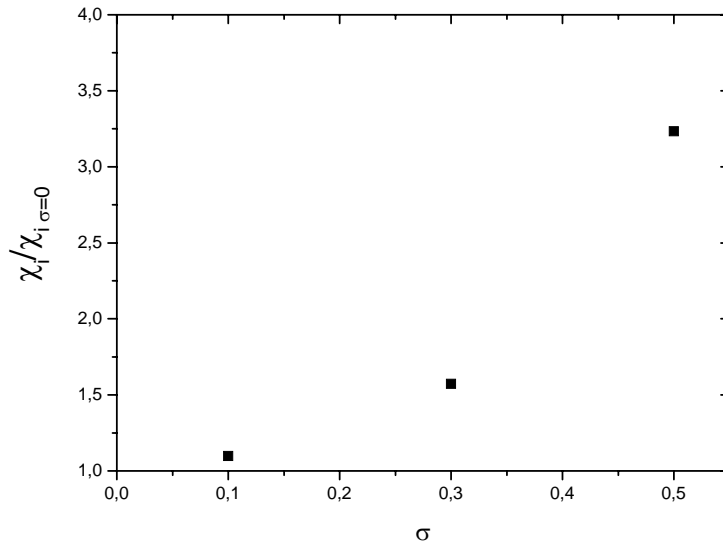
Figure 3.3. Initial susceptibility as function of the particle size polydispersity.

3.1.3 Magnetic body forces on magnetic nanofluids.

The total magnetic body force density acting on a magnetic nan-fluid in the presence of a magnetic field distribution is [Rosensweig, 1997]

$$\underline{f}_m = -\nabla \left[\mu_0 \int_0^H \left(\frac{\partial M v_f}{\partial v_f} \right)_{H,T} dH \right] + \mu_0 M(H) \nabla H \tag{3.15}$$

Here v_f and T are the volume and temperature of the fluid, respectively. The first term in equation (3.15) is a magnetostrictive term related to the changes of fluid density due to the applied magnetic field. If the fluid is considered incompressible, this term is neglected and equation (3.15) becomes

$$\underline{f}_m = \mu_0 M(H) \nabla H \tag{3.16}$$

In agreement with equation (3.16), to provoke the appearance of magnetic forces in an incompressible magnetic nanofluid, it is necessary to place it in the presence of a non-uniform magnetic field distribution.

3.1.4 Magnetic nanofluid viscosity

A magnetic nanofluid is a colloidal suspension which is expected to retain the Newtonian behavior of the continuum phase. The Newtonian viscosity of the suspension, η, increases with the particle volume concentration ϕ respect to the. For a suspension with volume concentration ϕ of spherical particles and continuum medium viscosity η_c, the relative viscosity can be approximated by the expression [Rosensweig, 1997]

$$\frac{\eta}{\eta_c} = \frac{1}{1 - \frac{5}{2}\phi + \left(\dfrac{\frac{5}{2}\phi_c - 1}{\phi_c^2} \right)\phi^2} \tag{3.17}$$

where ϕ_c is the maximum packing concentration. The particle coating used to stabilize the suspension against Van der Waals interactions increases the total volume of solid in the suspension. For an uniform coating of thickness δ, the solid volume increments by a factor $\left(1 + 2\delta/d\right)^3$. Including this effect in equation (3.17), the solution viscosity is found to be

$$\frac{\eta - \eta_c}{\eta\phi} = 1 - \frac{5}{2}\left(1 + \frac{2\delta}{d}\right)^3 + \left(\dfrac{\frac{5}{2}\phi_c - 1}{\phi_c^2} \right)\left(1 + \frac{2\delta}{d}\right)^6 \phi \tag{3.18}$$

Due to thermal fluctuations in the continuum medium, the particles in a colloidal suspension exhibit translational and rotational Brownian motion. Additionally, if a shear deformation is imposed to the suspension, hydrodynamic forces act on the particles having a similar effect to thermal forces. When a magnetic field is applied to a magnetic nanofluid subjected to a shear deformation, the magnetic particles in the fluid tend to remain rigidly aligned in the direction of the magnetic field. As a result, larger gradients in the velocity surrounding a particle are expected and viscous dissipation increases in the fluid. This magnetic contribution to the total viscosity is called rotational viscosity.

This contribution can be calculated as function of α (see equation (3.10)) using the Shliomis model mathematically expressed in equation (3.19) [Shliomis, 2001]

$$\frac{\eta_r}{\eta} = \frac{3}{2}\phi\frac{\alpha - \tanh\alpha}{\alpha + \tanh\alpha}$$ (3.19)

3.2 Reynolds theory for magnetic nanofluids.

Taken into account the discussion in previous sections, a magnetic nanofluid can be thought as a Newtonian fluid in which an additional force appears when it is placed in the presence of a magnetic field distribution. The motion of an incompressible magnetic Newtonian nanofluid can be described by the modified Navier- Stokes equation shown as follows;

$$\rho\left[\frac{\partial \underline{V}}{\partial t} + \underline{V} \bullet \nabla \underline{V}\right] = -\nabla p + \eta\nabla^2 \underline{V} + \rho\underline{g} + \mu_0 M(H)\nabla H$$ (3.20)

Equation (3.20) differs from equation (2.18) in the magnetic body force density expressed in equation (3.20).

We are interested in obtaining the Reynolds equation for a magnetic nanofluid. It is obtained by integrating the continuity and the modified Navier-Stokes equations under the lubrication approximation as decribed in section 2.3.1. Here again, the vector components of all the equations will be separated into their components perpendicular to the shearing plane (denoted by the suffix $\perp$) and those that lie on the cited plane (denoted by the suffix $\parallel$). In order to retain a problem where the pressure does not vary through the lubricant film, it will be supposed that the gradient of the magnetic field distribution has non-vanishing components only in the shearing plane. This condition can be expressed mathematically as

$$\nabla_{\perp}H = 0 .$$ (3.21)

The Navier-Stokes equation for a Newtonian fluid under the lubrication approximation given in equations (2.21) and (2.22), must include the magnetic body forces for a magnetic nanofluid, which, in agreement to equations (3.16) and (3.21), is

$$\underline{f}_{\|m} = \mu_0 M(H)\nabla_\| H \qquad (3.22)$$

and

$$\underline{f}_{\perp m} = 0 \qquad (3.23)$$

The modified Navier-Stokes equation for an incompressible Newtonian magnetic nanofluid under the lubrication approximation is

$$\nabla_\| p = \eta \nabla_\perp^2 \underline{V}_\| + \underline{f}_{\|m} \qquad (3.24)$$

and

$$\nabla_\perp p = 0 \qquad (3.25)$$

Equation (3.25) expresses mathematically that fluid pressure does not vary in the perpendicular direction to the shearing plane and then equation (3.24) can be analytically integrated through the fluid film to find expressions for the component of the velocity fluid profile lying on the shearing plane.

Considering the case represented in Figure 3.4, of two surfaces displacing with relative velocity V_{0x} and V_{0y} in the x and y directions, respectively. Then, the shearing plane for this problem is parallel to the plane x-y. The magnetic field strength H must be such as

$$H \equiv H(x, y) \qquad (3.26)$$

in order to satisfy the condition in equation (3.25). Then, in agreement with equations (3.22) and (3.26), the magnetic body force density on the fluid is

$$\underline{f} = \mu_0 M(H)\left[\hat{i}\partial_x + \hat{j}\partial_y\right]H \tag{3.27}$$
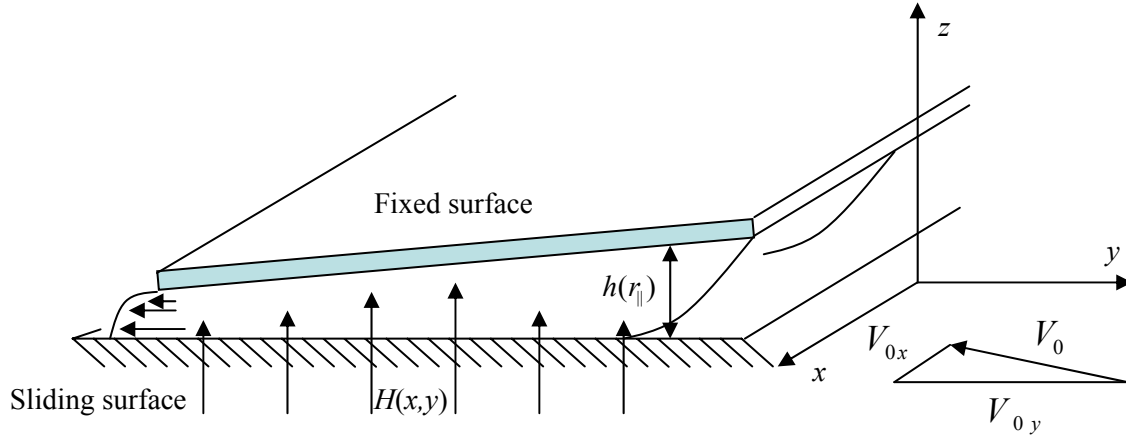
Figure 3.4 Surfaces separated by a magnetic nanofluid in the presence of a magnetic field $H(x,y)$. The bottom surface displaces with speed V_0 on the plane x-y, corresponding to the shearing plane.

The expressions for the components of the fluid velocity profile under the lubrication approximation are

$$V_x = \frac{h(x,y)}{2\eta}\left[\partial_x p(x,y) - \mu_0 M(H)\partial_x H\right] + \frac{V_{0x}z}{h(x,y)} \tag{3.28}$$

and

$$V_y = \frac{h(x,y)}{2\eta}\left[\partial_y p(x,y) - \mu_0 M(H)\partial_y H\right] + \frac{V_{0y}z}{h(x,y)} \tag{3.29}$$

Equations (3.28) and (3.29) are the solutions of the Navier-Stokes equation (3.24) for the fluid film of thickness $h(x,y)$ under no-slip boundary condition on the surfaces. They must also satisfy the continuity equation (2.10). Substituting equations (3.28) and (3.29) in the continuity equation and integrating the latter, we obtain the modified Reynolds equation for a magnetic nanofluid expressed in equation (3.34)

$$\partial_x\left[h^3(x,y)\partial_x p(x,y)\right]+\partial_y\left[h^3(x,y)\partial_y p(x,y)\right]=12\eta\left[V_{0x}\partial_x h(x,y)+V_{0y}\partial_y h(x,y)\right]$$
$$+\partial_x\left[h^3(x,y)\mu_0 M(H)\partial_x H\right]+\partial_y\left[h^3(x,y)\mu_0 M(H)\partial_y H\right]$$

(3.30)

The modified Reynolds equation for a magnetic nanofluid differs from the one for a Newtonian fluid only in the terms corresponding to the magnetic body forces. In the absence of a magnetic field or in the case that the magnetic field distribution is uniform, equation (3.30) reduces to equation (2.25).

Chapter4: Hydrodynamic lubrication between rigid tilted plates

Hydrodynamic lubrication theory is used to solve the problem of a contact of two, slightly tilted, flat rigid surfaces operating in the hydrodynamic lubrication regime, where one of surfaces rotates while the other is kept fixed. It is shown that theoretical results are in agreement with experimental ones available in literature. In addition, a method to estimate the misalignment between surfaces of a plate-plate rheometer is developed.

4.1 Introduction

Reynolds lubrication theory has been successfully used in the past to explain the hydrodynamic lubrication regime in different kinds of lubricated contacts including seals, journal and pad bearings. In this chapter, this theory is used to solve a problem consisting of a contact similar to the plate-plate rheometer, where the surfaces are slightly tilted. Only the flow in a misaligned cone-and-plate rheometer, where the axis is not perpendicular to the surface, has been investigated in full detail by the method of domain perturbation [Dudgeon, 1993]. For Newtonian fluids in a parallel-plate system, Taylor and Saffman [Taylor, 1957] found theoretically and Greensmith and Rivlin [Greensmith, 1953] experimentally that an extra pressure is exerted at the plate when the axis of rotation is not perfectly perpendicular to the fixed plate and that the pressure on the plate varies with position. In the aligned parallel plates, of course, there should be no such normal force for a Newtonian fluid [Walters, 1975]. It is our experience, however, that most parallel plate arrangements suffer from imperfections in parallelism between the plates [Bernzen, 2008]. It has been experimentally shown in the past that a small degree of non-parallelism can give rise to a large positive pressure in the converging flow region and a large negative pressure in the diverging flow region, superimposed on the pressure due to normal stress effects [Adams, 1964; Greensmith, 1953; Walters, 1975]. In this chapter we will show theoretical evidence of the effect of non-parallelism on thin film rheological measurements using plate-plate geometries. Theoretical results will be compared to experiments reported in the literature.

4.2 Theoretical modelling of rotating tilted plates

The problem solved in this chapter consists of describing the hydrodynamic lubrication regime of a contact composed of two rigid, flat, slightly tilted surfaces (see Figure 4.1), lubricated with an incompressible Newtonian fluid. The upper surface is commanded to rotate with angular speed Ω and the bottom is kept fixed. The film thickness at any point in the contact gap can be mathematically expressed as

$$h(r,\theta) = \varepsilon r \cos\theta + h_0 \qquad (4.1)$$

where

$$\varepsilon = (h_0 - h_{min})/R \qquad\qquad (4.2)$$

quantifies the plate misalignment, R is the plate radius, h_0 is the height at the midpoint in the contact and r and θ are the plate coordinates.
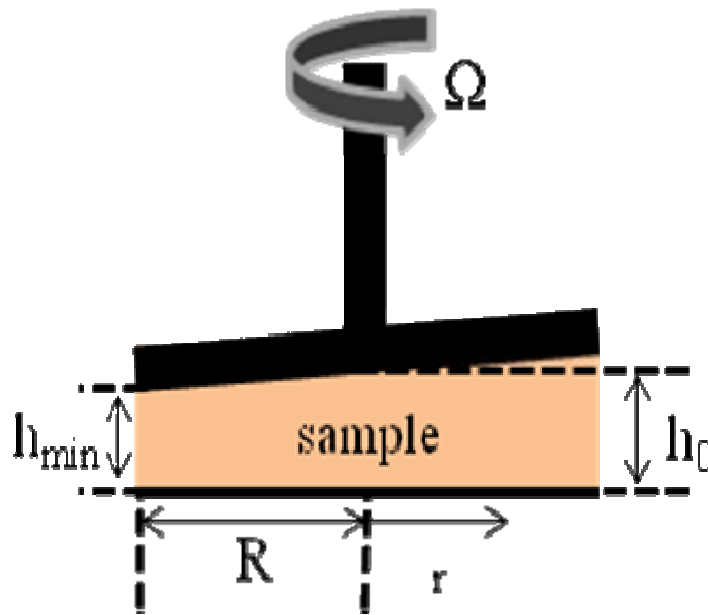
Figure 4.1. Schematic representation of two non parallel surfaces of radius R. The upper surface is commanded to rotate at a constant angular speed, while the lower is kept fixed. The gap between the plates is filled by a lubricant film characterized by the parameters h_{min} and h_0, corresponding to the minimum and central film thickness, respectively.

The hydrodynamic lubrication regime of the contact can be described by using the Reynolds lubrication theory assuming that the conditions of the lubrication approximation (discussed in section 2.3.1) are satisfied. The problem is then reduced to solving Reynolds equation (2.26) for the film shape given in equation (4.1) with the appropriate conditions on the manometric pressure $p(r,\theta)$ inside the gap. If the contact is supposed to be open to the atmosphere, pressure must satisfy the boundary conditions mathematically expressed in equation (4.3).

$$p(R,\theta) = 0 \tag{4.3}$$

Also, a condition of periodicity inside the gap must be imposed on the pressure. It is

$$p(\theta) = p(\theta + 2\pi) \tag{4.4}$$

In addition, the load capacity F_N of the contact, *i.e.* the load that the lubricant film must support, imposes another condition on the pressure as expressed mathematically in equation (4.5).

$$F_N = \int_0^R \int_0^{2\pi} p(r,\theta)r\,d\theta dr \tag{4.5}$$

The torque T needed to move the upper surface of the contact shown in Figure 2.1 can be calculated as

$$T = \int_0^R \int_0^{2\pi} \tau_{z\theta}(z = h)r^2\,d\theta dr \tag{4.6}$$

where $\tau_{z\theta}(z=h)$ is the shear stress acting on the fluid in contact with the rotating surface, as expressed in equation (2.4) this can be found as

$$\tau_{z\theta}(z = h) = \left.\frac{\partial V_\theta}{\partial z}\right|_{z=h} + \frac{1}{r}\left.\frac{\partial V_z}{\partial \theta}\right|_{z=h} \tag{4.7}$$

Here V_θ is the angular component of the fluid velocity, which under the lubrication approximation is given by equation (2.30). Substitution of this in equation (4.7) gives us the mathematical expression for $\tau_{z\theta}(z=h)$ shown in equation (4.8).

$$\tau_{z\theta}\big|_{z=h} = \left.\frac{\partial V_\theta}{\partial z}\right|_{z=h} = \frac{\eta\Omega r}{h(r,\theta)} + \frac{h(r,\theta)}{2r}\frac{\partial p(r,\theta)}{\partial \theta} \tag{4.8}$$

So far, we have presented the expressions needed to calculate the load capacity F_N and torque T acting in the contact after solution of the Reynolds equation. Their calculation may be simplified by using dimensionless variables, and also it may allow comparison with previous solutions of the lubrication equation. To do this, the set of dimensionless variables shown in equation (4.9) has been used.

$$r' = \frac{r}{R} \quad p' = \frac{pR^2}{F_N} \quad h' = \frac{h}{h_0} = \frac{\varepsilon}{h'_0} r' \cos\theta + 1 \quad h'_0 = \frac{h_0}{R} \tag{4.9}$$

It should be noted that, if the plates are consider to be always separated by the lubricant, then it must be satisfied that $0 \le \varepsilon / h'_0 < 1$.

With these dimensionless variables Reynolds equation (2.26) becomes

$$\frac{\partial}{\partial r'}\left[r' h'^3 \frac{\partial p'(r,\theta)}{\partial r'} \right] + \frac{1}{r'} \frac{\partial}{\partial \theta}\left[h'^3 \frac{\partial p'(r,\theta)}{\partial \theta} \right] = 6 A r' \frac{\partial h'}{\partial \theta} \tag{4.10}$$

where

$$A = \frac{R^2 \eta \Omega}{F_N h'^2_0} \tag{4.11}$$

The equation for the load capacity (4.5) can be rewritten as

$$\int p'(r',\theta) r' \, d\theta dr' = 1 \tag{4.12}$$

Simultaneous solution of equations (4.10) and (4.12) leads to a closed form relationship between the parameter A and the dimensionless film thickness h'.
It is also of interest to rewrite the variables related to the torque using dimensionless variables. The normalized shear stress is

$$\tau' = \frac{R^2 \tau}{F_N h'_0} = \frac{A r'}{h'(r,\theta)} + \frac{h'(r,\theta)}{2r'} \frac{\partial p'(r,\theta)}{\partial \theta} \tag{4.13}$$

and in consequence the dimensionless torque must be defined as

$$T' = \frac{T}{RF_N h'_0} = \int\limits_0^1 \int\limits_0^{2\pi} \tau' r'^2 \, d\theta dr' \tag{4.14}$$

Substituting equation (4.13) in (4.14) we find that the total normalized torque is

$$T' = T'_c + T'_p = \int\limits_0^1 \int\limits_0^{2\pi} d\theta dr' \frac{Ar'}{h'(r,\theta)} + \int\limits_0^1 \int\limits_0^{2\pi} d\theta dr' \frac{h'(r,\theta)}{2r'} \frac{\partial p'(r,\theta)}{\partial \theta} \tag{4.15}$$

where two contributions can be distinguished, these are the Couette and Pousseuille normalized torques, corresponding to the first and second integral terms respectively. Equation (4.15) represents a relation between the torsional and normal forces acting on the contact, which can be determined by solving the Reynolds equation given values for the fluid viscosity η, angular speed Ω, central film thickness h_0 and plate misalignment ε.

Reynolds equation was solved using a finite difference numerical method, with the resulting matrix being solved by Gauss-Seidel iteration using the Reynolds boundary conditions [Khonsari, 2001]. If the pressure at any point of the contact takes a negative value during the cycle of iterations this is replaced by zero. This restricts the pressure to take only positive values.

To apply the method of finite differences, the area of integration must be divided into a mesh containing points regularly spaced a distance Δr and $\Delta \theta$ apart in the radial and angular directions respectively. Then a point (i , $j)$ in the mesh corresponds to a point $r_i = i\Delta r$ and $\theta_j = j\Delta \theta$ inside the contact. The first and second order derivatives in equation (4.10) at the point of the mesh (i , $j)$ must be approximated as follows:

$$\frac{\partial p(r,\theta)}{\partial r} = \frac{p_{i+1,j} - p_{i-1,j}}{\Delta r} \tag{4.16}$$

$$\frac{\partial p(r,\theta)}{\partial \theta} = \frac{p_{i,j+1} - p_{i,j-1}}{\Delta \theta} \tag{4.17}$$

$$\frac{\partial^2 p(r,\theta)}{\partial r^2} = \frac{p_{i+1,j} - 2p_{i,j} + p_{i-1,j}}{\Delta r^2} \tag{4.18}$$

and

$$\frac{\partial^2 p(r,\theta)}{\partial \theta^2} = \frac{p_{i,j+1} - 2p_{i,j} + p_{i,j-1}}{\Delta \theta^2} \tag{4.19}$$

Using equations (4.16) to (4.19) on (4.10) we obtain the set of simultaneous equations

$$A_{i,j} p_{i+1,j} + B_{i,j} p_{i-1,j} + C_{i,j} p_{i,j} + D_{i,j} p_{i,j+1} + E_{i,j} p_{i,j-1} = R_{i,j}, \tag{4.20}$$

where the coefficients are:

$$A_{i,j} = \frac{1}{\Delta r^2} + \frac{1}{2\Delta r}\left(\frac{1}{r_i} + \frac{3}{h(r_i,\theta_j)}\frac{\partial h}{\partial r}(r_i,\theta_j)\right) \tag{4.21}$$

$$B_{i,j} = \frac{1}{\Delta r^2} + \frac{1}{2\Delta r}\left(\frac{1}{r_i} - \frac{3}{h(r_i,\theta_j)}\frac{\partial h}{\partial r}(r_i,\theta_j)\right) \tag{4.22}$$

$$C_{i,j} = -2\left(\frac{1}{\Delta r^2} + \frac{1}{r_i^2 \Delta \theta^2}\right) \tag{4.23}$$

$$D_{i,j} = \frac{1}{r_i^2 \Delta \theta^2} + \frac{3}{2r_i^2 (\Delta\theta) h(r_i,\theta_j)}\frac{\partial h}{\partial \theta}(r_i,\theta_j) \tag{4.24}$$

$$E_{i,j} = \frac{1}{r_i^2 \Delta \theta^2} - \frac{3}{2r_i^2 (\Delta\theta) h(r_i,\theta_j)}\frac{\partial h}{\partial \theta}(r_i,\theta_j) \tag{4.25}$$

$$R_{i,j} = -\frac{6\eta\Omega}{h^3(r_i,\theta_j)}\frac{\partial h}{\partial \theta}(r_i,\theta_j) \tag{4.26}$$

To solve Reynolds equation, the integration area was divided in a mesh of $(i,j) = 200x100$ points. Increasing the number of points beyond this had no significant further effect on the results. The details related to the algorithm used to this solution are shown in the Appendix I.

4.3 Results and Discussion

4.3.1. Normal force in the contact

The numerical solution of Reynolds equation gives a relation of the form

$$A^{-1} = \frac{F_N h'^2_0}{R^2 \eta \Omega} = f(h')$$
(4.27)

where *h'* depends only on the ratio ε / h'_0, thus $f(h') = \left(\dfrac{\varepsilon}{h'_0} \right)$.

It can be observed in equation (4.27) that the load capacity and the product $\eta\Omega$ keeps a linear relation, whose proportionality constant depends on both the dimensionless central film thickness and the relative plate misalignment characterized by ε. Reynolds equation was solved as explained in section 4.2.3, for a wide range of ε / h'_0 from $1x10^{-2}$ to 0.95 and the results are shown in Figure 4.2. Over the whole range covered, the load capacity increases with the relative plate tilt while decreasing with film thickness. For values of ε / h'_0 up to approximately 0.2, a linear dependence is observed with A^{-1}. In this range, the load capacity is proportional to ε and it has a reciprocal dependence on h_0^3. For larger values of ε / h'_0, the load capacity increases more rapidly, with what it seems to be a power law. When the misalignment is close to the value of the medium film thickness, the load capacity becomes the most sensitive to any change of both the plate tilt ε and film thickness h_0. To give an approximate mathematical expression for *f(h')* in equation (4.27), a three parameter equation of the form

$$f\left(\frac{\varepsilon}{h'_0}\right) = \left(1 - \frac{\varepsilon}{h'_0\,\alpha}\right)^{\beta} - 1 + \gamma\frac{\varepsilon}{h'_0} \tag{4.28}$$

was used to fit the results. The best fit parameters were found to be $\alpha = 1.018 \pm 0.001$, $\beta = 0.196 \pm 0.0012$ and $\gamma = 5.915 \pm 0.002$.
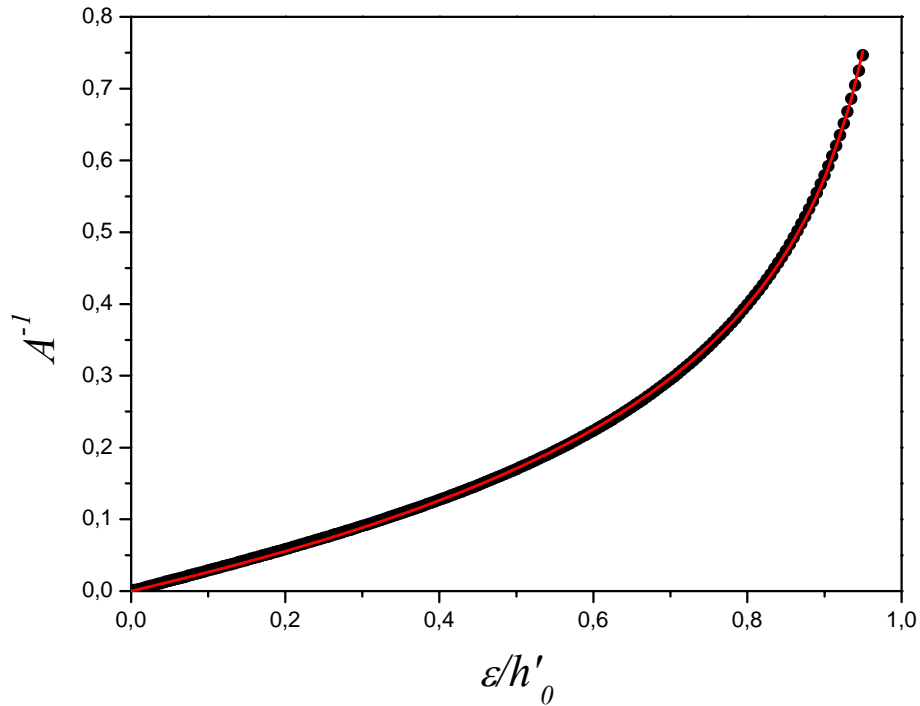
Figure 4.2. Theoretical results showing the dependence among all the parameters included in the Reynolds equation. The red line corresponds to the fit obtained using equation (4.28).

4.3.2. Friction forces between the surfaces

4.3.2.1 Couette torque

When the surfaces are completely parallel to each other ($\varepsilon = 0$) and separated by a fluid film of thickness h_c, the total torque is given by [Steffe, 1992]

$$T_{\varepsilon=0} = \frac{\pi}{2}\frac{\eta\Omega R^4}{h_c} \tag{4.29}$$

The Couette torque T_c is not related to the hydrodynamic pressure generated in the film but to the geometrical aspect of the contact established for the relative plate tilt ε/h'_0. This change is to be studied by means of the ratio of the actual Couette torque T_c and the torque in parallel plates $T_{\varepsilon=0}$ given by equation (4.29). This ratio is shown in Figure 4.3 as function of ε/h'_0. The change in the Couette torque is negligible for values of ε/h'_0 up to 0.2. For larger values of ε/h'_0, T_c increases slowly relatively to $T_{\varepsilon=0}$, until an abrupt increment is found approximately at $\varepsilon/h'_0 = 0.8$. Finally, when ε is the 95% of the central film thickness the value of T_c is approximately double $T_{\varepsilon=0}$.
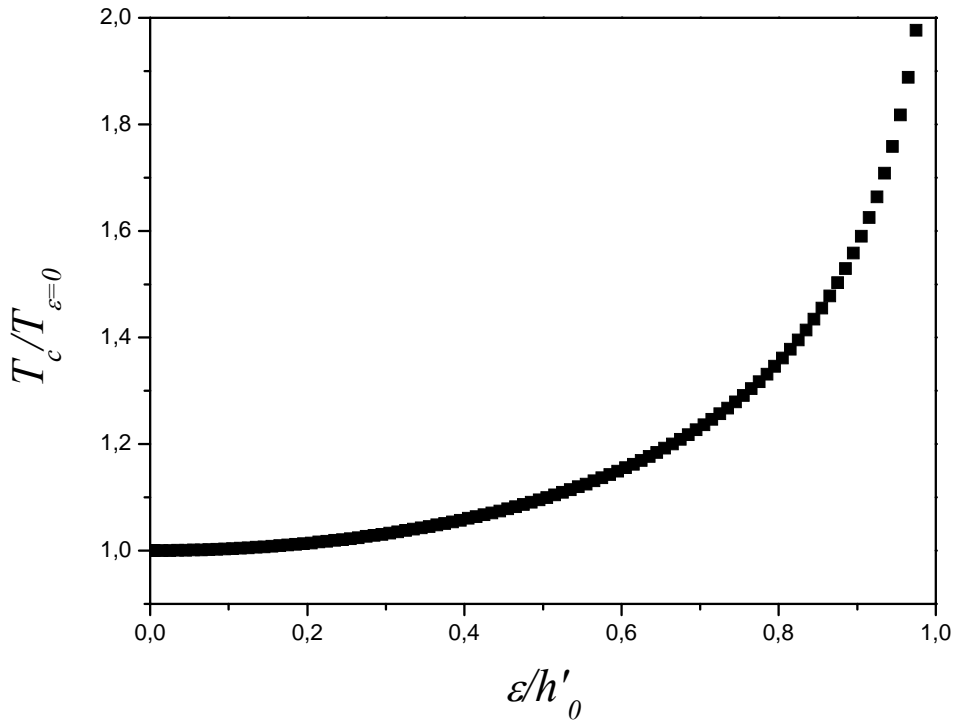
Figure 4.3. Ratio of actual Couette torque to its parallel plate value as function of the relative plate tilt.

4.3.2.2. Poiseuille torque

As shown in Figure 4.4 the normalized Poiseuille torque T'_p, previously defined in equation (4.15), grows proportionally with ε/h'_0, for values of the later up to 0.9,

where the former reaches a plateau about a value of 0.523. At this value, the value of T'_p represents 4.25% of the total torque.

As the Poiseuille torque is proportional to the angular derivative of the pressure, its behaviour can be visualized with the help of Figure 4.5, where the normalized pressure distributions corresponding to values of ε / h'_0 of 0.05, 0.5, 0.75 and 0.95 are shown. A Cartesian reference frame is used for discussion of results. For the lowest relative plate tilt, the distribution appears to be symmetrical with respect to the y-axis and then the Poisseuille contribution to the torque is negligible. As ε / h'_0 is increased, the maximum value of the distribution increases as shifted to the position of minimum film thickness ($x = -R$), breaking the symmetry and giving rise to higher values of the Poisseuille torque.
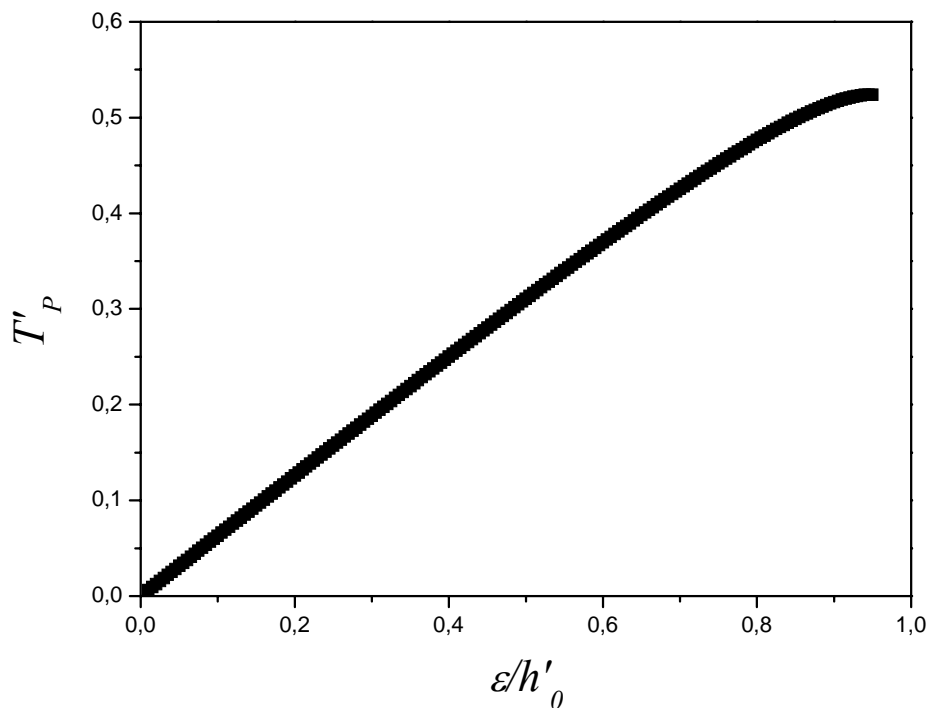
Figure 4.4. Normalized Poiseuille torque as function of the relative plate tilt.

$\dfrac{\varepsilon}{h'_0} = 0.05$ $\dfrac{\varepsilon}{h'_0} = 0.5$

$\dfrac{\varepsilon}{h'_0} = 0.75$ x + $\dfrac{\varepsilon}{h'_0} = 0.95$

y -   y +

x -
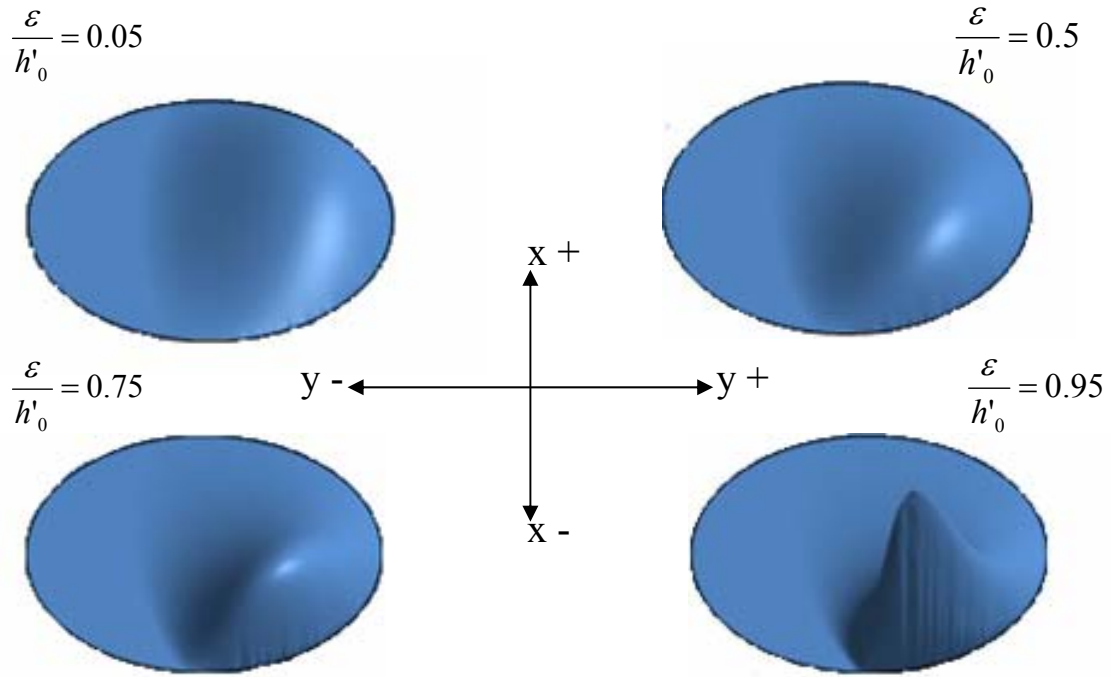
Figure 4.5. Hydrodynamic pressure distribution generated on the lubricant film between the plates.

4.3.2.3. Total torque

The total normalized torque containing Poiseueille and Couette contributions is shown in Figure 4.6. This curve suggests that the highest frictions are found for the lowest values of ε / h'_0, where the poorest performance of lubrication forces is expected. A fit to curve was carried out, using a three parameter expression:

$$T' = \cfrac{1}{\left(1 - \dfrac{\varepsilon}{h'_0 \, \alpha'}\right)^{\beta'} - 1 + \gamma' \dfrac{\varepsilon}{h'_0}} \qquad (4.30)$$

where $\alpha' = 1.067 \pm 0.002$, $\beta' = -0.021 \pm 0.001$ and $\gamma' = 0.0357 \pm 0.0002$.
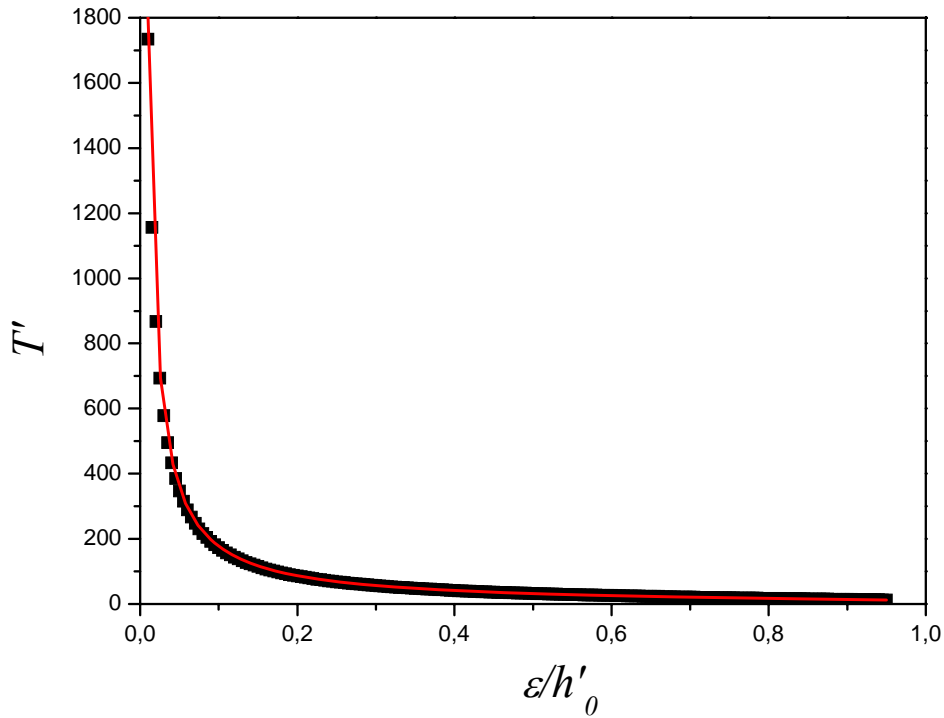
Figure 4.6. Normalized total torque as function of the relative plate tilt.

4.3.3 Stribeck Curve

As discussed in section 2.4, the performance of a lubricated contact can be described properly with respect to the so-called Stribeck curve. On the one hand, for this contact an appropriate form for the Gumbel number is

$$Gu = \frac{\pi R^2 \eta \Omega}{F_N} \tag{4.32}$$

and using equations (4.27) and (4.28) the Gumbel number Gu can be related to the central film thickness h_0' and the misalignment parameter ε by

$$Gu = \frac{\pi h_0'^2}{\left(1 - \dfrac{\varepsilon}{h_0' \alpha}\right)^{\beta} - 1 + \gamma \dfrac{\varepsilon}{h_0'}} \tag{4.33}$$

Here α, β and γ correspond to the constants in equation (4.28).

On the other hand, the friction coefficient for a torsion force must be defined in terms of the applied torque. For this geometry, the friction coefficient is defined in equation (4.34).

$$\mu = \frac{2T}{RF_N} \tag{4.34}$$

Introducing equations (4.14) and (4.30) into (4.34), the friction coefficient is found to be

$$\mu = \frac{2h'_0}{\left(1 - \frac{\varepsilon}{h'_0 \, \alpha'}\right)^{\beta'} - 1 + \gamma' \frac{\varepsilon}{h'_0}} \tag{4.35}$$

Here α', β' and γ' corresponds to the constants in equation (4.30).

Equations (4.33) and (4.35) are the parametric representations of a Stribeck curve equivalent to a typical tribo-rheological experiment, where a normal force is applied to the plates and the torque required to rotate the plates at a given angular speed is monitored. Given a value for ε, a Stribeck curve can be built, where every point corresponds to only one value of the central film thickness h_0.

Definitions in equations (4.32) and (4.34) were chosen to allow the comparison of the model developed here with experimental results available in literature. [Kavehpour, 2004] studied the performance of lubrication forces in a parallel plate tribometer. They estimated an effect of eccentricity of approximately 25 μm (ε=25x10^{-4}). Their results reveal the appearance of lubrication forces largely enough to find well-defined hydrodynamic lubrication regions in their Stribeck curves. Figure 4.7 shows the hydrodynamic lubrication regime of an experimental Stribeck curve, where the applied load was 10 N and the lubricant was a Pennzoil oil with Newtonian viscosity of 700 mPa·s. Theoretical Stribeck curves are also shown, corresponding to four different values of ε between 4x10^{-4} and 1x10^{-4}. The best agreement between experimental and theoretical curves was found for $\varepsilon = 2$x10^{-4} corresponding to $h_0 - h_{min}$=20 μm, which is close to the eccentricity in the experimental set-up.
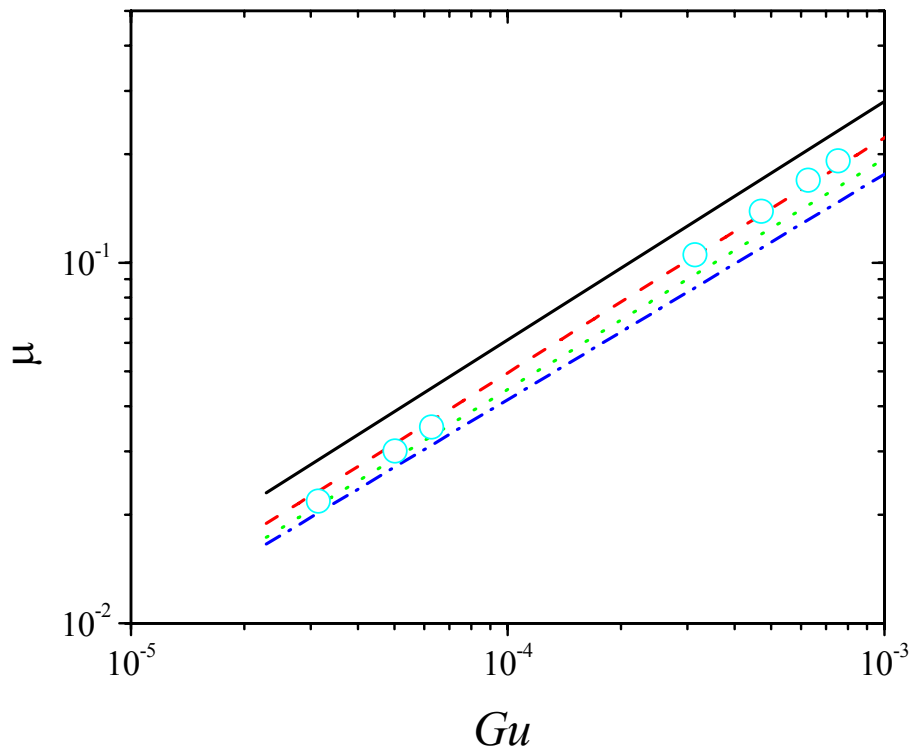
Figure 4.7. Stribeck curves for sheared Newtonian fluids. The model is represented in lines for values of ε of (solid) 0.0001, (dash) 0.0002, (dot) 0.0003 and (dash dot) 0.0004. Open circles correspond to experimental results obtained by [Kavehpour, 2004, Fig. 4, page 333].

4.4 Application in rheometry: estimation of non-parallelism on a plate-plate rheometer.

As previously discussed in the introduction section, in most plate-plate rheometer geometries a small misalignment will be present between the surfaces when they are at a very close distance (see Figure 4.1). As shown in section (4.3.2), the total torque measured in the rotating plate of a plate-plate rheometer suffers deviations from the expected value for perfect parallel geometries. The deviation becomes larger with both an increase of misalignment between the surfaces or a decrease of the central gap h_0 between the surfaces.

The model developed in this chapter represents an alternative to estimate the value of the mentioned error in the geometry [Andablo-Reyes, 2010-1]. The parameter A and the normalized torque T' given in equations (4.27) and (4.30), respectively represent a set of two equations with two variables whose values must be determined, once the rest of the parameters load capacity F_N, torque T, plate diameter R, fluid viscosity η, and angular velocity Ω of the rotating plate have been measured or set. To facilitate the solution of the set of equations for A and T', the combination of these quantities shown in equation (4.36) was introduced.

$$1/AT'^2 = R^4 F_N \eta \Omega / T^2 \qquad (4.36)$$

The convenience of using equation (4.36) is that, in agreement to equations (4.27) and (4.30), the combination of variables shown in (4.36) depends only on the ratio ε/h'_0. Figure 4.8 shows the functional dependence between the mentioned ratio and the measurable variables together to the best fit to the shown data. The mathematical relation between the measurable parameters and the ratio ε/h'_0 is

$$\frac{\varepsilon}{h'_0} = \left[1 - 1.11 \frac{R^4 F_N \eta \Omega}{T^2}\right]^{-0.04314} + 8.136 \frac{R^4 F_N \eta \Omega}{T^2} - 1 \qquad (4.36)$$

Introducing all the measured values for all the parameters in equation (4.36) a value for ε/h'_0 is found. The latter must be used either in equation (4.27) or (4.30) to find the value of h_0 and then a value for ε.
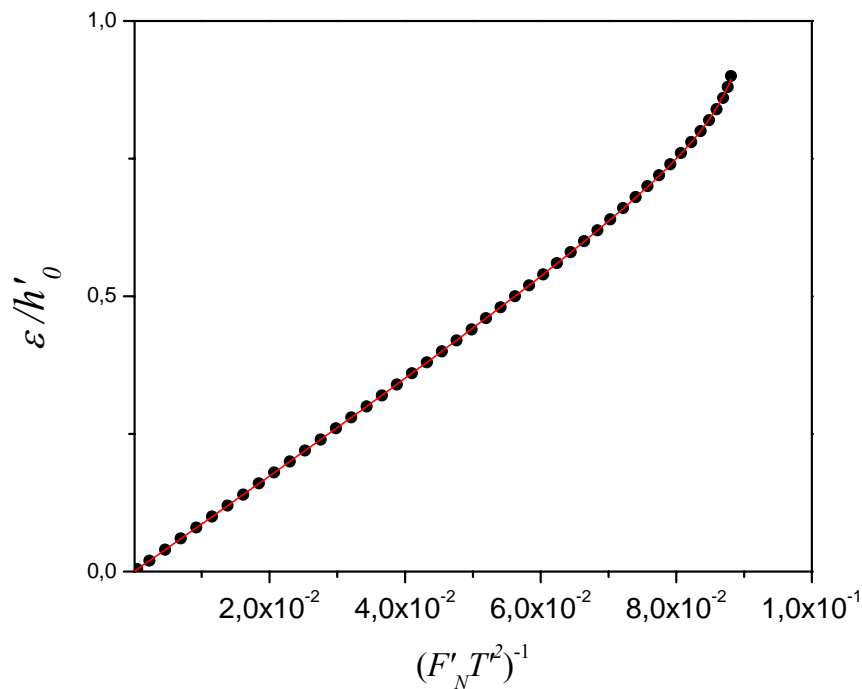
Figure 4.8. Relation between measurable parameters and the ratio ε/h'_0. The solid line corresponds to the best fit to the data.

4.5 Chapter conclusions

In agreement with Reynolds lubrication theory, the non-parallelism in plate-plate rheometers provokes the appearance of lubrication forces in the fluid film between the plates. The magnitude of the normal force appearing on the rotating plate is directly proportional to the angular speed and the fluid viscosity. The proportionality constant increases with relative tilt of the plates and decreases with the fluid film thickness. The Stribeck curve model presented here successfully explains results of tribo-rheological experiments available in the literature. The model presented in this chapter allows estimation of the misalignment between the surfaces in a plate-plate rheometer.

Chapter 5: Ferro-hydrodynamic lubrication in a contact of tilted rigid plates

The hydrodynamic lubrication regime of a contact of slightly tilted surfaces lubricated with a magnetic nanofluid was studied under the action of an externally-applied magnetic field distribution. Experiments were carried out in a plate-plate magnetorheometer and the modified Reynolds theory for magnetic fluids was employed for theoretical modeling of the contact, imposing cavitation conditions on the fluid film. Both theory and experiment showed that the friction on the contact can be controlled by means of modifying the strength of the applied magnetic field. The control mechanism is directly associated to an additional contribution to the load capacity due to the magnetic forces acting on the magnetic nanofluid.

5.1 Introduction

The shearing and hydrodynamic forces acting on a lubricated contact working in the hydrodynamic lubrication regime have a close relationship, which is determined by the contact design variables and the operating conditions. Usually, the operating conditions are imposed by the needs of the application where the contact is being used, and thus the friction acting on it during operation depends completely on its design, which may include clever modifications from the standard model to improve its performance, reducing its operating friction. An example of this is the inclusion of self-adjustable surfaces in journal and pad bearings in order to enable a control mechanism for the hydrodynamic forces, depending on the needs established by the operating conditions.

Magnetic nanofluids offer another alternative to control the performance of the lubrication of a contact and the friction between their surfaces *via* an external variable independent of the operation conditions. Previous theoretical studies have concluded that the body forces acting on the magnetic fluid when this is placed in presence of a non-uniform magnetic field distribution can modify the strength of the lubricant film, increasing the load capacity of the contact [Walker, 1979; Shah, 2004; Naduvinamani, 2009; Kuzhir, 2007]. Based on the dearth of comparison between theory and experimental evidence in current literature of the performance of magnetic nanofluids as lubricants, this work has as a main objective to study experimentally and theoretically the problem of a simple contact lubricated with a magnetic nanofluid. The experimental study will be carried out using a plate-plate magnetorheometer, which geometrically corresponds to the contact studied in the previous chapter. In addition, the modified Reynolds equation for magnetic nanofluids will be used to describe the performance of the lubrication forces in the contact.

5.2 Experimental section

5.2.1 Magnetic nanofluids

Magnetic nanofluids used in this work were bought from FerroTec Inc., and are stable suspensions of magnetite particles (M_d = 447 kA/m) in ester based oils. All of them have the same saturation magnetization in agreement with the data provided by the

manufacturer. In order to corroborate all the data previously mentioned and to obtain more information about the composition of the suspension, shear flow and magnetization measurement experiments were carried out.

The objective of the shear flow experiments was to corroborate that the magnetic nanofluids have a Newtonian behavior and to obtain more reliable data for their Newtonian viscosities. These experiments were carried using a Cone-Plate rheometer CP50-1 of Anton Paar, which is schematically represented in Figure 5.1. The cone angle is $\theta = 1°$ and its radius $R = 25$ mm. All the tests were carried out at temperature of 25 °C.
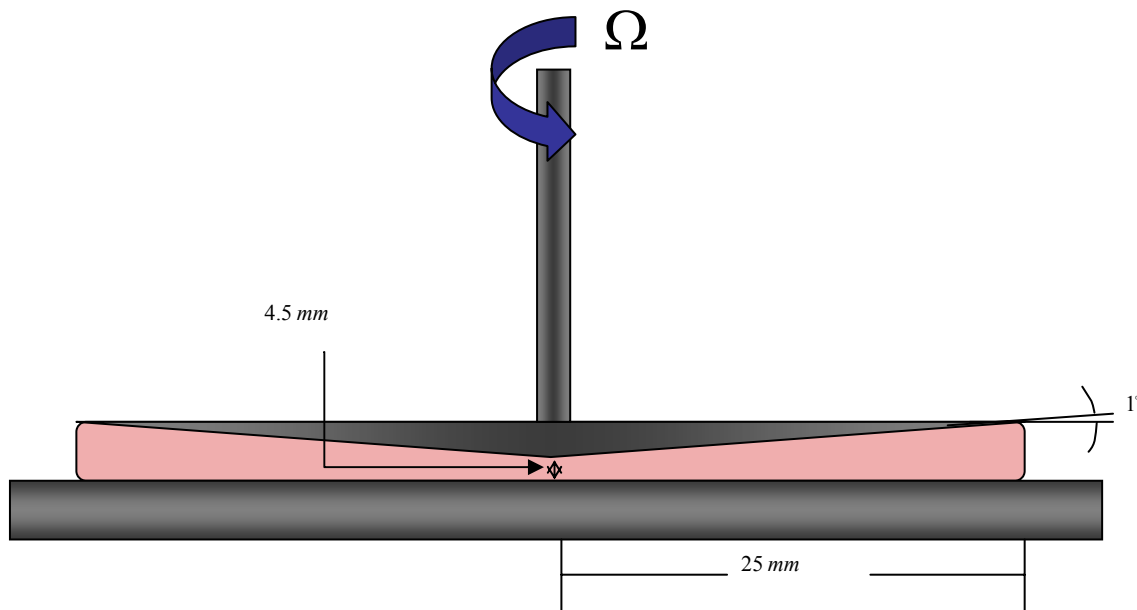
Figure 5.1. Schematic representation of a cone-plate rheometer.

When the cone rotates with angular velocity Ω and the plate is fixed, the shear rate $\dot{\gamma}$ at any point inside the gap between these surfaces is [Steffe, 1992]

$$\dot{\gamma} = \frac{\Omega}{\tan\theta} \tag{5.1}$$

In a cone-plate rheometer, the shear rate is independent of the radial distance from the gap centre. Thus, the shear stress is also uniform along the gap and is related to the total torque T measured on the cone as

$$\tau = \frac{3T}{2\pi R^3} \qquad\qquad (5.2)$$

The shear stress as function of the shear rate is shown in Figure 5.2 for the three different fluid viscosities. As expected for Newtonian fluids, a linear relation is found between the variables previously mentioned. The slopes of these lines correspond to the fluid viscosities, which were found to be 46, 200 and 560 mPa·s.
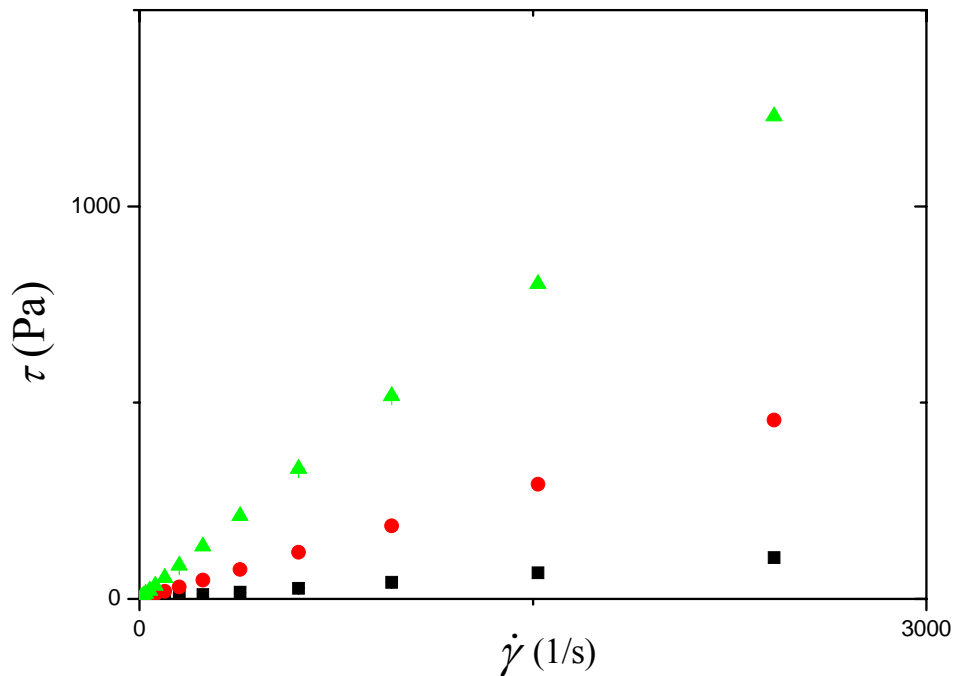
Figure 5.2. Shear flow curves obtained for the magnetic nanofluids used in this work using a cone-plate rheometer . This curves show linear behavior between shear stress τ and shear rate $\dot{\gamma}$ as expected for Newtonian fluids. They correspond to fluid viscosities of (squares) 46, (circles) 200 and (triangles) 560 mPa·s.

Curves for the magnetization of the magnetic nanofluids used in this work were obtained using a Quantum Design (San Diego, CA) MPMS-XL 5.0 Tesla magnetometer. The magnetization curves are shown in figure 5.3. All of them show a similar behavior, with similar initial susceptibility and saturation magnetization. The experimental data

were contrasted with the Langevin magnetization model assuming that the particle size satisfies a log normal distribution. All the details are given in Chapter Three, subsection 3.2.2. For this model the fitting parameters are the initial magnetic susceptibility χ_i, the magnetization saturation M_s, and the standard deviation σ of the particle size distribution. The latter quantifies the polydispersity in the particle size. The results of the model are presented together the experimental curves in Figure 5.3, and the values of the fitting parameters are given in Table 1. The Langevin model captures satisfactorily the real magnetic response of all the fluids. Nicely, it can be observed that the values of the fitting parameters are very similar for all the curves.
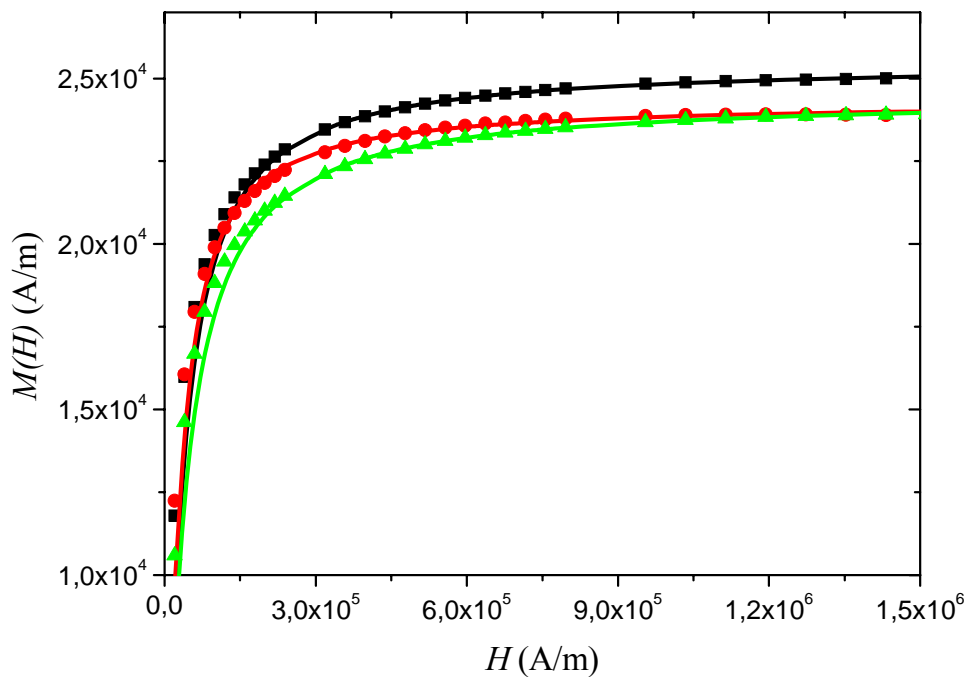
Figure 5.3. Magnetization curves for magnetic nanofluids with Newtonian viscosities of (squares) 46, (circles) 200 and (triangles) 560 mPa·s. The solid lines correspond to the fitted Langevin model of magnetization for polydisperse suspensions.

Fluid viscosity (mPa·s)	Fluid saturation magnetization Ms (A/m)	Initial susceptibility χ_i	Particle concentration ϕ	Particle size polydispersity σ	Particle diameter d(nm)
46	25485	0,5933	0,057	0,25	8,98
200	24316	0,6152	0,054	0,2	9,52
560	24457	0,5325	0,054	0,28	8.59

Table 1. Properties of magnetic nanofluids used in this work obtained from adjusting the Langevin model.

5.2.2 Experimental set-up

All the experimental results of lubrication shown in this chapter were obtained using the commercial magnetorheological plate-plate rheometer MCR-501 of Anton Paar, which is schematically shown in Figure 5.4. The geometry is provided of a magnetic circuit which generates a non uniform magnetic field distribution inside the gap between the plates. The magnetic field strength is controlled by the electric current fed to the coil in the magnetic circuit as is shown in Figure 5.5. A maximum current of 5 amperes can be applied to the coil, corresponding to a magnetic field distribution with maximum field strength of approximately 885 kA/m,.

The hydrodynamic lubrication experiments were carried out in a similar fashion to rheological flow tests. The upper plate was rotated with angular velocity Ω at a fixed gap distance and a fixed magnetic field strength. All the flow tests were carried out at a controlled temperature T of 25 ºC in order to obtained isothermal conditions. The angular speed was swept from zero up to 150 rad/s. The torque and normal force on the upper plate were measured with a precision of 0.01 μNm and 0.01 N, respectively. The upper plate is made of titanium, thus no magnetic force is directly exerted on it by the magnetic field.

As schematically represented in Figure 5.4, inside of the contact the upper surface is divided in three levels, an inner circular surface with radius of 10 mm, followed by a circular furrow with 0.75 mm of depth with respect to the inner surface, and 7 mm width that finishes at a ring of 0.3 mm of height. The reason for the existence of this furrow is to keep any excess of fluid out of the inner gap.

Using a clock dial with a fine grating, concentricity error was measured to be less than $2\mu m$ and misalignment was found to be $h_0 - h_{min} = 1.75\mu m$. The set value h' and real

gap distance h are not exactly the same, and an error Δh is commonly obtained. The gap error between plates was carefully evaluated in shear flow experiments using a semi-empirical procedure [11, 12]. This approach assumes that the sum of the set gap and the gap error gives the real gap ($h = h' + \Delta h$). Hence, the following equation holds: $h\eta/\eta_c = h + \Delta h$, where η_c is the measured viscosity based on the set gap and η is the true viscosity. A gap error of Δh = 18 μm is obtained by plotting h_c/η_c against the commanded gap h_c for a range of Newtonian silicone oils.
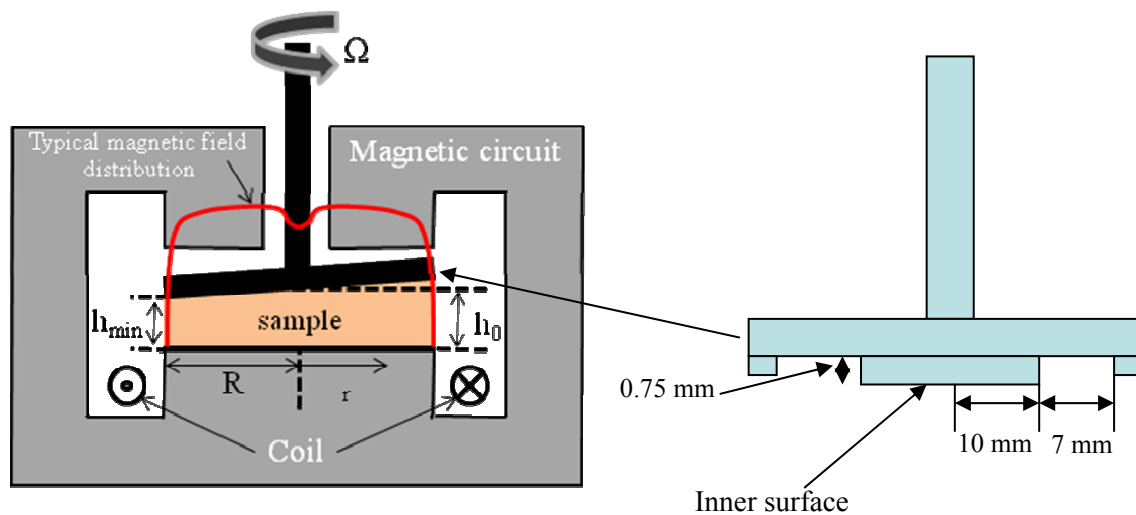
Figure 5.4. Schematic representation (not to scale) of the misalignment in a parallel plate geometry (face seal). The device is adapted for the application of an external magnetic field with strength up to ~ 800 kA/m by using an external magnetic circuit. A non-uniform magnetic field distribution exists in the contact due to the hole bored through the magnetically soft permeable material. Additionally a transverse cut of the upper surfaces is shown.

Plate rim
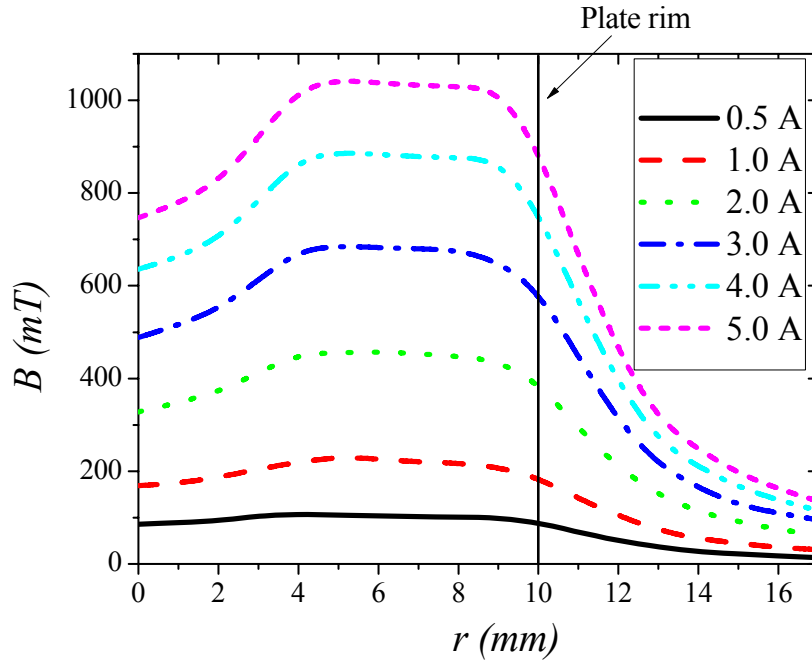
Figure 5.5. External magnetic field density distribution, B, as a function of radial distance r, in the mechanical face seal for a wide range of electric currents applied to the electromagnet.

5.3 Modeling the contact

The problem to be solved here is geometrically the same one solved in Chapter Four. Flat rigid surfaces that are relatively tilted are supposed to be separated by a lubricating pressurized film that supports a load F_N. But now the contact gap is filled with a magnetic nanofluid and a non-uniform magnetic field distribution which depends only on the radial coordinate r is generated inside the gap, as shown in figure 5.5. The magnetic nanofluid is expected to behave like a perfect Newtonian fluid in both the absence and in the presence of the magnetic field. Basically, the magnetic field does not modify the fluid viscosity η further than the changes expected for the rotational viscosity [Shliomis, 2001]. The fluid film pressure will be the combination of hydrodynamic and magnetic forces. The latter offers the advantage of manipulability by the externally applied magnetic field.

The contact schematically presented in Figure 5.4 will be theoretically modeled in this work using the Reynolds modified theory for magnetic nanofluids. In agreement with equation (3.16), the magnetic body forces acting on the magnetic nanofluid in the

presence of a magnetic field distribution whose strength depends only on the radial coordinate are given by

$$\underline{f}_{rm} = \mu_0 M(H)\hat{r}\partial_r H(r) \tag{5.3}$$

where $\mu_0 = 4\pi \times 10^{-7}$ $T/A \cdot m$ is the vacuum permeability, $M(H)$ is the fluid magnetization and $H(r)$ is the magnetic field strength at a distance r from the contact centre.

In agreement to equation (3.24), the appropriate Navier-Stokes equation under the lubrication approximation to describe this problem is

$$\partial_r p(r,\theta) = \eta \partial_z^2 V_r + \mu_0 M(H)\partial_r H(r) \tag{5.4}$$

and

$$\frac{1}{r}\partial_\theta p(r,\theta) = \eta^2 \partial_z^2 V_\theta \tag{5.5}$$

The result of integrating equations (5.4) and (5.5) through the lubricant film (z direction) under no-slip conditions on the surfaces are the expressions for the fluid velocity inside the contact given in equations (5.6) and (5.7).

$$V_r = \frac{1}{2\eta}\left[\partial_r p(r,\theta) - \mu_0 M(H)\partial_r H(r)\right]\left[z^2 - hz\right] \tag{5.6}$$

$$V_\theta = \frac{1}{2\eta r}\partial_\theta p(r,\theta)\left[z^2 - hz\right] + \frac{r\Omega z}{h} \tag{5.7}$$

In equations (5.6) and (5.7), $h(r,\theta)$ is the thickness of the fluid film separating the contact surfaces. For this contact

$$h(r,\theta) = \varepsilon r \cos\theta + h_0 \tag{5.8}$$

where

$$\varepsilon = (h_0 - h_{\min})/R \tag{5.9}$$

quantifies the plate misalignment, R is the plate radius, h_0 is the height at the midpoint.

Finally, in order to find the Reynolds equation to describe our problem, the continuity equation must be integrated through the fluid film using equations (5.6) and (5.7).

$$\partial_r \left[rh^3 \partial_r p(r,\theta) \right] + \frac{1}{r} \partial_\theta \left[h^3 \partial_\theta p(r,\theta) \right] = 6\eta\Omega r \partial_\theta h(r,\theta) + \partial_r \left[rh^3 \mu_0 M(H) \partial_r H(r) \right] \tag{5.10}$$

Here, $p(r,\theta)$ represents the total fluid manometric pressure which includes the hydrodynamic and magnetic forces contributions. This may be mathematically expressed as

$$p(r,\theta) = p_H(r,\theta) + p_m(r) \tag{5.11}$$

Here, $p_H(r,\theta)$ and $p_m(r)$ represent the pressure in the fluid film generated due to hydrodynamic and magnetic forces, respectively. The latter can be easily found by integrating equation (5.10) under static conditions ($\Omega=0$). Assuming that the contact is open to the atmosphere at the edge of the fluid film the total pressure must satisfy that

$$p(R_1,\theta) = 0 \tag{5.12}$$

where R_1 is the radius at the edge of the fluid film. It can be obtained that

$$p_m(r) = \mu_0 \int_{R_1}^{r} M(H)H(r)dr \tag{5.13}$$

Introducing equations (5.11) and (5.13) in equation (5.10), the latter reduces to

$$\partial_r \left[rh^3 \partial_r p_H(r,\theta) \right] + \frac{1}{r} \partial_\theta \left[h^3 \partial_\theta p_H(r,\theta) \right] = 6\eta\Omega r \partial_\theta h(r,\theta) \tag{5.14}$$

The pressure $p_H(r,\theta)$ can be determined solving equation (5.14) using finite differences, as was explained in section 4.2.3. For the results obtained in Chapter Four it is expected that a portion of the fluid film will cavitate. As the total fluid manometric pressure is not allowed to take negative values, the cavitation condition can be expressed as

$$p_H(r,\theta) = -p_m(r,\theta) \tag{5.15}$$

Equation (5.15) implies that hydrodynamic and magnetic body forces are coupled inside the contact due to the fluid cavitation. In agreement with equation (5.13), to ensure that all the magnetic pressure on the fluid film is positive, the film must cover a radius such that, at the edge of the film, the magnetic field is lower than at any point inside of it. In agreement with the magnetic field distribution shown in Figure 5.5, this is achieved approximately for radius larger than 12 mm, it is 2 mm out from the inner surface (see Figure 5.4). Following this criteria, a volume of 20 μl was placed, centered at the contact. The hydrodynamic pressure $p_H(r,\theta)$ is expected to be generated only inside of the inner contact of radius *R=10 mm*. Then it can be assumed that

$$p_H(R,\theta) = 0 \tag{5.16}$$

5.4 Results

5.4.1 Load capacity vs. angular speed

The load capacity of the contact is shown in Figure 5.6 as function of the angular speed of the upper surface for a central film thickness $h_0 = 38\mu m$. It is expected that all the hydrodynamic lubrication occurs inside of the gap formed between the inner surface of the upper plate and the lower surface. Then the pressure in the part of the fluid film contained in the furrow can be considered of purely magnetic origin.

Experimental results and theoretical calculations are shown together. The load capacity predicted by Reynolds theory is larger than the measured value during the experiments carried out in the magnetorheological device. Despite the quantitative difference between the results from the theoretical model and the experiments,

functional similarities can be observed. In both cases, the load capacity remains constant for low values of the angular speed Ω. For larger values of Ω, the load capacity suffer a non-negligible increment, which is evidence of appearance of hydrodynamic forces in the fluid film. In the inset of Figure 5.6, the pressure distributions are shown for three values of angular speed: 0.6, 22 and 113 rad/s, when the maximum magnetic field strength was set to approximately 88.5 kA/m. For the lowest speed, the total pressure is due purely to the magnetic body forces on the fluid. Like the magnetic field distribution, the pressure distribution is symmetric in the radial coordinate. The hydrodynamic forces start to contribute to the total pressure in an asymmetric way with respect to the tilt axis as the angular speed increases, until cavitation appears, as shown in Figure 5.6 in the pressure distributions corresponding to 22 and 113 rad/s. Numerical simulations reveal that a load capacity increase occurs only when the maximum hydrodynamic pressure $p_H(r,\theta)$ overcomes the maximum of the magnetic pressure distribution since only then is cavitation achieved in the diverging wedge-like region of the geometry so that a noticeable increment in the load capacity is observed. The cavitation region reaches its maximum extension at the highest speed.
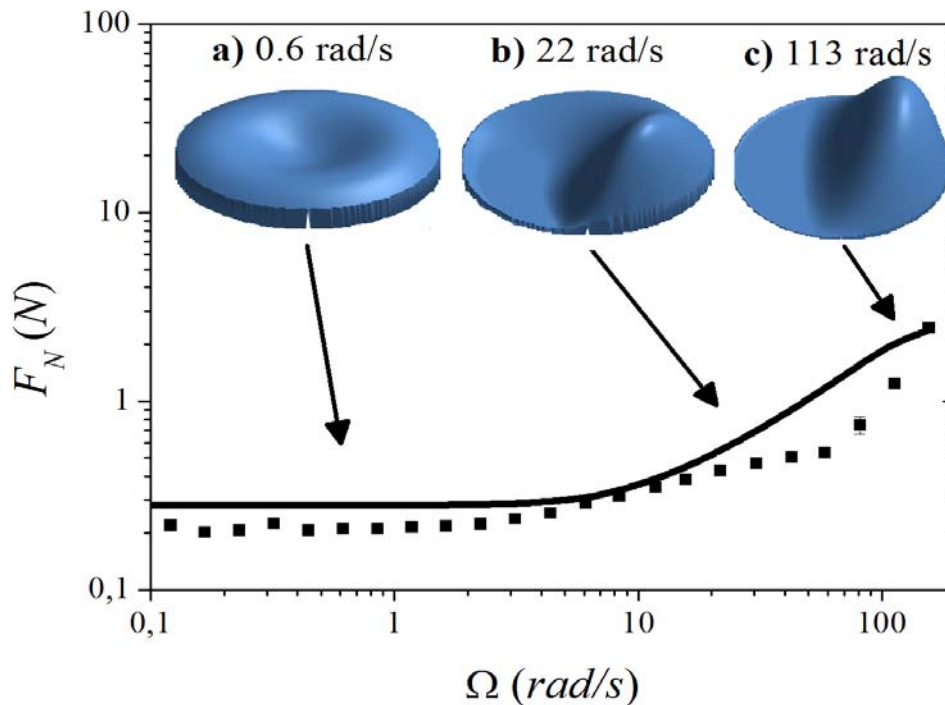
Figure 5.6 Load capacity in contact as function of the angular speed of the upper surface. Experimental and theoretical results are shown for a viscosity of 200 mPa·s and a magnetic field strength of 88.5 kA/m. Reynolds theory was solved assuming a central film thickness of 38 μm and $\varepsilon = 1.75$ μm.

5.4.2 Load capacity vs. fluid viscosity

Once we have probed that hydrodynamic forces may appear on the lubricant film of the magnetorheological geometry when the angular speed becomes large enough, we can investigate the influence of other lubrication parameters. We studied in Chapter 4 that hydrodynamic forces are proportional to the fluid viscosity, as mathematically expressed in equation (4.27). Here we will study the influence of the magnetic nanofluid viscosity in the presence of a magnetic field. Figure 5.7 shows the load capacity for three fluid viscosities 46, 200 and 560 mPa·s with a central film thickness $h_0 = 38 \, \mu m$.
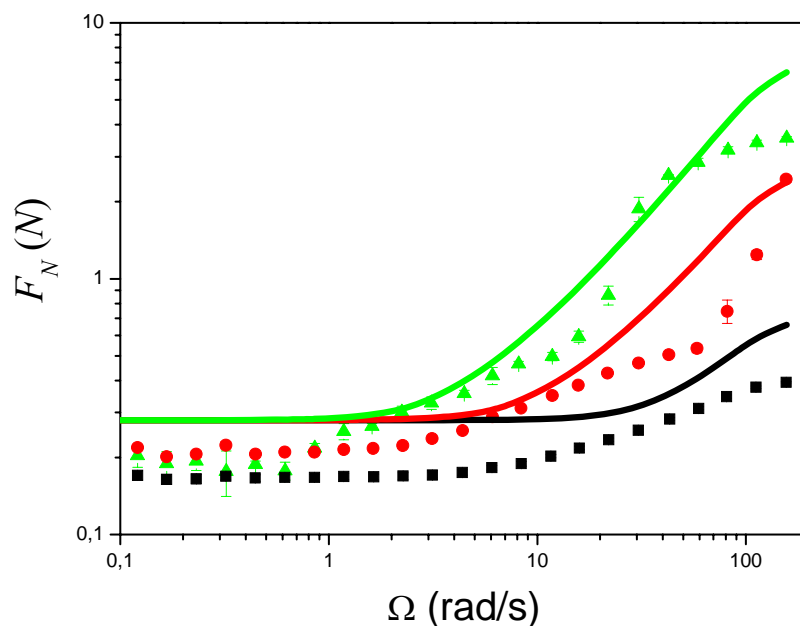
Figure 5.7. Load capacity for fluid viscosities of 46, 200 and 560 mPa·s and magnetic field of 88.5 kA/m. The solid lines are the theoretical calculations obtained from Reynolds theory, assuming a central film thickness of 38 μm and $\varepsilon = 1.75 \, \mu$m.

Again, it is observed that the load capacity remains constant at low angular speeds at a value independent of the fluid viscosity, as expected because in this range of speeds the total load capacity is provided by the magnetic body forces that depend only on the magnetic field strength and the magnetic properties of the fluid, which are very similar for all the fluid viscosities. The influence of the fluid viscosity can be appreciated as soon as the total load capacity starts to increase at larger speeds. The larger the fluid viscosity, the lower of the angular speed at which the load capacity starts increasing. Actually, in agreement to the Reynolds equation (5.14) hydrodynamic forces depend on

the product of the angular speed and the fluid viscosity. This can be observed in Figure 5.8, as the load capacity curves for different fluid viscosities collapse when they are plotted as function of the parameter $\eta\Omega$.
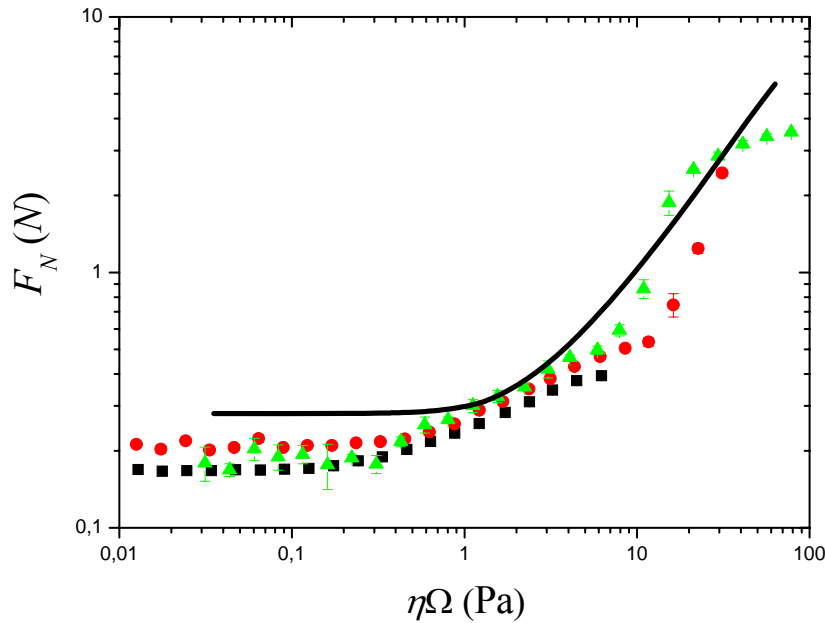
Figure 5.8. Load capacity as function of the parameter $\eta\Omega$ for fluid viscosities of (squares) 46, (circles) 200 and (triangles) 560 mPa·s and magnetic field with strength of 88.5 kA/m. The solid line is the theoretical calculation obtained from Reynolds theory, assuming a central film thickness of 38 μm and $\varepsilon = 1.75$ μm.

5.4.3 Load capacity vs. film thickness

The experimental equipment used in this work did not allow the surface misalignment represented by the parameter ε to be changed. This is not a real limitation in our study, since, in agreement with hydrodynamic lubrication theory, the influence of the film thickness on the hydrodynamic forces is represented by the ratio between the surface misalignment and the central film thickness $\varepsilon R/h_0$, as concluded in Chapter 4. Equation (4.28) shows that the strength of the hydrodynamic force acting on the contact increases with the value of the parameter $\varepsilon R/h_0$. The latter can be changed in both ways, either changing the plate misalignment ε or the central thickness of the fluid film h_0. The

experimental set-up used in this work does allow the latter to be modified. In figure 5.9, the load capacity is shown as a function of the angular speed for central film thicknesses of 38, 48, 58 and 68 mm, corresponding to values of $\varepsilon R/h_0$ =0.046, 0,036, 0.03 and 0.025, respectively. In this case, the contact was lubricated using a magnetic nanofluid with Newtonian viscosity of 560 mPa·s and the maximum magnetic field distribution of 88.5 kA/m was used. If the volume of magnetic nanofluid fluid inside is fixed, the area of the contact covered by the fluid decreases inversely proportionally with the central film thickness. In agreement with equation (5.13), the previously-described changes of area modify the contribution of the magnetic pressure to the total load capacity. To solve this problem, the load capacity shown in Figure 5.9 was normalized to value of the plateau obtained at low angular speeds. As previously discussed, in agreement with hydrodynamic lubrication theory, the hydrodynamic forces become stronger as the value of $\varepsilon R/h_0$ increases. This fact can be observed in two ways, in the lower speed needed to observe a contribution of hydrodynamic forces to the load capacity for larger values of $\varepsilon R/h_0$, and in the larger load capacities obtained for larger values of $\varepsilon R/h_0$.
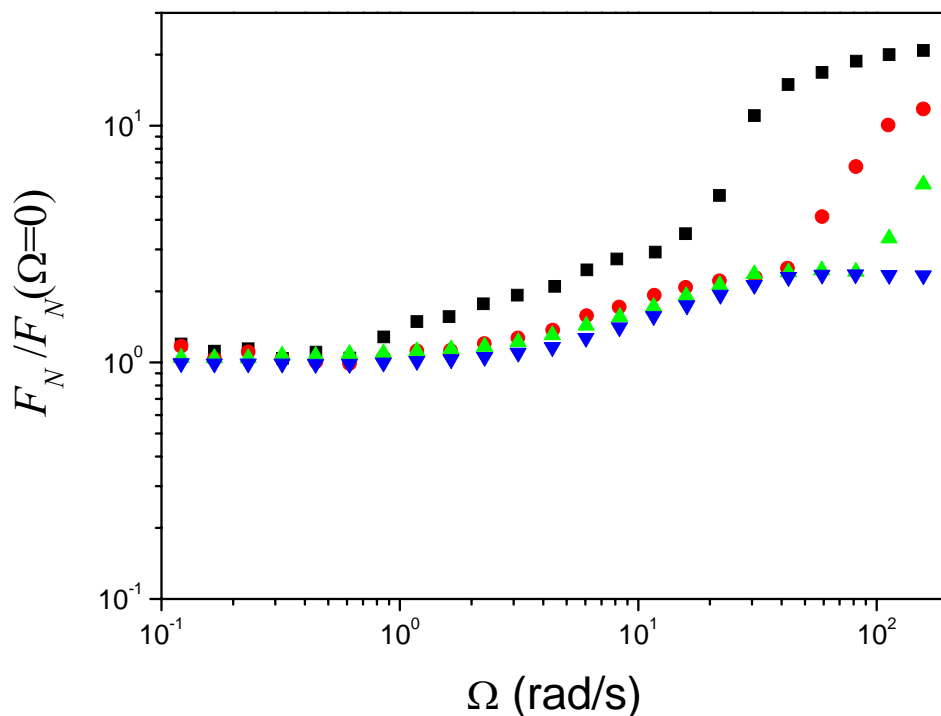

Figure 5.9. Load capacity normalized to its value in the initial plateau as function of the angular speed. The curves correspond to central film thickness of (squares) 38, (circles) 48, (up triangles) 58 and (down triangles) 68 μm.

5.4.4 Load capacity vs. field magnetic strength

The magnetic field strength is the externally controlled variable of interest in this work. It is expected to control the strength of the magnetic body forces on the fluid independent of the lubrication parameters, fluid viscosity, angular speed and separation between surfaces. The load capacity is shown as function of the angular speed for different magnetic field strengths in Figures 5.10, 5.11 and 5.12, for fluid viscosities of 46, 200 and 560 mPa·s. The load capacity for low speeds increases with the magnetic field strength equally for all the fluid viscosities. This fact is better observed in Figure 5.13, where this load capacity is shown as function of the magnetic field for the three fluid viscosities. The load increases linearly until the fluids approach the magnetic saturation and the rate of increase becomes lower.

As the magnetic body forces are enhanced by increasing the magnetic field strength inside the contact, the hydrodynamic pressure required to produce cavitation in the fluid film becomes larger. Thus, the presence of the hydrodynamic forces becomes non-negligible at higher speeds as the magnetic field strength is increased. This can be observed in the results for all the fluid viscosities studied in this work. The fluid viscosity enhances the hydrodynamic forces so that, for the same magnetic field strength, the increase in the load capacity is seen at lower values of angular speed for higher fluid viscosities. At high angular speeds the contribution of the magnetic field strength becomes less important so the curves for different values of magnetic field tend to converge. This is observed clearly in Figure 5.12, where hydrodynamic forces are stronger compared to the results shown in Figures 5.10 and 5.11, due to higher fluid viscosity. This fact is observed in both, theoretical and experimental results. The combined action of hydrodynamic and magnetic body forces is observed for intermediate angular speeds where an enhancement of the load capacity with the increment of the strength of the magnetic field is clear.
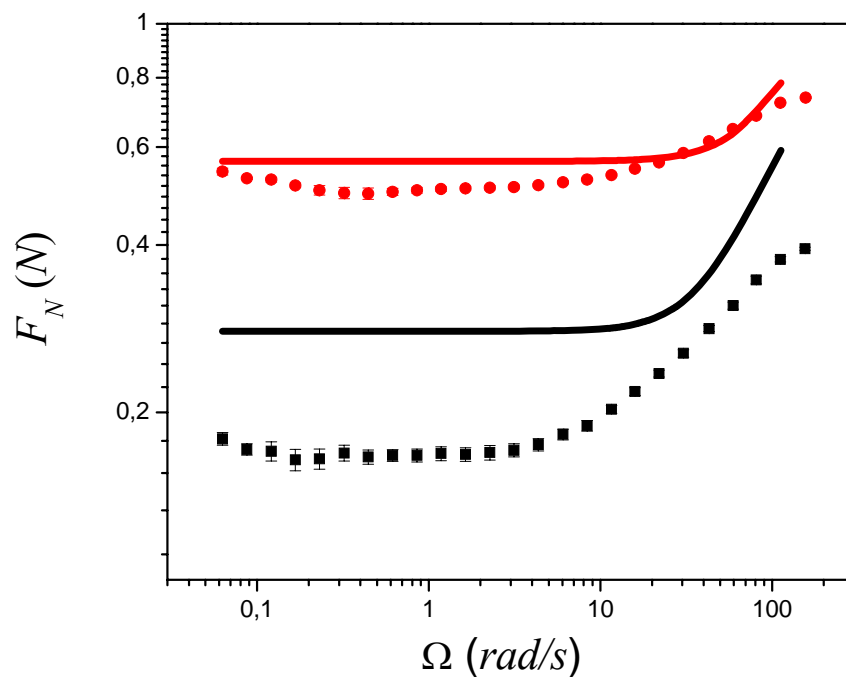
Figure 5.10. Load capacity of the contact lubricated with a magnetic nanofluid of 46 mPa·s of viscosity in the presence of magnetic fields of (squares) 88 and (circles) 177. The solid lines are the theoretical calculations obtained from Reynolds theory, assuming a central film thickness of 20 μm and ε = 1.75 μm.
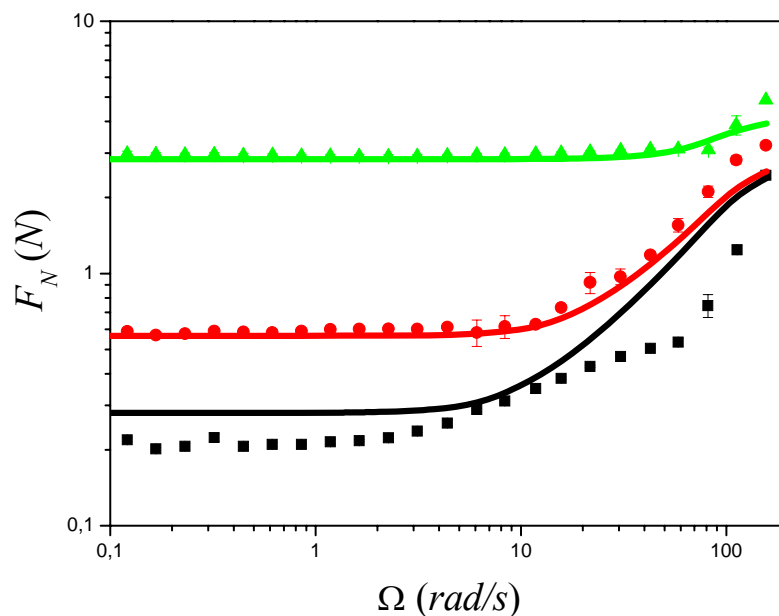
Figure 5.11. Load capacity of the contact lubricated with a magnetic nanofluid of 200 mPa·s of viscosity in the presence of magnetic fields of (squares) 88, (circles) 177 and (triangles) 885 kA/m. The solid lines are the theoretical calculations obtained from Reynolds theory, assuming a central film thickness of 20 μm and ε = 1.75 μm.
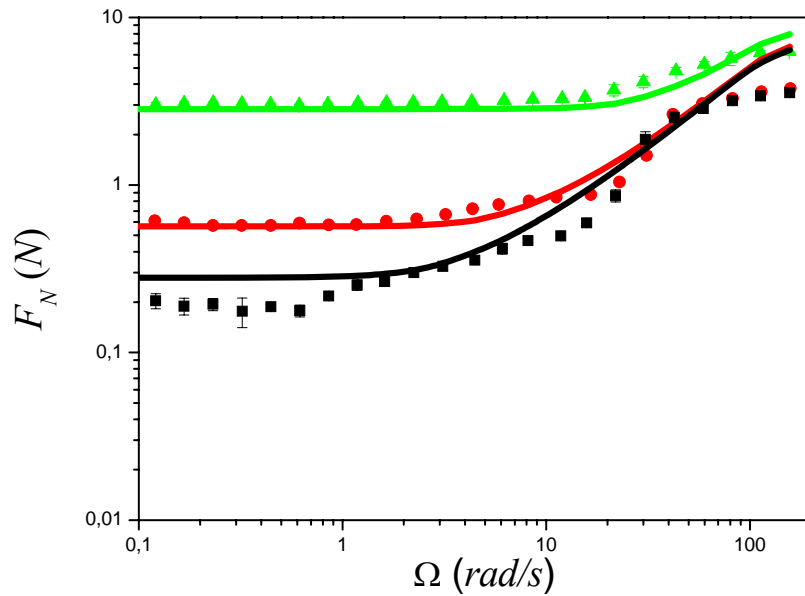
Figure 5.12. Load capacity of the contact lubricated with a magnetic nanofluid of 560 mPa·s of viscosity in the presence of magnetic fields of (squares) 88, (circles) 177 and (triangles) 885 kA/m. The solid Lines are the theoretical calculations obtained from Reynolds theory, assuming a central film thickness of 20 μm and $\varepsilon = 1.75$ μm.
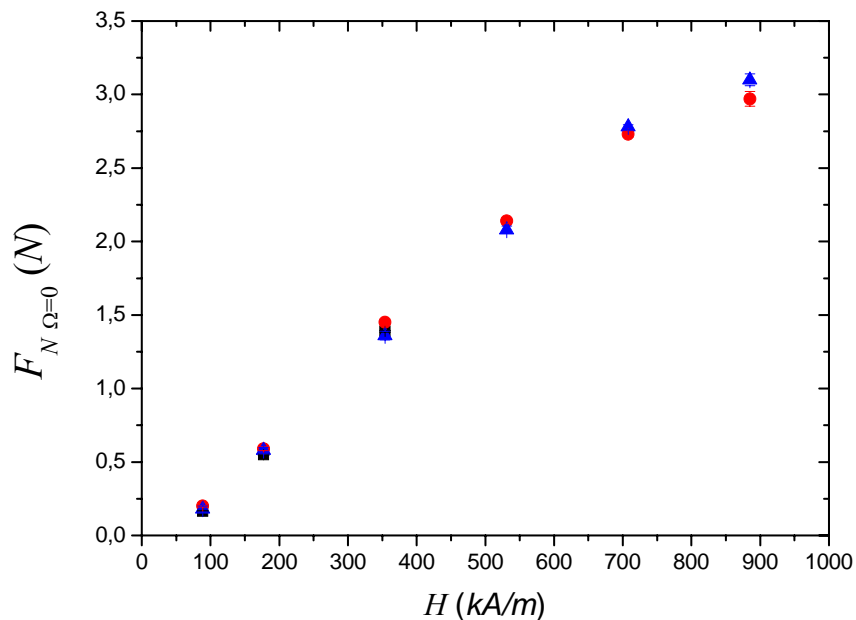
Figure 5.13. Load capacity provided entirely for the magnetic body forces on the fluid is represented here as function of the magnetic field strength for fluid viscosities of (squares) 46, 200 and 560 mPa·s.

Again, deviations are observed between values predicted from theory and values obtained in experiments. The agreement is the best at low angular speeds, where only the magnetic body forces provide the load capacity. Once the cavitated region in the fluid film has reached its maximum extension the theory predicts a log-log linear relation between the load capacity and the angular speed. This behavior is not shared by the experimental data, where a more complex behavior is observed. However, theoretical and experimental results agree in the fact that magnetic body forces improve the performance of the contact increasing its load capacity.

5.4.5 Control of friction in the contact

It this subsection, the effects of the magnetic body forces on the friction generated in the contact during operation is analyzed. Using the calculated and measured values of the torque on the upper plate, the friction coefficient on the contact was calculated using equation (4.34).

Firstly, the rheological behavior of the magnetic nanofluids used in this work in the presence of a magnetic field was explored using the results shown in Figure 5.14, where Stribeck-like curves are presented for different values of magnetic field strength and fluid viscosity. A variant of the Gumbel number defined in equation (4.32) is used here. We define a modified Gumbel number Gu^*, as

$$Gu^* = Gu\frac{R}{h_0} \tag{5.17}$$

From the definition of the friction coefficient (equation (4.34)), the Gumbel number and the torque measured in a parallel plates rheometer (equation (4.29)), we have

$$\mu = \frac{2T}{RF_N} = \frac{2}{RF_N}\frac{\pi}{2}\frac{\eta\Omega R^4}{h_0} = Gu* \tag{5.18}$$

In the geometry used for this work, the surfaces are not parallel and a small misalignment exists, such as for a central film thickness $h_0 = 38$ μm we have that $\varepsilon R/h_0$=0.046. In agreement with the results shown in Figure 4.3, the deviation expected

for the values of the Couette torque for misaligned and perfectly aligned surfaces is negligible for this value of the parameter $\varepsilon R/h_0$, hence equation (5.18) must hold. The latter is represented in Figure 5.14 as a dashed line. Nicely, it can be observed that the points obtained for the magnetic nanofluid in shear flow experiments fall close to this line, satisfying a Newtonian behavior for the range of magnetic field strength covered in this work.
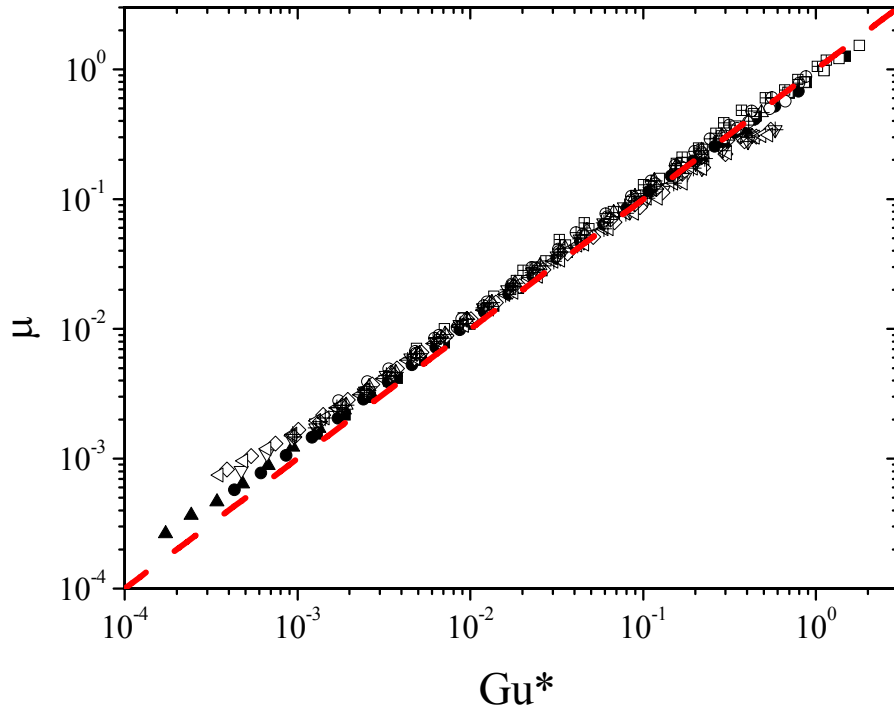
Figure 5.14. Experimental Stribeck curves where friction coefficient is shown as function of the modified Gumbel number. The experimental results correspond to three values of fluid viscosity; 46 mPa s (closed symbols), 200 mPa s (open symbols) and 560 mPa s (crossed symbols), for several magnetic field distributions; 88.5 kA/m (squares), 177 kA/m (circles), 354 kA/m (up triangles), 531 kA/m (down triangles), 708 kA/m (diamonds), and 885 kA/m (left triangles). Dashed line corresponds to predictions using classical rheology of Newtonian fluids under parallel plates ($\mu = Gu*$).

Secondly, it was shown theoretically in Chapter 4 that, for a contact lubricated with a simple Newtonian fluid and fixed film thickness, the friction on the contact depends solely on the product of the surface speed and the fluid viscosity (see equation (4.35)). However, in the case of magnetic nanofluids, a wide range of friction coefficients are allowed at a given $\eta\Omega$ value, depending on the applied magnetic field strength, as shown in Figure 5.15. As observed, friction can be reduced by one order of

magnitude by increasing the external magnetic field applied. Theoretical predictions and experimental results are not quantitatively in agreement, but both agree in the reduction of friction in the contact due to a magnetic field. Theoretical predictions obtained from Reynolds lubrication equation satisfactorily capture trends at low $\eta\Omega$ where, as shown in the previous subsection, the load capacity is mostly due to the magnetic forces in the fluid film. However, deviations between theory and experiment appear at large $\eta\Omega$ values, possibly due to the simple condition used to predict cavitation. Cavitation plays a very important role, because, as shown in Figure 5.5, the zone cavitated in agreement with Reynolds theory may occupy almost the half of the contact surface. Nevertheless, the results show that the friction of the contact can be externally controlled by the action of the magnetic field distribution when the contact is lubricated with a magnetic nanofluid.
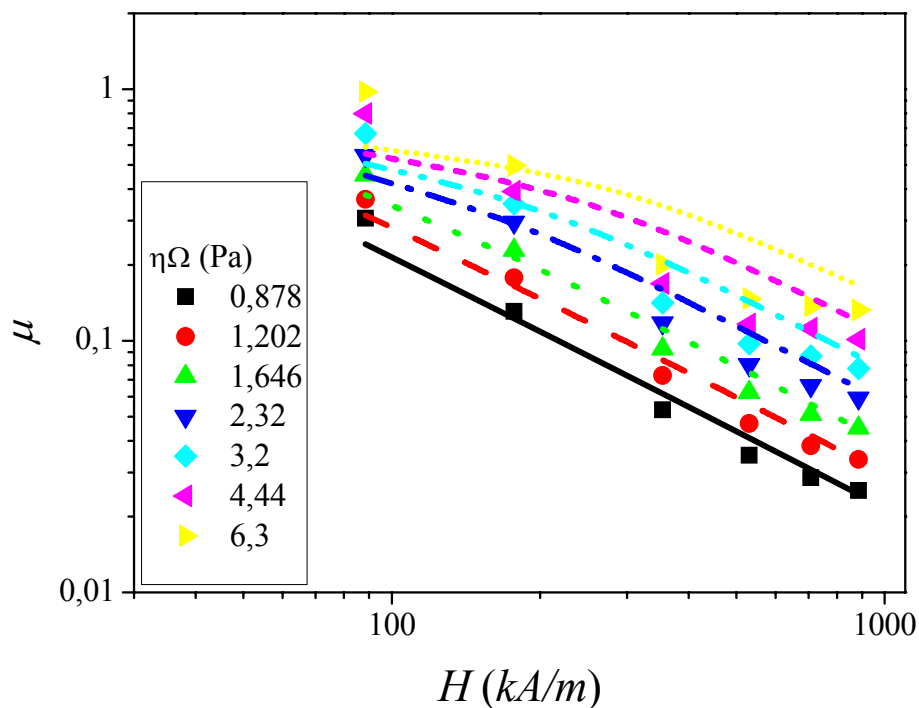
Figure. 5.15. Dependence of the friction coefficient, μ on the magnetic field strength H for $\eta\Omega$ = 0.878, 1.202, 1.646, 2.32, 3.2, 4.44, and 6.3 Pa. Lines represent theoretical predictions from full numerical solution of ferrohydrodynamic Reynolds equation. A good agreement with experimental results is found in the case of low $\eta\Omega$ values where cavitation is not present.

5.5 Chapter conclusion

The magnetorheological device used in this work behaved like a lubricated contact in which the small misalignment between the surfaces and the non-uniform magnetic field distribution applied inside it, produced, respectively, the appearance of hydrodynamic and magnetic body forces on the fluid film. On the one hand, hydrodynamic forces respond to the common lubrication parameters: relative surface speed, fluid viscosity and fluid film thickness. On the other hand, the magnetic forces respond to the magnetic properties of the fluid and to the strength of the applied field. In agreement with theoretical calculations, cavitation appears during operation of the contact, coupling the two kinds of forces. The load capacity as function of the parameter $\eta\Omega$ shows three different regions. At low values of $\eta\Omega$, where no cavitation takes place in fluid film, the strength of the magnetic body force determines the total load capacity of the contact. At intermediate values of $\eta\Omega$, cavitation appears in a portion of the fluid film and only then, the hydrodynamic forces become noticeable in the total load capacity. At high values of $\eta\Omega$, the contribution of the magnetic body force becomes negligible compared to the hydrodynamic force.

Experimental and theoretical results agree in the fact that tuning the strength of the applied magnetic field in the range covered in this work allows controlling the friction in the contact by at least in one order of magnitude.

Chapter 6: Control of starvation in a soft contact using magnetic nanofluids

This chapter examines the use of magnetic nanofluids to control starvation in lubricated contacts. Starvation in a ball-plate contact is experimentally studied under sliding-rolling conditions using a Mini Traction Machine (MTM). Friction is measured and the experimental results are presented in the form of Stribeck curves. The volume of lubricant is controlled in such a way that no free bulk oil is present in the vicinity of the contact. An abrupt change in the slope of the Stribeck curve in the Hydrodynamic Lubrication zone is interpreted as the onset of starvation. It is then shown that the use of magnetic nanofluids in the presence of a magnetic field distribution can change the conditions at which this onset of starvation occurs. Different magnetic field distributions are tested for different values of load and fluid viscosity. It is proposed that magnetic nanofluids in conjunction with a suitably-positioned magnetic field can be used to promote replenishment and thus control and reduce lubricant starvation.

6.1 Introduction

The surfaces of a contact working in the hydrodynamic lubrication regime are fully separated by a pressurized fluid film. Under flooded conditions, the Reynolds lubrication theory represents a powerful tool to predict the thickness and build-up pressure distribution of the film as function of the lubrication parameters, relative surfaces speed, fluid viscosity and load capacity. This way, many theoretical predictions have been developed for different contact geometries, including contacts composed of surfaces that suffer deformations due to the built-up pressure at the contact under normal conditions of operation. When the latter occurs and pressure is not high enough to provoke a change on lubricant viscosity at the contact inlet, the contact operates in the so called soft elasto-hydrodynamic lubrication regime.

A problem associated to contacts operating in this regime is the appearance of starvation. A contact goes from operating from flooded to starved conditions when the amount of free bulk lubricant in the inlet of the contact is not enough to build a lubricant film with the thickness expected under flooded conditions. Previous works have employed optical techniques to study starvation and thus to predict whether a contact is operating under flooded or starved conditions [Chiu, 1974; Guangteng, 1992; Jianhai, 1992; Cann, 2004; Yin, 2009]. Apart from this, it is also important to develop methods to improve the natural replenishment mechanism when the amount of oil needed to lubricate the contact is restricted, and hence prevent or limit starvation. The best way to do this is to find a method that allows some control *via* an external parameter, independent of other conventional lubrication parameters.

In this chapter, the frictional properties of a soft ball on plate contact were measured under restricted lubricant supply conditions. The use of magnetic nanofluids is proposed as a novel method to improve the replenishment of lubricant to the contact in the absence of free bulk lubricant [Andablo-Reyes, 2010-2].

6.2 Problem definition

In a point contact working in the soft elasto-hydrodynamic lubrication regime, the pressure in the lubricant film, starts to build-up at a distance x_B from the contact centre as illustrated in Figure 6.1. That position corresponds to the contact inlet. Commonly, when applying Reynolds lubrication theory it is supposed that the inlet distance is much larger than the radius of the solid-solid dry contact and the properties of the lubricant film is then independent of the inlet position. If this is satisfied, it is expected that the amount of lubricant around the contact will always sufficient to build the required lubricant film, and then the contact works under flooded conditions. Actually, experiments carried out in a ball-plate contact reveal that the minimum distance S_f between the inlet and dry contact radius a_H required to achieve a flooded condition is

$$S_f = \frac{3.52\left(Rh_{cf}\right)^{\frac{2}{3}}}{a_H^{\frac{1}{3}}} \tag{6.1}$$

where h_{cf} is the central film thickness under flooded conditions, R is the ball radius and

$$a_H = \left(\frac{1.31}{\pi}\right)^{\frac{1}{2}}\left(\frac{R'F_N}{E'}\right)^{\frac{1}{3}} \tag{6.2}$$

is the dry contact radius from Hertz theory. In equation (6.2), F_N is the contact load capacity, R' is the reduced radius in the entrainment direction and E' is the reduced elastic modulus. The latter are given by $1/R'=1/R_{x1}+1/R_{x2}$ and $2/E'=\left[\left(1-v_1^2\right)/E_1+\left(1-v_2^2\right)/E_2\right]$, where R_{x1}, R_{x2}, v_1, v_2, E_1 and E_2 represent the radii, the Poisson's ratios and Young moduli of the contacting bodies respectively. Theoretical calculations have been used to produce equations such as that given in equation (2.33) to predict the central film thickness h_{cf}. This quantity is found to depend on the operating conditions, load capacity, lubricant viscosity and the relative speed of the contacting surfaces.
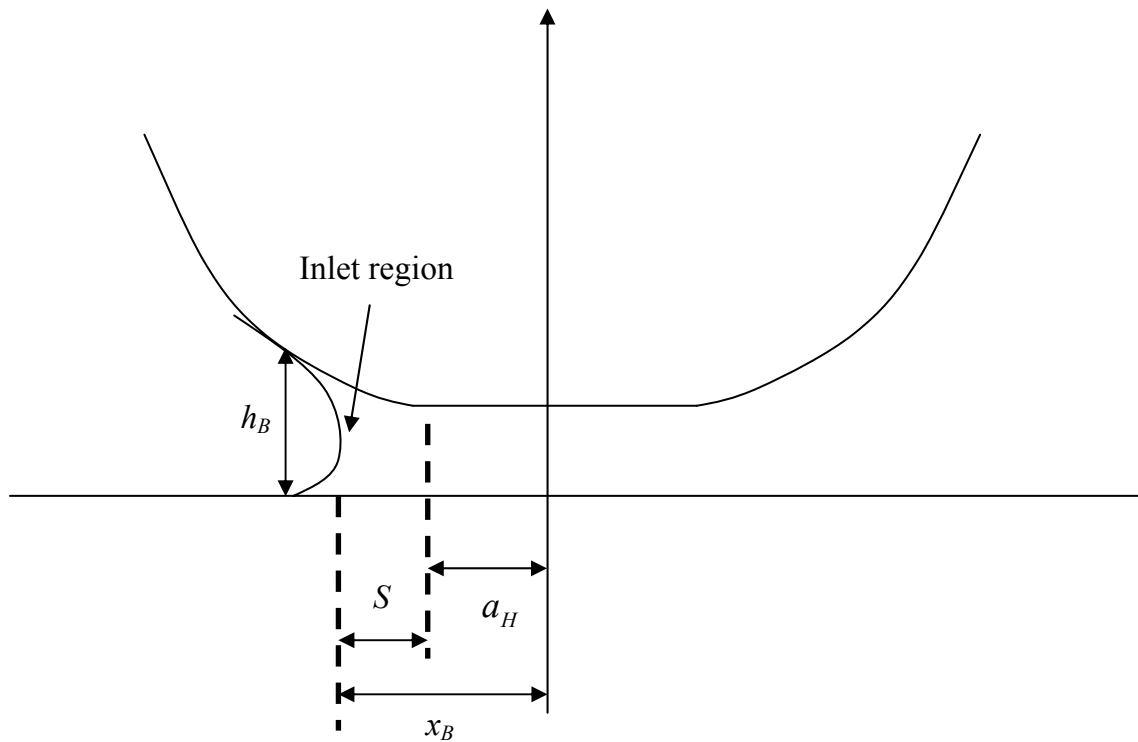
Figure 6.1. Schematic representation of a soft ball-plate contact. The contact inlet is placed a distant $S = x_B - a_H$ from the edge of the flat contact where x_B is the position of the inlet and a_H is the radius of the dry contact.

When the amount of lubricant around the contact is restricted, the condition mathematically expressed in equation (6.1) may not be satisfied and hence flooded hydrodynamic lubrication will not necessarily be achieved. In that case, the contact will operate in a regime known as starved elasto-hydrodynamic lubrication, where the functional dependence of the film thickness on the lubrication parameters is different and less than that expected for flooded conditions. Once the contact has started to operate in a starved soft elasto-hydrodynamic regime, the central film thickness h_{cs} depends on the height of the film h_B at the inlet position. Experimental evidence suggests that h_{cs} and h_{cf} are related, as shown in equation (6.3) [Cann, 2004].

$$\frac{h_{cs}}{h_{cf}} = \left(1.5\frac{h_b\sigma_s}{\eta U a_H}\right)^{1.67} \tag{6.3}$$

In equation (6.3) η is the fluid viscosity, U is the relative contact surfaces speed, a_H is the dry Hertz contact and σ_s is the fluid-air surface tension. The latter plays an important role in the replenishment mechanism of oil expelled to the sides of the contact and returned to the contact inlet. The higher lubricant-air surface tension, the larger amount of oil returned to the contact inlet. As soon as the contact operates under starved conditions the thickness of the lubricant film decreases respect to its value of flooded conditions as the factor ηU increases. The last mentioned is basically the problem of starvation, and results in the friction in the contact becoming larger than the value expected under flooded conditions.

Despite efforts to develop empirical and theoretical models to predict whether a rolling-sliding contact is operating under flooded or starved conditions, no mechanisms have been proposed to stop or reduce the degree of starvation apart from supplying oil directly to the contact. In the present study, the use of magnetic nanofluids as lubricants in the presence of a non-uniform magnetic field is proposed as a route for starvation reduction. Theoretical studies suggest that, under the proper conditions, magnetic fluids improve the contact load capacity and help preventing leakage at high operating speed or under the action of gravity [Chandra, 1993; Shah, 2004; Bali, 2005]. A successful application of this kind of fluid is the so-called magnetic seal, where the fluid is used to separate two plates that are maintained at different operating pressures [Rosenweig, 1997; Chandra, 1993; Shah, 2004; Bali, 2005; Ravaud, 2010]. In this, the fluid is externally manipulated by the application of a magnetic field distribution and confined in a desired position. The same mechanism can also be applied, in principle, to feed lubricant back into the contact using external forces when no free bulk oil is available.

Commonly, magnetic nanofluids are opaque media and, as a consequence, optical techniques cannot be used to determine the film thickness of lubricant in the contact. An indirect method to obtain information of the performance of this replenishment mechanism consists of measuring the friction force in the contact under different running conditions. This way, the performance of the lubricating forces (magnetic and hydrodynamic) is evaluated under different operation conditions of magnetic field strength and distribution, fluid viscosity, entrainment speed and applied load.

6.3 Experimental method

In this work, friction measurements were carried out using a Mini Traction Machine (MTM), which was adapted to study lubrication using magnetic fluids. In this apparatus, a ball is loaded and rotated against a flat surface of a rotating disc in the presence of a lubricant. The motion of both parts can be controlled independently to achieve any desired sliding-rolling speed combination and the ball shaft is inclined to minimize spin in the contact. Friction is measured by a load cell attached to the ball motor and, in the MTM, is determined by taking a pair of measurements at the same slide-roll ratio but with the ball moving respectively faster and slower than the disc. These two values are then differenced to eliminate any zero load offset in the load cell.

The contact studied was that of a PDMS elastomer ball (Sylgard^{TM} 184, supplied by Dow Corning) against an aluminium disc. A mould having a spherical cavity of 19 mm diameter was used to fabricate the elastic balls. The Sylgard components were mixed, degassed in a vacuum chamber, placed inside the mould and cured at a temperature of 60 ºC for a period of one hour in an oven. From this, bubble-free, elastomer spheres with a non-deformed radius of 19 mm and Young modulus of 3 MPa were prepared. The MTM aluminium disc had Young's modulus 69 GPa. The Poisson's ratio of the elastomer and aluminium were taken as 0.3 and 0.5 respectively, so the reduced elastic modulus was 8 MPa.

All the tests were carried out at room temperature at a slide-roll ratio $SRR = 0.50$. Friction was measured over an entrainment speed range of $U = 0.005$ to 1 m/s, at applied loads of $W = 3$, 5 and 7 N.

A radially-symmetric magnetic field distribution centered at the point contact was achieved by placing circular permanent magnets under the aluminium disc. The strength and shape of the distribution was easily changed by varying the number of magnets in the arrangement, as shown in Figure 6.2. The diameter of the magnets was 6 mm, which fully covers the largest Hertz contact radius, which has a value of 1.3 mm at a load of 7 N. The magnetic field distributions corresponding to the different magnet configurations are labeled as "maximum", "medium" and "minimum". The magnetic field density reached at the centre of the contact was 150, 50 and 25 mT respectively. Magnetic nanofluids used here were provided by FerroTec, Co. and all have the same $M(H)$ superparamagnetic Langevin type dependence (saturation magnetization 24.3 $\pm$

0.7 kA/m), but different Newtonian viscosities of 46, 200 and 560 mPa·s. The carrier fluids are synthetic ester and synthetic hydrocarbon, for the first and the last two magnetic nanofluids respectively. Also, density and surface tension is approximately the same for all the fluids. With the last, we ensure that the natural replenishment mechanism is independent of the fluid viscosity. Considering a particle size log-normal distribution and using the Langevin function, a value of 9 nm was obtained for the average particle diameter, with a polydispersity around of 20 % [Chantrell, 1978]. Particle volume fraction is around 5.5 vol % for the three lubricants, assuming a saturation magnetization for bulk magnetite of 447 kA/m. A rheological characterization of the magnetic nanofluids was performed. Neither shear-thinning nor viscoelasticity were observed in the range of shear rates of interest. The fluid characterization has been previously explained in section 5.2.

For every test, one drop of 500 μL of ferrofluid was deposited in the vicinity of the contact at rest conditions. As soon as the oil was placed around the contact it was trapped by the magnetic field. The amount of oil is then restricted to the oil trapped by the magnetic field.
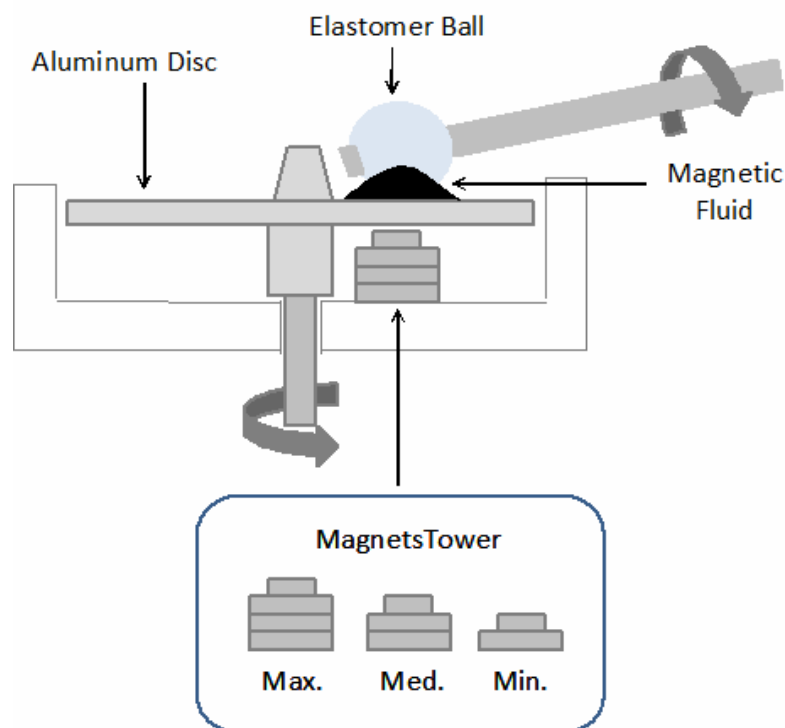

Figure 6.2. Schematic representation of the adapted Mini Traction Machine. The three magnet set-ups are represented.

6.4. Results

In both fully flooded and starved conditions, entrainment speed U, fluid viscosity η, and load capacity W control the contact friction. Therefore each of these parameters will be studied, introducing at the same time the magnetic field as a controllable external parameter.

6.4.1 Role of the entrainment speed on the starvation

The scaling number $U\eta$ determines the film thickness and thus the regime in which the contact operates. Initially the fluid viscosity was held constant and the effect of speed on lubrication studied. Figure 6.3 shows the friction coefficient *versus* the entrainment speed U, for a viscosity of 200 mPa·s, a load of 7 N and the maximum magnetic field distribution. Mixed and hydrodynamic lubrication regions are shown in the range of entrainment speed swept in the figure.

Despite the limitation in lubricant supply, this curve shows similar behaviour of a contact under fully flooded conditions for entrainment speeds up to approximately 0.6 m/s. The log-log slope in the hydrodynamic regime is 0.4 ± 0.07. This value is similar to the value of 0.33, calculated by considering a simple Couette flow, and assuming that the fully flooded film thickness is proportional to $U^{0.67}$ [de Vicente, 2005]. Moreover, this result is different from that obtained by solving Reynolds equation under the assumption of fully flooded condition given in equation (2.34), as shown in Figure 6.3 in which this model is represented as a solid line. The slope predicted by the model is clearly larger than the slope of the experimental data. However, the experimental and theoretical values for the friction coefficient μ are similar until a dramatic change in the slope of the experimental curve occurs. This change occurs when the speed becomes larger than 0.6 m/s (pointed out by a vertical dashed line in Figure 6.3); this is believed to be the critical point that divides full lubrication and starved lubrication and to result from the lack of lubricant to achieve the fully flooded film thickness.

In agreement to equation (6.3), the oil film thickness is found to be proportional to $U^{1.67}$ when the contact operates under starved conditions. If the same assumption of a simple Couette flow is taken, the resulting friction coefficient is proportional to U^2. However, the slope found for these measurements is larger, at about 5.9. In addition to

the previous mechanisms proposed for rolling contacts, in rolling-sliding conditions both the disc and the ball are in motion. Due to the movement of the disc, centrifugal forces act on the lubricant, whose magnitude depends on the disc speed and the position of the contact respect to the spinning centre and also on the fluid density. This force is neglected by Reynolds theory, under the assumption of fully flooded conditions. However, when the amounts of oil are restricted and entrainment speed is large enough they play an important role pulling the lubricant out from the Hertz contact to the rim of the plate, hindering the replenishment mechanism and increasing the starvation.
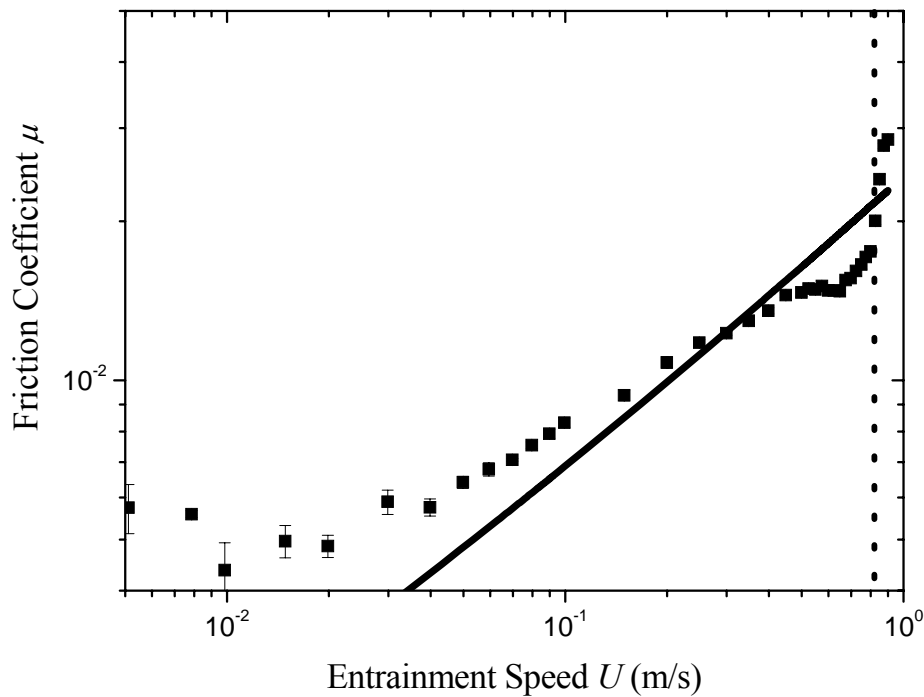
Figure 6.3. Friction coefficient μ as function of the entrainment speed U for a 200 mPa·s magnetic nanofluid. Mixed and hydrodynamic lubrication regions are shown. The load is 7 N and the maximum magnetic field distribution is applied. A dotted line divides the fully and the starved hydrodynamic lubrication regimes. The solid line corresponds to the model obtained by solving Reynolds equation under the assumption of fully flooded conditions.

6.4.2 Role of the fluid viscosity on the starvation

The viscosity is another important parameter governing the performance of the lubricant in the contact. Results for fluid viscosities of $\eta = 46$, 200 and 560 mPa·s are shown in Figure 6.4. As expected from hydrodynamic lubrication theory, the higher the viscosity, the larger the friction coefficient. The critical point between fully flooded and starved lubrication is reached at lower speeds for the higher viscosity, as shown by the division lines inserted in the figure. This is in agreement with observations obtained from film thickness measurements by other authors, where it was found that the fluid film starvation increases with fluid viscosity [Chiu, 1974; Guangteng, 1992; Jianhai, 1992; Cann, 2004]. Figure 6.5 shows the friction coefficient plotted as function of the product of the entrainment speed and the fluid viscosity $U\eta$. All the curves collapse to a single one in the fully lubricated regime. However, the same effect is not observed in the starved lubrication regime since for different fluid viscosities, the critical point occurs at a different value of the parameter $U\eta$.
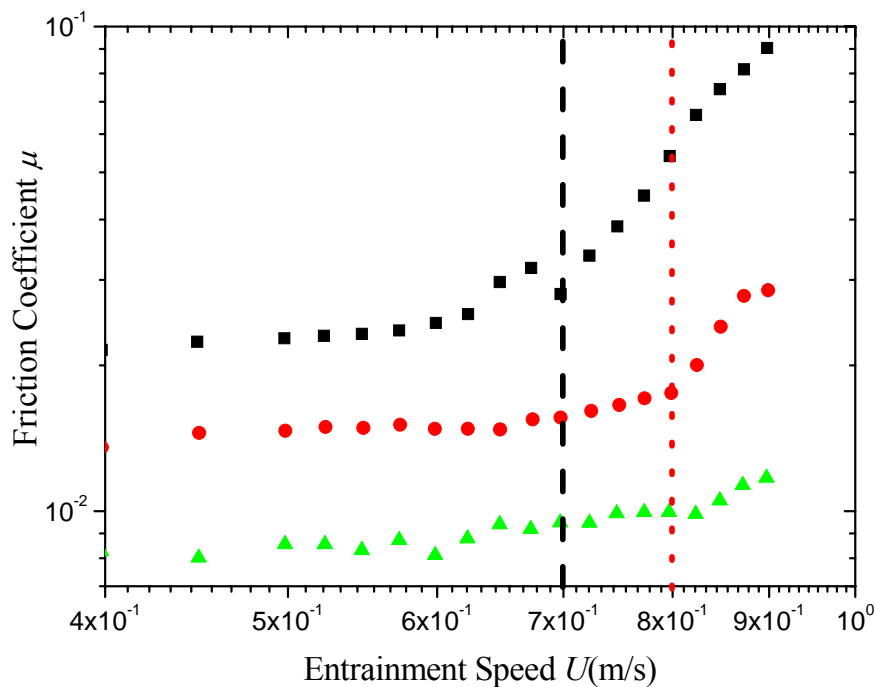
Figure 6.4. Friction coefficient μ as function of the entrainment speed U for three magnetic nanofluid viscosities (triangles) 46, (circles) 200 and (squares) 560 mPa·s in the presence of the maximum field strength and a 7 N applied load. The transition between the fully flooded and the starved lubrication regime was observed for 200 mPa·s (dotted line) and 560 mPa·s (dashed line). Contrarily, starvation was not observed for the lowest viscosity ferrofluid investigated.
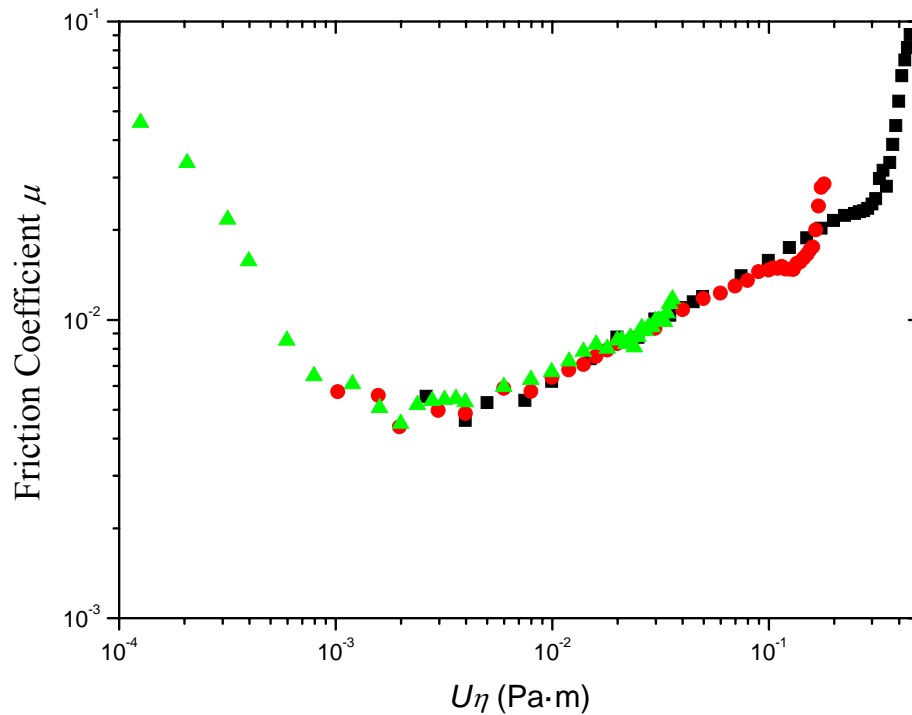
Figure 6.5. Friction coefficient μ vs. the parameter $U\eta$ for (squares) 46, (circles) 200 and (triangles) 560 mPa·s magnetic nanofluids in the presence of the maximum magnetic field at 7 N load.

6.4.3 Role of the load capacity on the starvation

Figure 5 shows the friction coefficient as function of the entrainment speed for a 200 mPa·s fluid. Loads of 3, 5 and 7 N were tested at the maximum magnetic field distribution. Similarly to the case of fully flooded conditions (see equation (2.34)), here the friction coefficient decreases with the applied load. For all the loads investigated, the transition point occurs at $U = 0.8$ m/s, which is observed as an increment of the slope of the curves of friction coefficient. A dashed line is used to separate the fully flooded and starved lubrication regimes. The values of the slopes after the transition do not differ significantly for different values of W. Hence, the applied load has no significant influence on the performance in this starved regime.
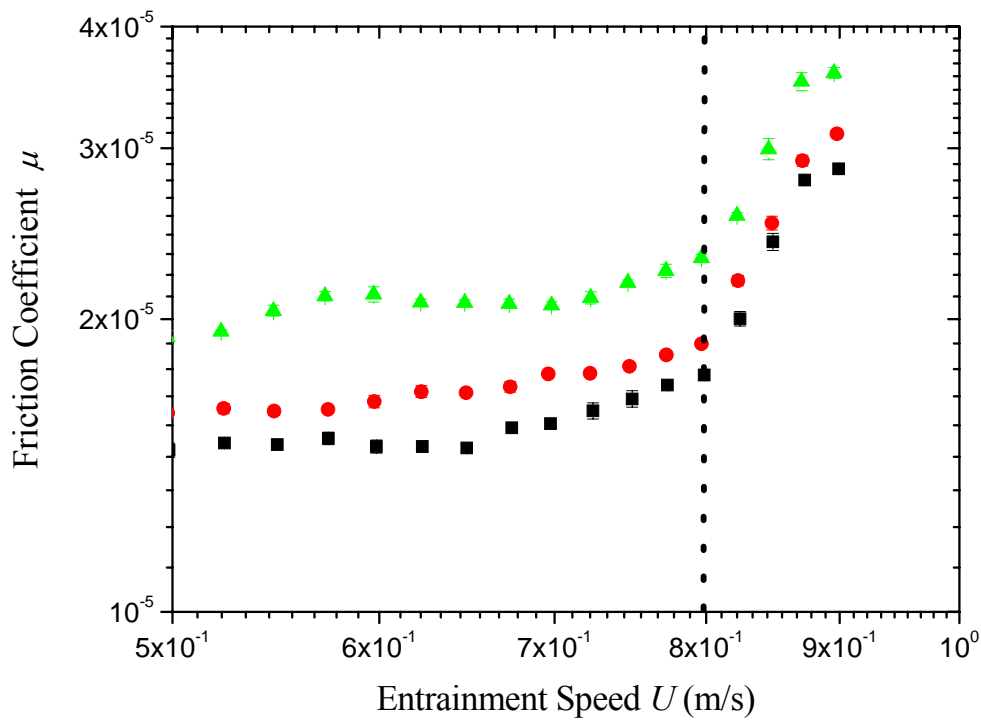
Figure 6.6. 200 mPa·s magnetic nanofluid at three different loads (triangles) 3, (circles) 5 and (squares) 7 N, in the presence of the maximum magnetic field. The dotted line corresponds to the transition point between the fully to the starved lubrication regime. The transition occurs at the same speed for all the curves.

6.4.4 Role of magnetic field distribution on the starvation

Once the role of the lubrication parameters (U, η and F_N) in controlling the occurrence and development of starvation in the contact has been established, it is important to study the influence of the parameter proposed here to control starvation, the magnetic field.

The lubricants were chosen so that, regardless the fluid viscosity, the magnetic response was approximately the same. This means that the magnetic lubrication forces are completely controlled by the strength and shape of the external magnetic field distribution, with no variation due to mechanical properties (*e.g.* density, surface tension).

Magnetic body forces appear in the magnetic fluid when a magnetic field distribution is applied and are given by $-\mu_0 M(H)H$, where μ_0 is the vacuum permeability, $M(H)$ the functional fluid magnetization and H the magnetic field strength. Thus these forces depend on the magnetic response of the fluid and the shape and strength of the magnetic field distribution. Due to magnetic forces, the pressure on the fluid is increased, and the main effect of this is the confinement of the fluid around the region of maximum field, i.e. in this case around the centre of the contact. All the results shown in the previous subsections were carried out at the maximum field distribution. The effect of decreasing the strength of the magnetic field is now explored.

In Figure 6.7, Stribeck curves for a fluid viscosity of 46 mPa·s are shown for the three different magnetic field distributions used in this work. As shown above, the load applied did not significantly affect the transition from fully flooded to starved elasto-hydrodynamic lubrication regime. So a value of 7 N was fixed. As observed in Figure 6.7, there was not any significant difference between applying the minimum and medium magnetic field distribution. However, when the maximum magnetic field was applied, the contact remained working in the fully lubricated regime over the range of speeds studied in this work, which means that starvation was prevented by increasing the magnetic field. The same experimental tests are shown in Figure 6.8, now for a much more viscous ferrofluid. In this case, the transition point between tribological regimes is clearly shifted to higher speeds for higher values of magnetic field strength. In highly viscous magnetic nanofluids, starvation was not fully prevented even for the highest magnetic fields employed, in contrast to low viscosity magnetic nanofluids (see Figure 6.7). Summing up, higher viscosities and higher speeds require higher magnetic fields to prevent starvation. It is demonstrated here that the external magnetic field can be used as a lubricant supply control parameter, which can be tuned independently, without interfering with the rest of the lubrication parameters.
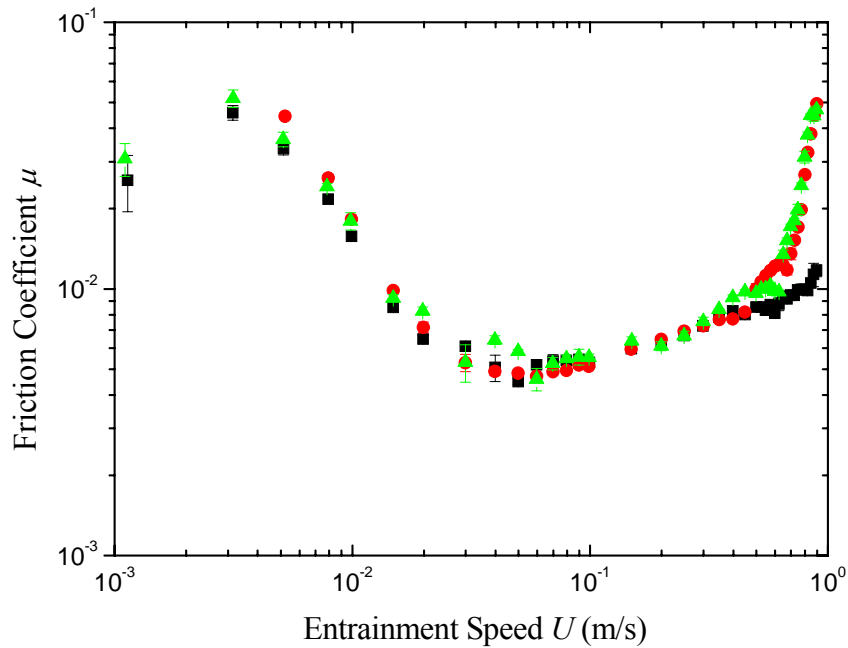
Figure 6.7. Stribeck curve for three different magnetic field distributions (triangles) Low, (circles) Medium and (squares) Maximum. The viscosity is 46 mPa·s and the applied load is fixed at 7 N.
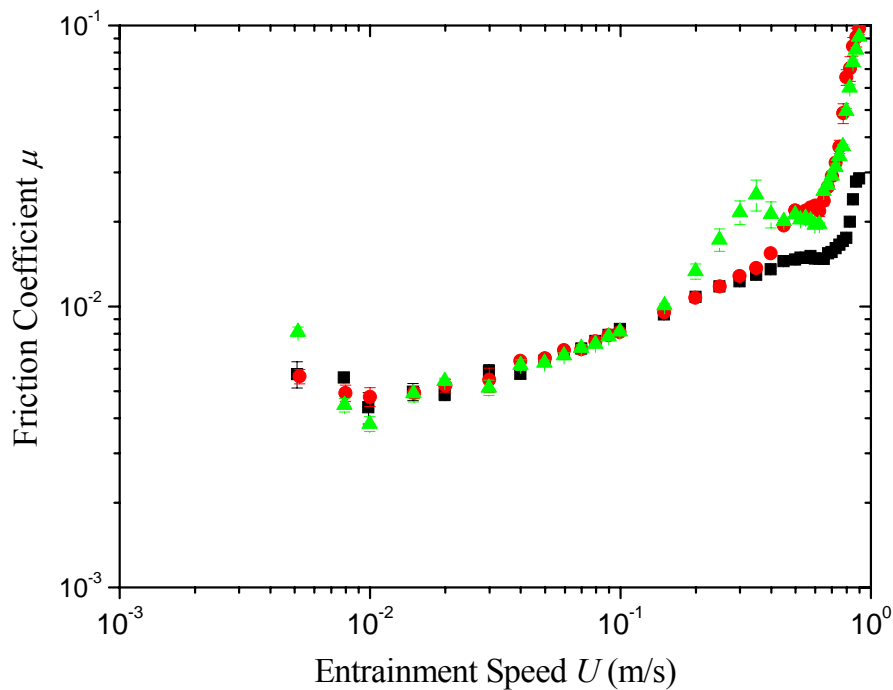
Figure 6.8. Stribeck curve for three different magnetic field distributions (triangles) Low, (circles) Medium and (squares) Maximum. The viscosity is 200 mPa·s and the applied load is fixed at 7 N.

6.5 Chapter conclusions

Starvation is a problem in many lubricated systems. It occurs at high speeds and with high viscosity lubricants and is thus a problem in rolling element bearings operating at low temperatures. It is especially prevalent with low elastic modulus, polymeric bearings where the contact is large and wetting of the surfaces by the lubricant often poor.

The experimental results show that magnetic nanofluids can be used as smart lubricants to limit starvation in sliding-rolling contacts where the amount of lubricant is restricted. A non-uniform magnetic field distribution is centered on a sliding, non-conforming contact lubricated with magnetic nanofluid. This has the effect of confining the fluid within the region of the contact, thus greatly reducing the total amount of lubricant required. Experiments show that the transition between the fully and starved lubrication regimes can be controlled by modifying the magnetic field distribution.

The transition between hydrodynamic and starved regimes depends on the fluid viscosity and not on the applied load, at least in the range covered in the present study. The higher the viscosity, the lower the speed associated to the onset of starvation. Hence, it is shown that the higher the viscosity, the higher the magnetic field strength required to prevent starvation.

As well as helping to control starvation, it is likely that the ability to confine a magnetic nanofluid lubricant close to the location where lubrication is required using a magnetic fluids might also be desirable in situations where viscous drag losses need to be minimized. For example the application of magnetic fields to transmissions could potentially offer increased efficiency by reducing the volume of lubricant in which contacting surfaces are submerged. As shown in this work, if an appropriate magnetic field distribution is applied, very small lubricant volumes can be employed without the normally-associated risk of starvation.

Chapter 7: Summary and conclusions

The aim of this work was to study the performance of magnetic nanofluids as lubricants in contacts operating in the hydrodynamic and soft elasto-hydrodynamic lubrication regimes. The results of this study have been divided in three chapters. Here we present a brief summary of all them and their most important conclusions.

7.1 Hydrodynamic lubrication forces in a contact of two tilted rigid surfaces

Using the Reynolds lubrication theory we studied the theoretical performance of a lubricated contact operating in the hydrodynamic lubrication regime. This contact consisted of two tilted flat circular rigid surfaces, separated by a thin film of a Newtonian fluid. One of the surfaces was made to rotate while the other was kept fixed, transmitting a torsional shearing force on the fluid film under the assumption of no slip at the surfaces. The shearing force resulted in the fluid passing periodically from a converging wedge-like zone to a diverging one in circular laminar flow inside the contact. This mechanism produced hydrodynamic forces that pressurized the fluid film. The pressure film increased in the convergent zone while in the divergent one, it decreased until cavitation was induced. The area of the cavitated region depended on the operating conditions of the contact.

A set of reduced variables were introduced to facilitate the solution of the lubrication equation, which was solved numerically using a method of finite differences. The load capacity provided by the fluid film pressure showed a direct proportional relation with the product of the fluid viscosity and the angular speed of the rotating surface. It also increased with the surfaces misalignment and it was reciprocal to the central film thickness. Regression equation to describe the dependence of the load capacity and friction on the operation conditions of the contact were developed using the results for the normalized variables. Using these equations, the compromise between all the lubrication and geometrical parameters of the contact was summarized in a Stribeck curve representation. This curve depends only on the parameter describing the relative tilt of the contact surfaces. The theoretical Stribeck curve obtained here were in good agreement with experimental results available in literature for a similar contact.

Besides the interest of this problem in lubrication, it has also interest in rheometry. The equations developed here may be used to determine the central film thickness and misalignment between the surfaces of a plate-plate rheometer, provided that the rest of the lubrication parameters are known or measured.

7.2 Hydrodynamic lubrication in a contact of tilted rotating surfaces

A magnetorheological plate-plate rheometer was used to study the performance of a contact lubricated with a magnetic nanofluid. This geometry corresponds to rotating contact between two slightly tilted surfaces described in the previous section. Thus, in agreement to the theoretical results hydrodynamic forces appeared in the fluid due to the periodically passage of the fluid through converging and diverging wedge-like zones formed by the tilted surfaces. In addition, magnetic body forces were introduced in the fluid film due to a non-uniform magnetic field distribution applied inside the contact.

In addition to experimental results, a theoretical description of the problem was carried out by solving the modified Reynolds theory for magnetic nanofluids.

If the load capacity is represented as function of the product of the fluid viscosity and the angular speed $\eta\Omega$, the former can be located in one of three different regions depending on the balance of magnetic and hydrodynamic forces in the fluid film, which were determined, respectively, for the magnetic parameters and the value of $\eta\Omega$.

In the first region, at low values of the product $\eta\Omega$, the load capacity depends only on the strength of the magnetic body forces on the fluid. In agreement with theoretical calculations, in this region, a plateau in the load capacity curve can be observed. In this region, the pressure due to the hydrodynamic force is lower than the pressure resulting from the magnetic ones and cavitation is not achieved. The larger the magnetic field, the wider the range of $\eta\Omega$ where the plateau is observed. Once a portion of the fluid film had cavitated, an increment in the load capacity was observed. In this region the total load capacity depends on the strength of both hydrodynamic and magnetic forces on the fluid.

Finally, for low or intermediate values of the magnetic field strength and high values of the product $\eta\Omega$, hydrodynamic forces dominate over the magnetic ones, and the total load capacity becomes independent of the value of the strength of the applied magnetic field.

Theoretical and experimental results agree in the fact that the improvement in the total load capacity in the contact due to the magnetic body forces appearing in the fluid helps decrease the friction in the contact, which can be controlled by in at least one order of magnitude, in agreement with the results shown in this work.

7.3 Control of starvation in a soft contact using magnetic nanofluids

A contact works in the soft elasto-hydrodynamic lubrication when the pressure in the fluid film separating completely its surfaces is high enough to deform at least one of the contact surfaces but not to cause changes in the fluid viscosity at the inlet of the contact. This regime of lubrication was studied experimentally in a contact composed of a soft elastomeric ball loaded and rotated against a flat surface of a rigid rotating disc in the presence of a limited amount of a magnetic nanofluid. A set of circular magnets arranged in a tower like structure was placed under the disc, centered with the contact. This induced a non-uniform magnetic field radial dependent distribution which confined the fluid around the contact.

Due to the small amount of lubricant at the contact, starvation occurred in the contact at high speeds. This was observed in an abrupt change of the slope in the curves where the friction was represented as function of the relative surfaces speed. The friction coefficient increases more rapidly in a starved regime than in a fully flooded one. The starvation occurs because the rupture of the natural replenishment mechanism of lubricant to the inlet contact.

In agreement with the observed the higher the viscosity, the lower the speed associated to the onset of starvation. The load capacity of the contact had no significant influence on this.

Experiments showed that the transition between the fully and starved lubrication regimes can be controlled by modifying the magnetic field distribution. The magnetic forces appear to act like an extra lubricant replenishment mechanism, externally manipulated by the applied magnetic field. The higher the viscosity, the higher the magnetic field strength required to prevent starvation.

Capítulo 8: Resumen y conclusiones

El objetivo de este trabajo fue estudiar el comportamiento de un fluido magnético empleado como lubricante en contactos que operan en los regímenes conocidos como lubricación hidrodinámica y lubricación elasto-hidrodinámica suave. Los resultados de este estudió fueron divididos en tres capítulos a lo largo de este manuscrito. Aquí se presenta un breve resumen de todos ellos, así como las conclusiones más importantes.

8.1 Fuerzas de lubricación hidrodinámica entre dos superficies inclinadas

Empleando la teoría de lubricación de Reynolds se estudió el funcionamiento de un contacto lubricado operando en el régimen de lubricación hidrodinámica. Dicho contacto estaba compuesto por dos superficies circulares, planas, relativamente inclinadas y separadas por una fina capa de un fluido Newtoniano. Al hacer rotar una de las superficies manteniendo la otra fija, el fluido era forzado a fluir periódicamente dentro del contacto, pasando de una primera zona en la cual la distancia entre superficies disminuía a una segunda donde las superficies se separaban. Se encontró que este mecanismo era capaz de generar la aparición de fuerzas de lubricación hidrodinámica, presurizando así la capa de fluido. En la primera zona se producía un aumento de presión, mientras que en la segunda la presión disminuía hasta provocar la aparición de cavitación en el fluido.

Para facilitar la resolución de la ecuación de Reynolds se introdujo una serie de variables normalizadas. Dicha resolución se llevó a cabo mediante la utilización de un método numérico de diferencias finitas. Como resultado, se obtuvo la relación que guardan las fuerzas actuando en el contacto (torsión y capacidad de carga), así como las condiciones de operación impuestas sobre éste, es decir, la viscosidad del fluido, velocidad angular y espesor de la capa de lubricante. Finalmente, se obtuvieron las siguientes conclusiones:

La capacidad de carga de la capa de fluido es directamente proporcional al producto de la viscosidad del fluido y la velocidad angular de la superficie en rotación; a su vez la capacidad de carga disminuye con la distancia entre las superficies del contacto y aumenta con la inclinación entre ellas.

La curva de Stribeck, la cual resume el funcionamiento del contacto lubricado, depende solamente de la inclinación relativa entre las superficies del mismo. Estos resultados concuerdan satisfactoriamente con resultados experimentales encontrados en la literatura.

Más allá del interés de este problema desde el punto de vista de la lubricación, las soluciones encontradas aquí tienen también aplicación en reometría. Los resultados obtenidos pueden ser usados para determinar la inclinación en una geometría de caracterización reológica del tipo plato-plato.

8.2 Lubricación ferrohidrodinámica en un contacto de superficies inclinadas

Con el objetivo de estudiar el funcionamiento de un contacto lubricado con un fluido magnético se realizaron experimentos de flujo en una geometría de plato-plato adaptada para estudios magnetoreológicos, esto es, permite aplicar un campo magnético sobre la muestra considerada. Esta geometría fue matemáticamente modelada como el contacto estudiado en la sección anterior, siendo el mismo mecanismo el encargado de introducir las fuerzas de lubricación en el contacto. La diferencia en este caso reside en aplicar un campo magnético sobre el nanofluido magnético, provocando la aparición de fuerzas magnéticas sobre este.

Mediante experimentos de flujo se midieron la fuerza de cizalla en el contacto, así como su capacidad de carga. La representación de la última en función del producto de la viscosidad del fluido y la velocidad angular de la superficie en rotación, $\eta\Omega$, puede ser dividida en tres regiones, determinadas por el balance entre las fuerzas hidrodinámicas y magnéticas actuando en la capa de fluido magnético que separaba las superficies del contacto. Tras analizar éstas tres regiones se obtuvieron las siguientes conclusiones:

En la primera de ellas, correspondiente a valores bajos del parámetro $\eta\Omega$, la capacidad de carga se mantenía constante a un valor que dependía solamente de la intensidad de las fuerzas magnéticas en la capa de fluido. De acuerdo con los resultados obtenidos a partir de la teoría de lubricación hidrodinámica de Reynolds, en esta región, la presión generada en la capa de fluido por las fuerzas de origen hidrodinámico era menor que la de origen magnético, por lo que no se encontró cavitación dentro del fluido.

Sólo cuando aparece cavitación en una porción de la capa de fluido se encuentra que la fuerza hidrodinámica aumenta con respecto al parámetro $\eta\Omega$, determinando una segunda región. Finalmente, en la tercera región para intensidades bajas o intermedias de campo magnético y valores altos del parámetro $\eta\Omega$, las fuerzas hidrodinámicas dominan sobre las magnéticas, siendo las primeras las que contribuyen en mayor medida a la capacidad de carga del contacto

8.3 Control de inanición en un contacto suave empleando fluidos magnéticos

Se dice que un contacto opera en el régimen de lubricación elasto-hidrodinámica suave cuando la presión en la capa de fluido que separa sus superficies es lo suficientemente alta como para causar la deformación de al menos una de ellas, pero no tan alta como para causar cambios en la viscosidad del fluido a la entrada del contacto. En este trabajo se presentaron resultados experimentales obtenidos para un contacto compuesto de una bola cargada contra un plano, trabajando en el régimen de lubricación previamente mencionado. La cantidad de fluido magnético colocada en el contacto para lubricarlo fue restringida y atrapada alrededor de éste por un campo magnético producido por imanes circulares colocados por debajo del disco.

A altas velocidades de operación, el contacto trabajaba en un régimen de lubricación de inanición de lubricante. Este fenómeno pudo ser observado en un cambio abrupto en la pendiente de las curvas de fricción frente a la velocidad de arrastre de fluido en el interior del contacto. Este cambio de régimen ocurrió debido a la ruptura del mecanismo de reabastecimiento de fluido a la entrada del contacto desde la salida de éste.

De acuerdo a los datos experimentales obtenidos en este trabajo se pudo concluir que:

El contacto empieza a trabajar en inanición a menor velocidad de arrastre para una viscosidad mayor del fluido. La capacidad de carga no tiene un efecto significativo en el valor de la velocidad previamente mencionada.

El campo magnético aplicado al fluido dentro del contacto es capaz de aumentar la velocidad de transición entre los regímenes de lubricación mencionados en este apartado, e incluso evitar por completo que el contacto trabaje en el régimen de inanición. Cuanta mayor sea la viscosidad del fluido lubricando el contacto, mayor será la intensidad del campo magnético aplicado para evitar dicha transición.

Appendix I. Algorithm for numerical solution of the Reynolds equation

To clarify the procedure used in this work to numerically solve the Reynolds equation, the code of the program written for this work and its corresponding flow diagram are shown in this appendix.

The code was written using the Visual basic platform available in the program Microsoft Excel. This is presented in the following:

```
Option Explicit
'------------------------------------------------------------------------------
'------------------------------------------------------------------------------
Dim nr As Integer, nt As Integer, nt2 As Integer 'number of intervals
Dim deltar As Double, deltat As Double 'mesh size
Dim radio As Double, hin As Double, epsilon As Double, radioi As Double, wa As
Double 'geometry dimensions
Dim eta As Double
Dim angular As Double
Dim pinicial As Double
Dim teta() As Double, r() As Double
Dim p() As Double, pold() As Double
Dim h() As Double
Dim dhdt() As Double, dhdr() As Double
Dim A As Double, B As Double, D As Double 'dummy coeff for reynolds equation
Dim C1() As Double, C2() As Double, C3() As Double, C4() As Double, C() As
Double, E() As Double 'coeff for reynolds equation
Dim pc As Double 'central pressure
Dim pmax As Double 'maximum pressure
Dim fin As Double
'----------------main program----------------------------------------------------
Sub main()
Call read
Call dimensioning
Call grid
Call calc_gap
Call calc_coef
Call calc_inicial
Call solver
Call calc_maxp
Call write_results
Call fuerza_in
End Sub
'-----------------read input parameters-------------------------------------
Sub read()
nr = Worksheets(1).Cells(2, 2)
nt2 = Worksheets(1).Cells(4, 2)
radio = Worksheets(1).Cells(6, 2)
radioi = Worksheets(1).Cells(6, 5)
hin = Worksheets(1).Cells(8, 2)
angular = Worksheets(1).Cells(10, 2)
epsilon = Worksheets(1).Cells(12, 2)
eta = Worksheets(1).Cells(14, 2)
pinicial = Worksheets(1).Cells(16, 2)
wa = Worksheets(1).Cells(18, 2)
wa = wa * 0.000001
nt = 4 * nt2
```

```
epsilon = epsilon * 0.000001
hin = hin * 0.000001
End Sub
'----------------------------------------------------------------------------
Sub dimensioning()
ReDim p(0 To nr, 0 To nt)
ReDim pold(0 To nr, 0 To nt)
ReDim teta(0 To nt)
ReDim r(0 To nr)
ReDim h(0 To nr, 0 To nt)
ReDim dhdr(0 To nr, 0 To nt)
ReDim dhdt(0 To nr, 0 To nt)
ReDim C(0 To nr, 0 To nt)
ReDim E(0 To nr, 0 To nt)
ReDim C1(0 To nr, 0 To nt)
ReDim C2(0 To nr, 0 To nt)
ReDim C3(0 To nr, 0 To nt)
ReDim C4(0 To nr, 0 To nt)
End Sub
'----------------------------------------------------------------------------
Sub grid()
Dim i As Integer
deltar = (radio - radioi) / nr
deltat = 8 * Atn(1) / nt
For i = 0 To nr
   r(i) = i * deltar + radioi
Next i
For i = 0 To nt
   teta(i) = i * deltat
Next i
End Sub
'----------------------------------------------------------------------------
Sub calc_gap()
Dim i As Integer, j As Integer
For i = 0 To nr
   For j = 0 To nt
     h(i, j) = hin + hsd(r(i), teta(j))
   Next j
Next i
For i = 1 To nr - 1
   For j = 0 To nt
     dhdr(i, j) = dhr(teta(j))
     dhdt(i, j) = dht(r(i), teta(j))
   Next j
Next i
End Sub
'----------------------------------------------------------------------------
Sub calc_coef()
Dim i As Integer, j As Integer
For i = 1 To nr - 1
```

```
   A = r(i) * r(i)
   For j = 0 To nt
      B = (1 / r(i) + 3 * dhdr(i, j) / h(i, j))
      D = 3 * dhdt(i, j) / (h(i, j) * A)
      C(i, j) = 2 / (deltar * deltar) + 2 / (A * deltat * deltat)
      C1(i, j) = 1 / (deltar * deltar) + B / (2 * deltar)
      C2(i, j) = 1 / (deltar * deltar) - B / (2 * deltar)
      C3(i, j) = 1 / (A * deltat * deltat) + D / (2 * deltat)
      C4(i, j) = 1 / (A * deltat * deltat) - D / (2 * deltat)
      E(i, j) = -6 * eta * angular * dhdt(i, j) / (h(i, j) * h(i, j) * h(i, j))
   Next j
Next i

End Sub
'----------------------------------------------------------------------------------
Sub calc_inicial()
Dim i As Integer, j As Integer
For i = 0 To nr
   For j = 0 To nt
      pold(i, j) = pin(r(i))
   Next j
Next i
End Sub
'----------------------------------------------------------------------------------
Sub solver()
Dim i As Integer, j As Integer, iter As Long
Dim pd As Double
Dim resta As Double, sumresta As Double, suma As Double
Dim error As Double, tol As Double
Dim relax As Double
Dim pcold As Double
tol = 0.00001
error = 2 * tol 'ensures it always goes inside the while cycle
iter = 0
relax = 1
pcold = pinicial
While error > tol
iter = iter + 1
If iter > 50000 Then relax = 0.5
If iter > 100000 Then relax = 0.3
sumresta = 0
suma = 0

For i = 1 To nr - 1
   pd = (E(i, 0) + C1(i, 0) * pold(i + 1, 0) + C2(i, 0) * pold(i - 1, 0) + C3(i, 0) * pold(i, 1)
+ C4(i, 0) * pold(i, nt - 1)) / C(i, j)
   resta = pd - pold(i, 0)
   If pd < 0 Then
      pd = 0
      resta = 0
```

```
    End If
    pold(i, 0) = pold(i, 0) + relax * resta
    pold(i, nt) = pold(i, 0)
    sumresta = sumresta + relax * Abs(resta)
    suma = suma + Abs(pold(i, 0))
Next i
For i = 1 To nr - 1
   For j = 1 To nt - 1
      pd = (E(i, j) + C1(i, j) * pold(i + 1, j) + C2(i, j) * pold(i - 1, j) + C3(i, j) * pold(i, j
+ 1) + C4(i, j) * pold(i, j - 1)) / C(i, j)
      resta = pd - pold(i, j)

      pold(i, j) = pd + relax * resta
      If pd < 0 Then

         pold(i, j) = 0
         resta = 0
      End If
      sumresta = sumresta + relax * Abs(resta)
      suma = suma + Abs(pold(i, j))
   Next j
Next i

error = sumresta / suma
Worksheets(3).Cells(1, 1) = iter
Worksheets(3).Cells(1, 2) = error
Worksheets(3).Cells(1, 3) = pc
Wend
End Sub
Sub calc_maxp()
Dim i As Integer, j As Integer
Dim imax As Integer, jmax As Integer
pmax = pc
imax = 0
jmax = 0
For i = 1 To nr - 1
   For j = 0 To nt - 1
   If pold(i, j) > pmax Then
      pmax = pold(i, j)
      imax = i
      jmax = j
   End If
   Next j
Next i
Worksheets(3).Cells(6, 6) = imax
Worksheets(3).Cells(6, 7) = jmax
End Sub
'----------Integrates pressure to obtain the force excerted by the fluid----------------------
'----------------------integration by simpson 1/3 method-------------------------------------
Sub fuerza_in()
```

```vba
Dim i As Integer, j As Integer
Dim sum As Single
For i = 0 To nr
    For j = 0 To nt
        p(i, j) = r(i) * pold(i, j)
    Next j
Next i

sum = p(0, 0) + p(nr, nt) + p(0, nt) + p(nr, 0)
For i = 2 To nr - 2 Step 2
    sum = sum + 2 * p(i, 0) + 4 * p(i - 1, 0) + 2 * p(i, nt) + 4 * p(i - 1, nt)
    sum = sum + 8 * p(i, nt - 1) + 16 * p(i - 1, nt - 1)
Next i
sum = sum + 4 * p(nr - 1, 0) + 4 * p(nr - 1, nt)
For j = 2 To nt - 2 Step 2
    sum = sum + 2 * p(0, j) + 2 * p(nr, j) + 4 * p(0, j - 1) + 4 * p(nr, j - 1)
    sum = sum + 8 * p(nr - 1, j) + 16 * p(nr - 1, j - 1)
Next j
sum = sum + 4 * p(0, nt - 1) + 4 * p(nr, nt - 1)
For i = 2 To nr - 2 Step 2
    For j = 2 To nt - 2 Step 2
        sum = sum + 4 * p(i, j) + 8 * p(i - 1, j) + 8 * p(i, j - 1) + 16 * p(i - 1, j - 1)
    Next j
Next i
sum = sum + 16 * p(nr - 1, nt - 1)
fin = (deltar * deltat) * sum / 9
Worksheets(3).Cells(5, 6) = fin
End Sub
'-------------------------------------------------------------------------------
Sub write_results()
Dim i As Integer, j As Integer
For i = 0 To nr
    Worksheets(2).Cells(i + 2, 1) = r(i)
    For j = 0 To nt - 1
        Worksheets(2).Cells(1, j + 2) = teta(j)
        Worksheets(2).Cells(i + 2, j + 2) = pold(i, j)
    Next j
Next i
Worksheets(3).Cells(5, 5) = pmax
End Sub
'-------------------------------------------------------------------------------
'-------------------------------------------------------------------------------
Function hsd(ByVal rs As Double, ByVal tetas As Double) As Double
    hsd = epsilon * rs * Cos(tetas) / (radio * 2) + epsilon / 2 + wa * (1 + Cos(2 * tetas))
End Function
'-------------------------------------------------------------------------------
Function dhr(ByVal tetas As Double) As Double
    dhr = epsilon * Cos(tetas) / (radio * 2)
End Function
'-------------------------------------------------------------------------------
```

```
Function dht(ByVal rs As Double, ByVal tetas As Double) As Double
   dht = -epsilon * rs * Sin(tetas) / (radio * 2) - 2 * wa * Sin(2 * tetas)
End Function
'----------------------------------------------------------------------------------
Function pin(ByVal rs As Double)
   pin = pinicial * ((radio - rs) * (rs - radioi)) / (radio * radio)
End Function


'----------------------------------------------------------------------------------
'End of the program
'----------------------------------------------------------------------------------
```

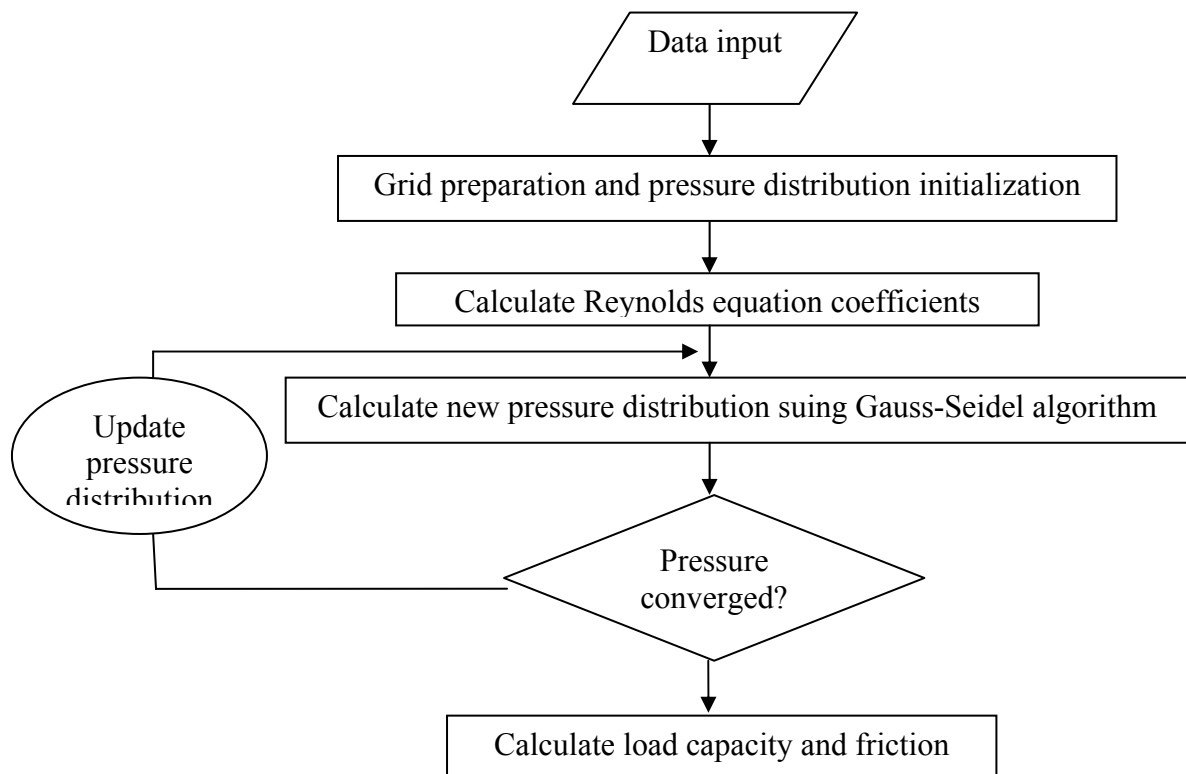The flow diagram corresponding to this code is presented in Figure I.1.

Figure I.1. Flow diagram corresponding to the code used to solve Reynolds equation.

Bibliography

[Adams, 1964] N. Adams, A. S. Lodge. Rheological properties of concentrated polymer solutions II. A cone-and-plate and parallel-plate pressure distribution apparatus for determining normal stress differences in steady shear flow. *Phil. Trans. Roy. Soc. Lond. A*, 256:149, 1964.

[Andablo-Reyes, 2010-1] E. Andablo-Reyes, R. Hidalgo-Álvarez, J. de Vicente, *J. Non-Newton. Fluid Mech.*. 165:1419, 2010.

[Andablo-Reyes, 2010-2] E. Andablo-Reyes, R. Hidalgo-Álvarez, J. de Vicente, C. Myant, T. Reddyhoff, H. A. Spikes. Soft elasto-ferrohydrodynamic lubrication. *Tribol. Lett.*, 39: 109, 2010.

[Bali, 2005] R. Bali, S. K. Sharma. Effect of magnetic field in lubrication of synovial joints. *Tribol Lett.*, 19:281, 2005.

[Bernzen, 2008] M. Bernzen, *Anton Paar Instruments. Private communication*, 2008.

[Berret, 2006] J. F. Berret, O. Sandre, A. Mauger. Size distribution of superparamagnetic particles determined by magnetic sedimentation. *Langmuir*, 23:2993, 2006.

[Bird, 1982] R. B. Bird, W. E. Stewart, E. N. Lightfoot. Fenómenos de transporte, John Wiley & Sons, New York, Spanish edition, 1982.

[Bongaerts, 2007] J. H. H. Bongaerts, K. Fourtouni, J. R. Stokes. Soft-tribology: lubrication in a compliant PDMS-PDMS contact. *Trib. Int.*, 40: 1531, 2007.

[Cann, 2004] P. M. E. Cann, B. Damiens, A. A. Lubrecht. The transition between fully flooded and starved regimes in EHL. *Tribol. Int.,* 37:859, 2004.

[Chandra, 1993] P. Chandra, P. Sinha. Ferrofluid lubrication of externally pressurized circular plates and conical bearings. *Int. J. Eng. Sci.,* 31:593, 1993.

[Chantrell, 1978] R. W. Chantrell, J. Popplewell, S. W. Charles. Measurements of particle size distribution parameters in ferrofluid. *IEEE Trans. Magn.,* 14:975, 1978.

[Chantrell, 1982] R. W. Chantrell, J. Sidhu, P. R. Bissell, P. A. Bates. Dilution induced instability in ferrofluids. *J. Appl. Phys.*, 53:8341, 1982.

[Chiu, 1974] Y. P. Chiu. An analysis and prediction of lubricant film starvation in rolling contact systems. *Tribol. Trans.,* 17:22, 1974.

[Clasen, 2010] C. Clasen, P. H. Kavehpour, G. H. McKinley. Bridging tribology and microrheology of thin films. *Appl. Rheol.*, 20:45049, 2010.

[Dababneh, 1995] M. S. Dababneh, N. Y. Ayoub. The effect of oleic acid on the stability of magnetic ferrofluid. *IEEE Trans. Mag.,* 31:4178, 1995.

[de Vicente, 2005] J. de Vicente, J. R. Stokes, H. A. Spikes. The frictional properties of Newtonian fluids in rolling-sliding soft-EHL contact. *Trib. Lett.,* 20:237, 2005.

[de Vicente, 2006] J. de Vicente, J. R. Stokes, H. A. Spikes. Rolling and sliding friction of compliant, lubricated contact. *Proc. IMechE Part J: J. Eng. Trib.*, 20:55, 2006.

[Dudgeon, 1993] D. J. Dudgeon, L. E. Wedgewood. Flow in the misaligned cone-and-plate rheometer. *J. Non-Newton. Fluid Mech.*, 48:21, 1993.

[Fay, 1996] J. A. Fay, Mecánica de Fluidos. Compañía Editorial Continental, México, 1996.

[Greensmith, 1953] H. W. Greensmith, R. S. Rivlin. The hydrodynamics of non-Newtonian fluids. III. The normal stress effect in high-polymer solutions. *Philos. Trans. R. Soc. Lond. A,* 245:399, 1953.

[Guangteng, 1992] G. Guangteng, P. M. Cann, H. A. Spikes. A study of parched lubrication. *Wear,* 153:91, 1992.

[Hamrock, 1978] B. J. Hamrock, D. Dowson. Elastohydrodynamic lubrication of elliptical contacts for material of low elastic modulus. *Trans. ASME J. Lubr. Technol.,* 100:236, 1978.

[Huang, 2004] J. P. Huang, C. Holm. Magnetization of polydisperse colloidal ferrofluids: effect of magnetistriction. *Phys. Rev. E*, 70:061404, 2004.

[Ivanov, 2007] A. O. Ivanov, S. S. Kantorovich, E. N. Reznivok, C. Holm, A. F. Pshenichnivok, A. V. Lebedev, A. Chremos, P. J. Camp. Magnetic properties of polydisperse ferrofluids: A critical comparison between experiment, theory and simulation. *Phys. Rev. E*, 75:061405, 2007.

[Jianhai, 1992] L. Jianhai, W. Shizhu. Fully flooded, starved and parched lubrication at a point contact system. *Wear*, 159:135, 1992.

[Kavehpour, 2004] H. P. Kavehpour, G. H. McKinley. Tribo-rheometry: from gap-dependent rheology to tribology. *Trib. Lett.*, 17:327, 2004.

[Koc, 2007] E. Koç, E. C. Sabir. An investigation on the lubrication mechanism of the mechanical radial face seals-II: hydraulic balance of the ring. *Indust. Lub. Tech.*, 59/4:166, 2007.

[Khonsari, 2001] M. M. Khonsari, E. R. Booser, Applied Tribology: Bearing design and lubrication. John Wiley & Sons, New York, 2001.

[Ku, 2009] I. S. Y. Ku, T. Reddyhoff, J. H. Choo, A. S. Holmes, H. A. Spikes. A novel tribometer for the measurement of friction in MEMS. *Trib. Int.*, 43: 1087, 2009.

[Kumar, 1993] D. Kumar, P. Chandra, P. Sinha. Ferrofluid lubrication of externally pressurized circular plates and conical bearings. *Int. J. Engn. Sci.,* 31:593, 1993.

[Kuzhir, 2007] P. Kuzhir. Free boundary of lubricant film in ferrofluid journal bearings. *Trib. Int.*, 41:256, 2007.

[Lavaca, 1999] Z. G. M. Lavaca, R. B. Azevedo, L. M. Lavaca, E. V. Martins, V. A. P. Garcia, C. A. Rébula, A. P. C. Lemos, M. H. Sousa, F. A. Tourinho, P. C. Morais, M. F. Da Silva. Toxic effects of ionic magnetic fluids in mice. *J. Magn. Magn. Mater.*, 194:90, 1999.

[Lavaca, 2010] L. M. Lavaca, Z. G. M. Lavaca, M. F. Da Silva, O. Silva, S. B. Chaves, R. B. Azevedo, F. Pelegrini, C. Gansau, N. Buske, D. Savolovic, P. C. Morais. Magnetic resonance of a dextran-coated magnetic fluid intravenously administered in mice. *Biophys. J.*, 80:2483, 2001.

[Lubbinge, 1999] H. Lubbinge. On the lubrication of mechanical face seals. *PhD. Thesis.* University of Twente, 1999.

[Mahle, 2008] S. Mahle, P. Ilg, M. Liu. Hydrodynamic theory of polydisperse chain-forming ferrofluids. *Phys. Rev. E*, 77:016305, 2008.

[Naduvinamani, 2009] N. B. Naduvinamani, S. B. Patil. Numerical Solution of finite modified Reynolds equation for couple stress squeeze film lubrication of porous journal bearings. *Comp. Struct.*, 87:1287, 2009.

[Persson, 2009] B. N. J. Persson, M Scaraggi. On the transition from boundary lubrication to hydrodynamic lubrication. *J. Phys.: Condens. Matter*, 21:185002, 2009.

[Racuciu, 2007] M. Răcuciu, D. E. Crangă, V. Bădescu, N. Sulitanu. Microstructural investigation of some biocompatible ferrofluids. *J. Magn. Magn. Mater.*, 316: 772, 2007.

[Ravaud, 2010] R. Ravaud, G. Lemarquand, V. Lemarquand. Mechanical properties of ferrofluid applications: Centering effect and capacity of a seal. *Tribol. Int.* 43 :76, 2010.

[Rosensweig, 1997] R. E. Rosensweig. Ferrohydrodynamics. *Dover Publications*, INC. New York, 1997.

[Ranger, 1975] A. P. Ranger, C. M. M. Ettles, A. Cameron. The solution of the point contact elasto-hydrodynamic problem. *Proc. R. Soc. Lond. A.,* 346:227, 1975.

[Sabir, 2007] E. C. Sabir, E. Koç. An investigation on the lubrication mechanism of the mechanical radial face seals-I: general theory. *Indust. Lub. Tech.*, 59/2:85, 2007.

[Shah, 2004] R. C. Shah, M. V. Bhat. Ferrofluid squeeze film in a long journal bearing. *Tribol. Int.*, 37:441, 2004.

[Shliomis, 2001] M. I. Shliomis. Comment on "Magnetoviscosity and relaxation in ferrofluids". *Phys. Rev. E*, 64:063501, 2001.

[Skotheim, 2004] J. M. Skotheim, L. Mahadevan. Soft lubrication. *Phys. Rev. Lett.*, 92:245509-1, 2004.

[Stachowiak, 2000] G. W. Stachowiak, A. W. Batchelor. Engineering Tribology, Butterworth Heinemann, 2000.

[Steffe, 1992] J. F. Steffe. Rheological methods in food process engineering. Freeman Press, USA, 1992.

[Taylor, 1957] G. Taylor, P. G. Saffman. Effects of compressibility at low Reynolds number. *J. Aero. Sci.*, 24:553, 1957.

[Walker, 1979] J. S. Walker, J. D. Buckmaster. Ferrohydrodynamic thrust bearing. *Int. J. Engn. Sci.*, 17:1171, 1979.

[Walters, 1975] K. Walters. Rheometry. Chapman and Hall Ltd., London, 1975.

[Yin, 2009] C. Yin, P. H. Yang, H. Tan, J. Wang. Thermal elastohydrodynamic lubrication of starved elliptical contacts. *J. Tribol. Int.*, 42:964, 2009.